LUT UNIVERSITY
LUT School of Energy Systems
LUT Mechanical Engineering

Arttu Muikku

FATIGUE ASSESSMENT OF LIFTING BOOM

1.9.2021

Examiner(s): Professor Timo Björk
M. Sc. (Tech.) Jami Leivo

TIIVISTELMÄ

LUT-Yliopisto
LUT School of Energy Systems
LUT Kone

Arttu Muikku

Nostopuomin väsymisanalyysi

Diplomityö

2021

62 sivua, 36 kuvaa, 2 taulukkoa ja 18 liitettä

Tarkastajat: Professori Timo Björk
DI Jami Leivo

Hakusanat: väsymisanalyysi, tehollinen lovijännitys, hot spot jännitys, 4R menetelmä, nimellinen jännitys, True-Load, Palmgren-Miner vauriosumma.

Tässä diplomityössä toteutettiin väsymisanalyysi nostopuomille perustuen väsytyskokeen aikana mitattuun venymäliuskadataan soveltaen kahta eri menetelmää. Puomiin väsytyskokeen testisyklin aikana vaikuttavat ulkoiset voimat määritettiin venymäliuskadatan perusteella. True-Load on kaupallinen ohjelmisto, jolla edellä mainittu voimien määritys tehtiin. Toinen käytetty menetelmä perustui kahdeksaan venymäliuskaan, joiden perusteella voitiin määrittää poikkileikkauksessa vaikuttavat sisäiset voimat ja momentit, josta edelleen voitiin ratkaista ulkoiset voimat. Jälkimmäiselle menetelmälle käytettiin nimeä 8-venymäliuskan menetelmä.

4R menetelmän, tehollisen lovijännitys menetelmän ja hot spot menetelmän tuloksia vertailtiin ja nimellisen jännityksen menetelmää sovellettiin hiotuille hitseille. Eri väsymisanalyysi menetelmillä saadut tulokset olivat samaa suuruusluokkaan. Laskennan ja FE-analyysin mahdollistamiseksi toteutettiin jäännösjännitys- ja geometriamittauksia.

Väsymisanalyysi suoritettiin onnistuneesti käyttäen True-Load ohjelmaa. Kyseinen ohjelma kuitenkin todennäköisesti yliarvioi joitakin jännityspiikkejä, jonka seurauksena vauriosummien arvot olivat korkeita verrattuna mitattuun dataan. 8-venymäliuskan menetelmä vaikutti toimivan erittäin hyvin lähellä venymäliuskojen sijaintia mutta ei antanut hyväksyttäviä tuloksia kauempana. Vähäisen venymäliuskadatan takia laskenta perustui vai yhden testisyklin aikana mitattuun dataan minkä seurauksena tuloksiin jäi jonkin verran epävarmuutta.

ABSTRACT

LUT University
LUT School of Energy Systems
LUT Mechanical Engineering

Arttu Muikku

Fatigue assessment of lifting boom

Master's thesis

2021

62 pages, 36 figures, 2 tables and 18 appendices

Examiners: Professor Timo Björk
M. Sc. (Tech.) Jami Leivo

Keywords: fatigue analysis, effective notch stress, hot spot stress, 4R method, nominal stress, True-Load, Palmgren-Miner's damage sum.

In this thesis two different methods were used to implement fatigue analysis of a lifting boom based on strain gauge data collected during fatigue testing. Strain gauge data was used to determine the external forces acting on the boom during the test cycle. True-Load is a commercial software that does the above mentioned. Another method based on 8 strain gauges was used to determine internal forces and moments and through those the external forces. The latter method was named 8-strain gauge method.

Results of the 4R method, effective notch stress method and hot spot method were compared, and nominal stress method was used for ground welds. The results of the different fatigue assessment methods were in the same order of magnitude. To support the calculations and FE-analysis residual stress and geometry measurements were taken into account.

Fatigue assessment was successfully conducted based on the True-Load software. Although this software overestimated some stress peaks which led to significantly higher damage sums compared to measured data. The 8-strain gauge method seemed to work very well close to the strain gauges location but did not give acceptable result further away. Due to lack of strain gauge data, calculations were based on strain gauge data of single test cycle which left some uncertainty to the accuracy of the results.

ACKNOWLEDGEMENTS

I would like to thank everyone involved at Ponsse and LUT University for the chance to do my master's thesis from such interesting topic. I would also want to express my gratitude to the examiners of the thesis Professor Timo Björk and M. Sc. (Tech.) Jami Leivo for the guidance and smooth cooperation during the thesis. Additionally, D. Sc. (Tech.) Antti Ahola has been great help during the whole project.

During the project various people from both Ponsse and LUT have lent me some of their time and expertise which have made this thesis possible. So, thanks to everyone involved.

Finally, I would like to thank family and friends for giving balance to life.

Arttu Muikku
Tampere 1.9.2021

TABLE OF CONTENTS

LIST OF SYMBOLS AND ABBREVIATIONS

A	Cross-section area [mm]
A_m	Area enclosed by the cross-sectional center line [mm^2]
B_ω	Bimoment [Nmm^2]
C_{ref}	Fatigue capacity [MPa^m]
$C_{ref,char}$	Characteristic fatigue capacity $10^{20.83}$ [MPa^m]
$C_{ref,mean}$	Mean fatigue capacity $10^{21.59}$ [MPa^m]
D	Palmgren-Miner's linear damage sum
E	Young's modulus [MPa]
FAT_1	Fatigue capacity above knee point [MPa]
FAT_2	Fatigue capacity below knee point [MPa]
FAT_{char}	Fatigue class corresponding to 95 % survival probability [MPa]
FAT_{mean}	Fatigue class corresponding to mean life [MPa]
F_1	Force causing the torsion [N]
F_i	Force multipliers from True-load
F_x	External force in x-direction [N]
F_y	External force in y-direction [N]
F_z	External force in z-direction [N]
H	Strain hardening coefficient [MPa]
I_{yy}	Second moment of area around y-axis [mm^4]
I_{zz}	Second moment of area around z-axis [mm^4]
I_ω	Warping constant [mm^6].
m	Slope parameter for 4R method 5.85
m_1	Slope parameter of the S-N curve when above the knee point 3
m_2	Slope parameter below knee point 5
M_{yy}	Bending moment around y-axis [Nmm]
M_{zz}	Bending moment around z-axis [Nmm]
n	Strain hardening exponent
N	Normal force [N]
N_f	Fatigue life or fatigue life estimation
n_i	Number of cycles at certain stress range

N_i	Fatigue life at certain stress range
R	Stress ratio
R_{local}	Local stress ratio
R_m	Material ultimate strength [MPa]
$R_{p0.2}$	Proof strength [MPa]
r_{true}	Radius of the real weld toe [mm]
$S_{LUT4,LUT8}$	First moment of area at LUT4 and LUT8 locations [mm^3]
$S_{LUT6,LUT10}$	First moment of area at LUT6 and LUT10 location [mm^3]
t	Plate thickness [mm]
t_1	Wall thickness at LUT4, LUT6 and LUT10 [mm]
t_2	Plate thickness at LUT8 [mm]
t_3	Combined wall thickness of LUT6 and LUT10 locations [mm]
t_4	Combined wall thickness of LUT4 and LUT8 locations [mm]
T_{avg}	Average torsional moment in the cross-section [Nmm]
T_{LUT4}–T_{LUT10}	Torsional moments corresponding to the strain gauges [Nmm]
x	Coordinate through plate thickness [mm]
X	X-distance between the bearing and LUT-plane [mm]
Y	Half of the bearing distance in y-direction [mm]
y_{LUT3}– y_{LUT9}	Y-coordinates corresponding to the strain gauges [mm]
Z_1	Z-distance between the bearing and the center of mass for the LUT-plane [mm]
z_{LUT3}– z_{LUT9}	Z-coordinates corresponding to the strain gauges [mm]
$\Delta\varepsilon$	Strain range
$\Delta\varepsilon_e$	Elastic strain range
$\Delta\varepsilon_p$	Plastic strain range
$\Delta\sigma$	Stress range [MPa]
$\Delta\sigma_k$	Effective notch stress range [MPa]
$\Delta\sigma_L$	Stress range at knee point [MPa]
$\Delta\sigma_{local}$	Local stress range [MPa]
ε_{LUT3}–ε_{LUT9}	Strain values from measurements corresponding to subindex
ε_u	Ultimate strain
$\varepsilon_{p0.2}$	0.2 % plastic strain

σ_b	Bending stress [MPa]
σ_m	Membrane stress [MPa]
σ_{max}	Maximum local stress [MPa]
σ_{min}	Minimum local stress [MPa]
σ_{res}	Residual stress [MPa]
σ_x, σ_y, σ_z	Total normal stress components [MPa]
$\sigma_{x,i}$, $\sigma_{y,i}$, $\sigma_{z,i}$	Normal stress component corresponding to specific load from FE-model
$\sigma(x)$	Normal stress component perpendicular to the weld toe as function of x [MPa]
τ_{LUT4}–τ_{LUT10}	Shear stresses corresponding to the measured strain gauge values [MPa]
τ_{xy}, τ_{yz}, τ_{zx}	Total shear stress components [MPa]
$\tau_{xy,i}$, $\tau_{yz,i}$, $\tau_{zx,i}$	Shear stress components corresponding to specific load from FE-model [MPa]
ω_{LUT3}– ω_{LUT9}	Sectorial coordinates corresponding to strain gauge in question [mm^2]
AGIFAP	Advanced Graphical Interactive Frame Analysis Package
ENS	Effective notch stress method
FE	Finite element
FEMAP	Finite element modeling and postprocessing
HFMI	High frequency mechanical impact
HS	Hot spot method
IIW	International Institute of Welding
SEM	Scanning electron microscope
SG	Strain gauge
TL	True-Load software
4R	Fatigue assessment method that considers material strength, residual stress, weld toe radius and applied stress ratio

1 INTRODUCTION

Fatigue is a very important design criteria for machine components. This is true especially for welded components due to the relatively poor fatigue strength of welded joints. In real applications unlike in laboratory tests the loading is rarely constant amplitude or even uniaxial. The loading can be complex, and it can change depending on the operating environment. This makes the fatigue analysis of components loaded by variable loading difficult.

The aim of this master's thesis was to do fatigue analysis for a lifting boom under variable amplitude loading. This project was conducted in collaboration with Ponsse. Fatigue analysis for as welded sections is conducted using effective notch stress method (ENS) and 4R method. Corners of the lifting boom are ground so for those nominal stress method is used. Hot spot method is also used to check certain details. Figure 1 shows the lifting boom considered in this thesis. Four weld toes were considered and those are numbered from 1 to 4 starting from the front end casting. Longitudinal welds were not considered due to location and direction of the welds those were not seen as critical. The lifting boom is part of a larger loader assembly of a Ponsse's forwarder. Figure 2 gives an idea of the loader and the used fatigue testing set up.

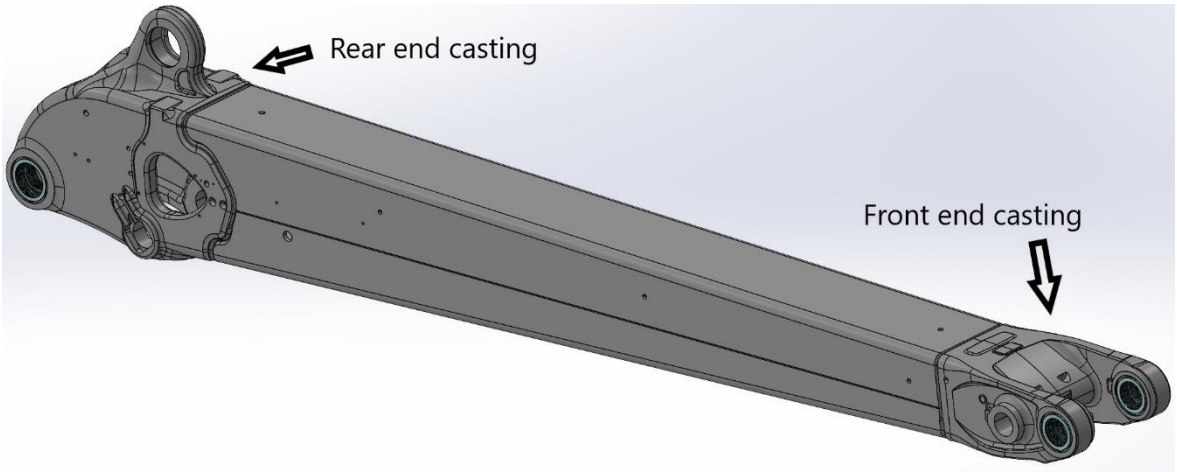

Figure 1. Lifting boom.

Before starting this thesis, some residual stress and geometry measurements had been conducted at LUT University. Also, the fatigue testing had been conducted by Ponsse. Aim of

this thesis was to generate notch stress finite element (FE) model required for the fatigue analysis and then conducting the fatigue analysis based on the measured strain gauge data using two different gauging methods for generating unit force model for fatigue analysis. First of the methods is a commercial software True-Load (TL) which is designed for this type of analysis. Second one is based on 8 strain gauges that are used to calculate the internal forces and moments of a beam structure and after those external forces of the lifting boom. The latter method was named 8-strain gauge method. Strain gauge data in combination of those two methods are used to calculate forces affecting the lifting boom. Combined effect of the various forces is then combined through the loading history utilizing superposition principle. This way complex loading case can be handled as a sum of few simple load cases. Also, results of different fatigue assessment and strain gauging methods are compared.

Geometry measurement are conducted so that weld geometry can be modelled based on the real structure.

Main ideas were to see if the simpler strain gauging method of only 8 strain gauges would give similar results as the calculations based on True-Load and whether or not different fatigue assessment methods give similar damage sum values.

2 METHODS

In this chapter, the research methods that are used in this thesis are introduced. Calculation procedures are explained, and compact literature review is conducted where necessary.

2.1 Experimental fatigue testing

Fatigue testing was conducted by Ponsse and they have also developed the test load cycle. Test is conducted by running the same test load cycle until fatigue fracture is observed. Test load is a variable amplitude loading history carried out by the three hydraulic cylinders attached to the end of the loader assembly as shown in figure 2. More detailed description of the test load cycle is not given in this work. Regular inspections were performed until a fatigue crack was found in the ground area of the weld joint at upper left corner of the front end casting and after that test was terminated. Test load was ran 84900 times before the failure was found. After the fatigue testing the boom was send to LUT University for additional examinations. Fatigue testing set up is shown in figure 2. As it can be seen from the figure the boom is tested as a part of larger loader assembly.

It was known that the loading is not perfectly symmetrical and also the effect of asymmetry changes slightly during the fatigue testing due to wearing and tightening of certain components. The fatigue calculations cannot take into account the effect of the asymmetry changes since not enough strain gauge data was available for neither True-Load or 8-strain gauge methods. Due to the lack of strain gauge data the calculations are based on measurements of a single test cycle. More accurate results could have been achieved if strain gauge data would have been available from various days.

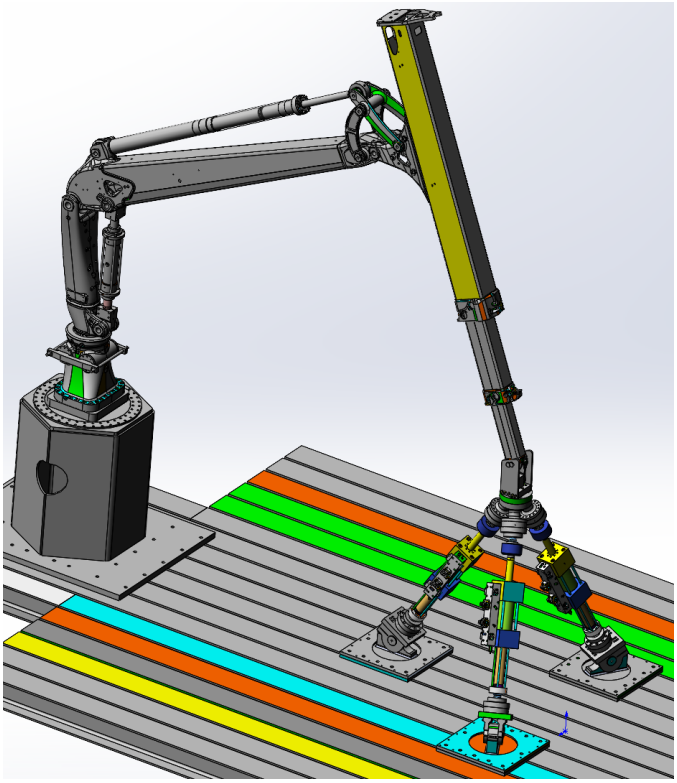

Figure 2. Fatigue testing set up.

2.2 Geometry measurements

Geometry of the welds was laser scanned using hexagon laser scanner and measuring arm. Weld surfaces were measured before fatigue testing, but the weld toes were measured only after the fatigue testing since it was not possible to fit the laser scanner inside the boom. Since the fatigue testing does not cause significant geometry changes in the weld this was seen as suitable approach.

Laser scanned 3D data was used to find the worst weld geometry considering fatigue life. 2D slices of the data were used to find dimensions required to model the welds. Dimensions measured from the 2D slices were flank angles, height of the weld, width of the weld and the weld toe radius. Similar measurements were conducted to weld roots as well. Due to the different geometries at the front and rear end castings the weld surfaces were considered to be different but same weld root geometry was assumed for both of those. Based on the measurements it was concluded that the real weld toe radius for the modeling of notch stress model should be considered as 0 mm.

2.3 Residual stress measurement using X-ray diffraction

Residual stresses at the weld toes were measured using Stresstech G3 X-ray diffractometer before and after the fatigue testing. Measurements after the fatigue testing were conducted to see the effect of residual stress relaxation. Also, older design iteration of the boom was measured from the similar locations to see how the residual stresses vary between the specimens. These two booms had some slight differences in the geometry and therefor the results are difficult to generalize to the newest design. Figure 3 shows the measuring locations of the rear end casting at the top flange and figure 4 shows the measuring locations of the rear end casting bottom flange and web and the measuring locations of the front end casting are shown in figure 5.

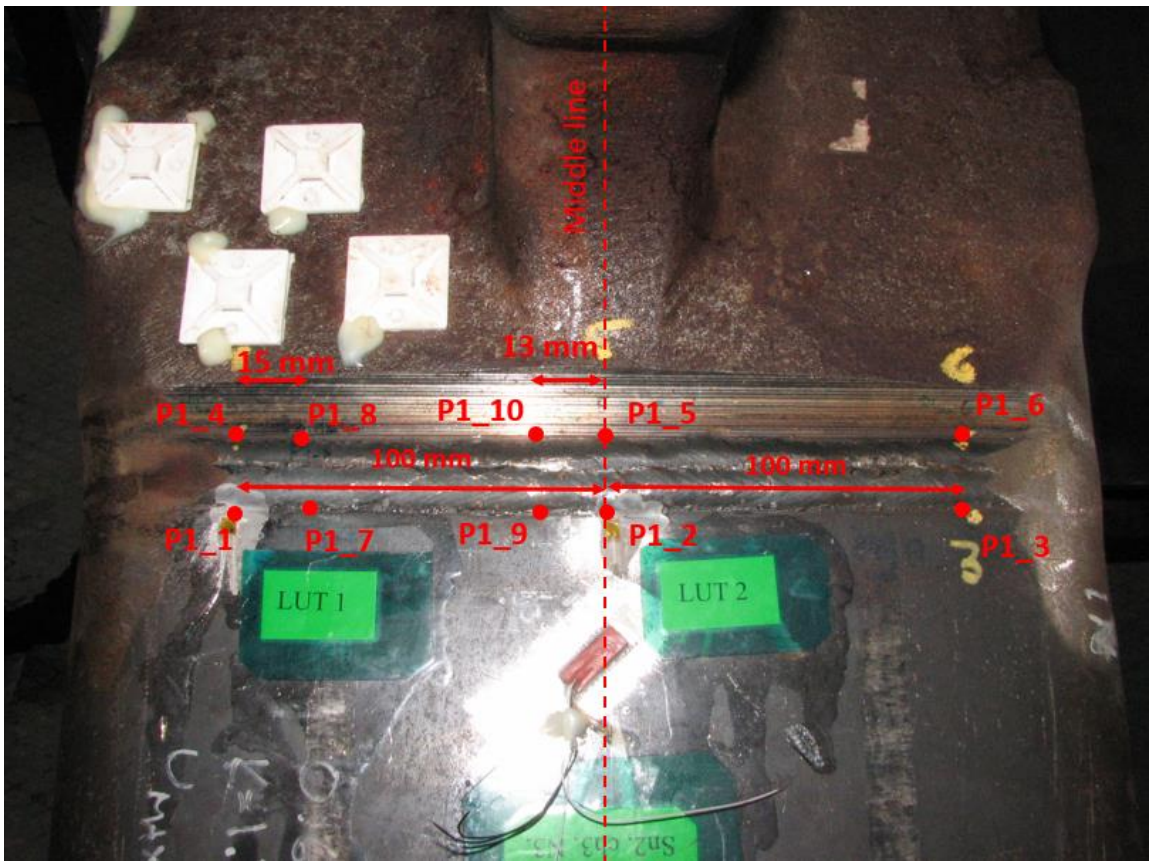

Figure 3. Residual stress measurement locations at the rear end castings top flange.

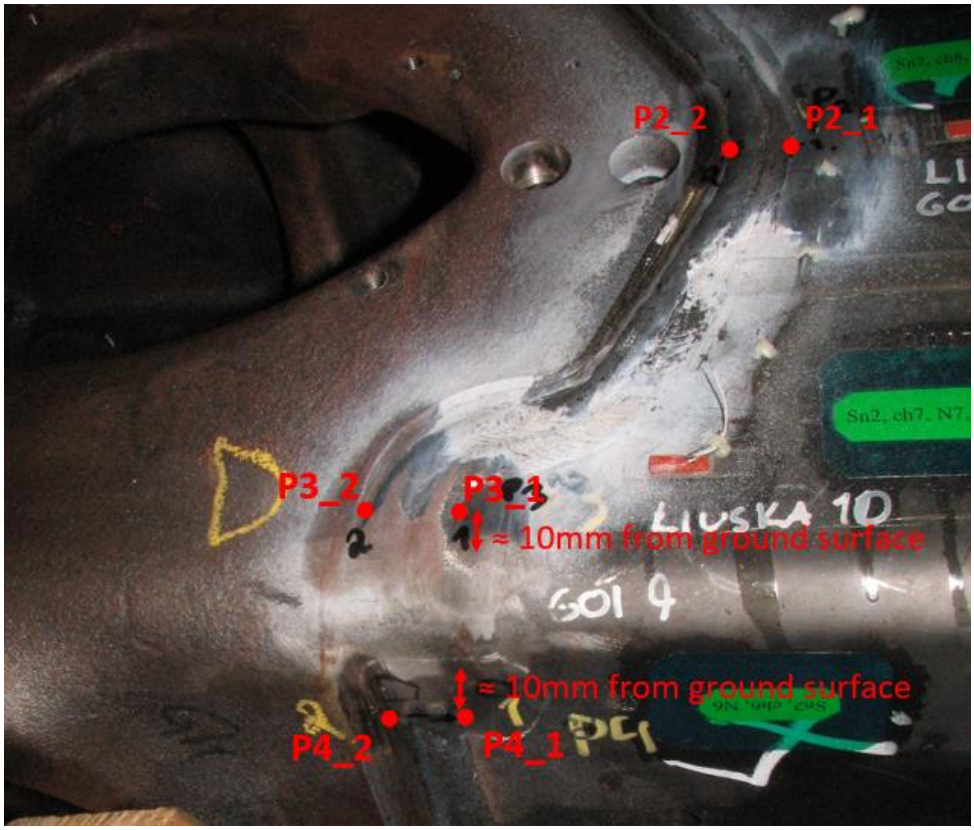

Figure 4. Residual stress measurement locations at rear end casting.

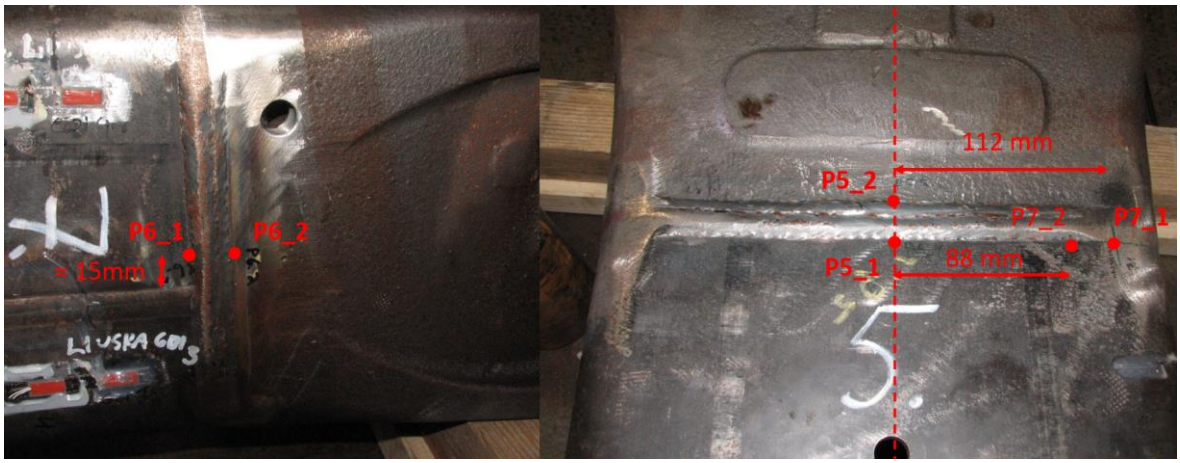

Figure 5. Residual stress measurement locations at front end casting.

Main differences between the two boom design versions are that the older version has a sharper peak at the transition from casting to the beam web and also at the top flange the weld is not straight but follows the shape of the cylinder bracket. These details of the older design are show in the figure 6 and those can be compared to figures 3–4.

Figure 6. Older design details.

Few new measurement locations were added after the fatigue test since the glue of strain gauges prevented measuring residual stresses at some of the locations. In these cases, new measuring points were set 10–15 mm to the side of the original measurement location while still being at the weld toe. Idea in this was to see if those locations could be used to see the effect of the residual stress relaxation. Also, some residual stress distributions perpendicular to the weld toe were measured after the fatigue test including one in the ground corner area. Distributions were measured starting from the weld toe and continuing to the plate material. Only exception to this is the distribution measured at the location P7_1 which is at the ground corner. Since it was not easy to identify the exact location of the weld toe on the ground area few measurements were taken into both directions and the zero position was set to the estimated location of the toe. Unfortunately, the residual stresses at the root side could not be measured since the diffractometer could not be positioned inside the boom structure.

During the measuring the collimator was tilted four times to both sides with tilt angle of ±45 degrees although when measuring close to the cylinder bracket the angle was reduced to avoid collision with the structure. Exposure time was set to 32 seconds and tilt oscillation was set to ±1 degree. For the distributions measurements were taken with 1 mm steps.

2.4 Hot spot strain gauges

The lifting boom was also equipped with two hot spot strain gauges. The strain gauges locations are at the top flange of the lifting boom at 0.4t distance from the weld toe. Exact locations for the gauges can be seen from figure 3. LUT1 hot spot strain gauge is located at P1_1

and LUT2 hot spot strain gauge at P1_2. These locations were thought to be possible critical locations before conduction the fatigue test.

2.5 Different fatigue assessment methods

In this thesis, various fatigue assessment methods are used. Results of local approaches are compared, and nominal stress method will be used on ground areas since notch stress methods are not suitable for those. Also, hot spot method is used in selected locations and compared to hot spot strain gauge, ENS and 4R results. Chapters below offer a short introduction to the used fatigue analysis methods.

Principal stresses were used in calculations for ENS, 4R and nominal stress methods and rainflow counting algorithm was used as the cycle counting method for every fatigue analysis method. Palmgren-Miner's linear damage sum is used to describe the fatigue damage caused by the loading. Palmgren-Miner's sum calculation can be formulated as follows (Hobbacher 2006, p. 96; SFS-EN 1993-1-9 2005, p. 31):

$$D = \sum_{i=1}^{k} \frac{n_i}{N_i} \tag{1}$$

In equation 1, D is the Palmgren-Miner's linear damage sum, n_i is the number of cycles at certain stress range and N_i is the fatigue life for that stress range. (Hobbacher 2006, p. 96; SFS-EN 1993-1-9 2005, p. 31)

Both design S-N curves available in Eurocode 3 and mean S-N curves were used in calculations. Since mean life S-N curves are not available in standards the mean life curves were calculated assuming that design curve has safety factor of 1.37 taken to the mean curve as suggested by Radaj, Sonsino and Fricke (2006, p. 165).

Knee points in S-N curves are taken into account based on the IIW recommendations which means that until 10 million cycles the slope parameter of 3 is used and after 10 million cycles slope parameter of 5 is used (Hobbacher 2016, p. 95). Those same slope parameters are used for nominal, hot spot and ENS methods. The S-N curves used for nominal, hot spot and ENS

calculations are shown in figure 7. Definition of the mean S-N curve based on the characteristic or design curve is shown in the equation below (Radaj, Sonsino and Fricke 2006, p. 165):

$$FAT_{mean} = 1.37 FAT_{char} \tag{2}$$

In equation 2 FAT_{mean} is the fatigue class corresponding to mean life and FAT_{char} is the fatigue class corresponding to 95% survival probability.

The definition of the knee point and fatigue class for stress ranges below knee point can be formulated as follows (modified from Hobbacher 2016, pp. 95–96):

$$\Delta\sigma_L = FAT_2 = \frac{FAT_1}{\left(\frac{10^7}{2 \times 10^6}\right)^{\frac{1}{m_1}}} \tag{3}$$

In equation 3 $\Delta\sigma_{\text{L}}$ is the stress range at knee point [MPa], FAT_1 is the fatigue capacity above knee point [MPa], FAT_2 is the fatigue capacity below knee point [MPa] and m_1 is the slope parameter of the S-N curve when above the knee point.

Calculation of fatigue life is performed using piecewise-defined function shown below (modified from Hobbacher 2016, pp. 95–96):

$$N_f = \begin{cases} 2 \times 10^6 \left(\frac{FAT_1}{\Delta\sigma}\right)^{m_1}, & \Delta\sigma \geq \Delta\sigma_L \\ 10^7 \left(\frac{FAT_2}{\Delta\sigma}\right)^{m_2}, & \Delta\sigma < \Delta\sigma_L \end{cases} \tag{4}$$

In equation 4 $\Delta\sigma_{\text{L}}$ is the stress range at knee point [MPa], FAT_1 is the fatigue capacity above knee point [MPa], FAT_2 is the fatigue capacity below knee point [MPa], m_1 is the slope parameter of the S-N curve when above the knee point, m_2 is the slope parameter below knee point, $\Delta\sigma$ is the stress range [MPa] and N_{f} is the fatigue life estimation.

In the equations 3–4, the knee point is set to 10^7 cycles. In case of different assumption for example in case of shear loading value 10^7 should be changed. Guidance for the knee points for various cases can be found in IIW guidelines (Hobbacher 2016, p. 95). Equations 2–4 are valid for nominal, hot spot and ENS methods.

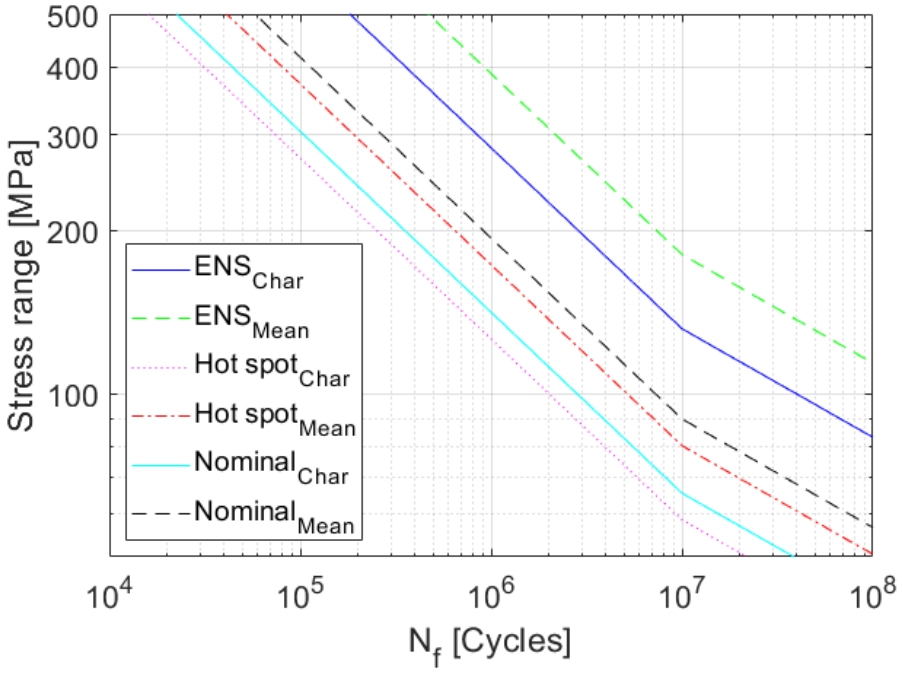

Figure 7. S-N curves for the various methods.

2.5.1 Nominal stress method

Nominal stress method is included in both IIW recommendations and Eurocode 3. In nominal stress method elastic material behavior is assumed and local stresses due to the weld geometry are not included. Finite element modeling is not required for the method, but the stresses can also be obtained from FE-model. Various fatigue classes are required for different weld details and these classes can also be found from the IIW recommendations and Eurocode 3. (Hobbacher 2016, pp. 15–17)

In this case the ground corners are modeled as flat surface in the FE-model. Nominal stresses were obtained as nodal stresses at the weld roots and toes. Design fatigue class used is FAT 112 for transverse butt welds ground flush with the plate.

2.5.2 Hot spot (structural stress) method

Hot spot method is also included in both IIW recommendations and Eurocode 3. Just like nominal stress method hot spot method also includes multiple fatigue classes for different types of details and also here linear material model can be assumed. Hot spot stresses can be obtained from a FE-model either using surface stress extrapolation or through-thickness linearization. The hot spot stress includes the stress concentration caused by the detail, but the non-linear peak stress is not included in calculations. (Niemi, Fricke & Maddox 2018, pp. 1, 41)

Since accurate solid element models will be constructed for the notch stress method through-thickness linearization method will be used for the hot spot method. Fatigue class 100 for full penetration butt joints is used in the calculations. The nodal normal stress component perpendicular to the weld toe is used to define the hot spot stress. This was as seen suitable choice since that stress component is significantly larger than others. Since the boom was equipped with two hot spot strain gauges the calculation results will be compared with the results available from strain gauges.

The stress linearization to find the structural stress components and hot spot stress based on those was performed according to following two equations. Equations used to calculate the membrane and bending stress are shown below and hot spot stress is defined as the sum of membrane and bending stress. (Hobbacher 2016, p. 14)

$$\sigma_m = \frac{1}{t}\int_0^t \sigma(x)\,dx \tag{5}$$

$$\sigma_b = \frac{6}{t^2}\int_0^t (\sigma(x) - \sigma_m)\left(\frac{t}{2} - x\right)dx \tag{6}$$

In equations 5–6 σ_m is membrane stress [MPa], t is the plate thickness [mm], $\sigma(x)$ is normal stress component perpendicular to the weld toe [MPa], x is the coordinate through plate thickness [mm] and σ_b is bending stress [MPa]. (Hobbacher 2016, p. 14)

2.5.3 Effective notch stress method

In the effective notch stress method, the true weld toe and root geometries are replaced with a 1 mm radius. Also, for this method linear material model is assumed. This method is not suitable for cases were large part of the stress acts parallel to the weld toe or material thickness is below 5 mm or where the weld toe or root is not in as welded state. IIW guidelines recommends using flank angle of 30 degrees for butt joints unless there is a reason to assume something else. Since the method is a notch stress method it is not suited for calculating butt joints ground flush with the plate surface and it is recommended to use nominal stress method for those. For the maximum element size in radial and tangential directions at the notch surface IIW recommends 0.25 mm for quadratic elements and 0.15 mm for linear elements. For the ENS method only one fatigue class FAT 255 for principal stress criteria is needed unlike in the previous methods. (Hobbacher 2016, pp. 27–29, 62) Significantly stricter rules for the element size selection for ENS method can be found from literature for example Baumgartner & Bruder (2012, p. 138) recommends element size of 0.05 mm for quadrilateral linear elements.

In this work steeper flank angle will be used based on geometry measurements and element size is set between the recommendations from Hobbacher (2016, p. 29) and Baumgartner & Bruder (2012, p. 138).

2.5.4 4R method

The 4R method is a more comprehensive notch stress method as it takes into account material ultimate strength R_m, applied stress ratio R, residual stress σ_{res} and the true weld toe radius r_{true}. The method was first proposed as 3R method by Nykänen & Björk (2015, 2016) since then the weld toe radius has also been taken into account and the method named 4R method. The 4R method could be seen as an extension of the ENS method. Since it takes into account ENS stress range but also Smith-Watson-Topper equation, Ramberg-Osgood material model and Neuber's rule (Mettänen et al. 2020, p. 3).

The 4R method has been showed to work well in variable amplitude loading. In variable amplitude cases the mean curve is used to calculate the fatigue life estimations for each cycle and Palmgren-Miner's linear damage sum is used estimate the damage. Damage sum value

1 is assumed to correspond to the mean life while 0.174 can be assumed as the characteristic value. n = 0.15 can used as strain hardening exponent and H=1.65R_m as strain hardening coefficient for the Ramberg-Osgood material model. (Nykänen et al. 2017)

Ahola (et al. 2021) analyzed large amount of as welded, ground and ground+peened filled welded joints extracted from literature using the 4R method with success. In that study strain hardening coefficient and strain hardening exponent for Ramberg-Osgood material model were estimated based on the proof and ultimate strength and the plastic strain at yield and failure. (Ahola et al. 2021) Since those assumptions gave successful results same method for estimating the Ramberg-Osgood material model is used in this thesis. Material parameters for Ramberg-Osgood material model can be solved from equation formulated as shown (modified from Ahola et al. 2021, p. 7):

$$\begin{cases} \log_{10}\left(\ln\left(1+\varepsilon_{p0.2}\right)\right) = \frac{1}{n}\left(\log_{10}\left(1+\varepsilon_{p0.2}\right) R_{p0.2} - \log_{10} H\right) \\ \log_{10}(\ln(1+\varepsilon_u)) = \frac{1}{n}\left(\log_{10}(1+\varepsilon_u)\, R_m - \log_{10} H\right) \end{cases} \quad (7)$$

In equation 7, $\varepsilon_{p0.2}$ is 0.2% plastic strain, $R_{p0.2}$ is the proof strength [MPa], n is the strain hardening exponent, H is the strain hardening coefficient [MPa], ε_u is the ultimate strain and R_m the ultimate strength [MPa] (Ahola et al. 2021, p. 7).

For the 4R calculations either plate or cast material parameters were used depending on the weld toe. Strain hardening exponent and strain hardening coefficients were defined based on the average values for proof strength, ultimate strength, and ultimate strain. Material parameters are listed in table 1.

Table 1. Material parameters for the casting and plate material.

	$R_{p0.2}$ [MPa]	R_m [MPa]	ε_u	n	H [MPa]
Strenx 700MC Plus	700[a]	750–950[a]	0.13[a]	0.0764	1127.9
G24Mn6	400–550[b]	600–800[b]	0.12–0.18[b]	0.1237	1026.9

[a] (SSAB 2017, p. 1)

[b] (SFS-EN 10293 2015, p. 10)

In figure 8, the two different ways to define the material model are compared with true stress-strain curve based on tensile test of similar S700 steel. For the comparison Strenx 700MC Plus material parameters are used. As it can be seen the two different methods give quite different stress-strain curve. The curve based on assumption $n = 0.15$ and $H = 1.65R_m$ seems to underestimate yielding. The curve based on calculated n and H values is quite similar to the measured curve although the curved section around 600–800 MPa is much sharper in measured data.

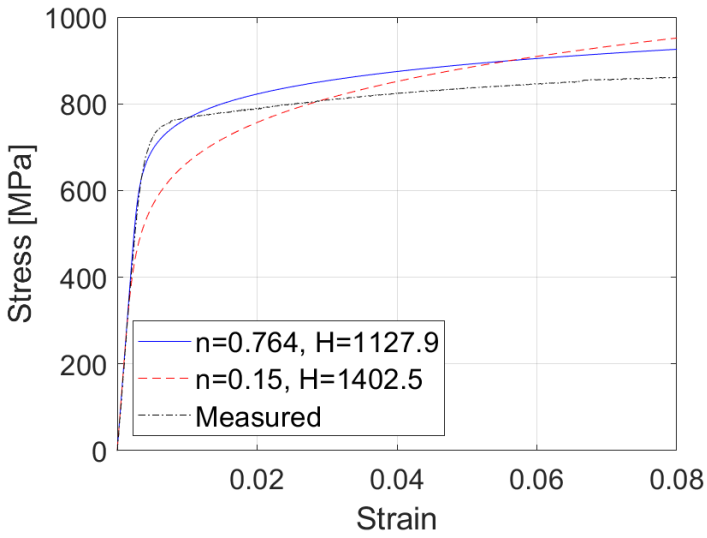

Figure 8. Effect of material parameters on stress-strain curve. Measured values (modified from Amraei et al. 2020).

In the 4R calculations those load cycles that were completely in compression (local stress ratio $R_{local}>1$) were excluded from calculations since the residual stress value is considered in calculations.

Calculation procedure of the 4R method is described below. Here the calculation is showed for single cycle but for variable amplitude loading the same procedure can be looped to go through multiple cycles. Equations for Ramberg-Osgood material model and Neuber's rule are shown below in that order. These two equations can be marked equal and the local maximum stress can be solved. This equation cannot be solved in closed-form so numerical solver can be used. (Nykänen & Björk 2016, pp. 581–582)

$$\varepsilon = \epsilon_e + \epsilon_p = \frac{\sigma_{max}}{E} + \left(\frac{\sigma_{max}}{H}\right)^{\frac{1}{n}} \quad (8)$$

$$\varepsilon = \frac{\left(\frac{\Delta\sigma_k}{1-R} + \sigma_{res}\right)^2}{\sigma_{max}E} \quad (9)$$

In equations 8 and 9 ε is strain, ε_e is elastic strain, ε_p is plastic strain, σ_{max} is local maximum stress [MPa], E is young's modulus [MPa], H strain hardening coefficient [MPa], n strain hardening exponent, $\Delta\sigma_k$ is the linear elastic ENS range [MPa], R stress ratio and σ_{res} residual stress [MPa]. (Nykänen & Björk 2016, pp. 581–582)

Next the local stress range, local minimum stress and local stress ratio will be calculated in that order using following equations. First local stress range is solved using numerical solver by setting cyclic Ramberg-Osgood material model and cyclic Neuber's rule equal. These equations are shown below in corresponding order. (Nykänen & Björk 2016, p. 582)

$$\Delta\varepsilon = \Delta\varepsilon_e + \Delta\varepsilon_p = \frac{\Delta\sigma_{local}}{E} + 2\left(\frac{\Delta\sigma_{local}}{2H}\right)^{\frac{1}{n}} \quad (10)$$

$$\Delta\varepsilon = \frac{{\Delta\sigma_k}^2}{\Delta\sigma_{local}E} \quad (11)$$

In equations 10–11 $\Delta\varepsilon$ is strain range, $\Delta\varepsilon_e$ is elastic strain range, $\Delta\varepsilon_p$ plastic strain range, $\Delta\sigma_{local}$ local stress range [MPa], E is Young's modulus [MPa], H strain hardening coefficient [MPa], n strain hardening exponent and $\Delta\sigma_k$ is linear elastic ENS range [MPa]. (Nykänen & Björk 2016, p. 582)

Equations for minimum local stress and the local stress ratio can be formulated as shown (Nykänen & Björk 2016, p. 582):

$$\sigma_{min} = \sigma_{max} - \Delta\sigma_{local} \quad (12)$$

$$R_{local} = \frac{\sigma_{min}}{\sigma_{max}} \tag{13}$$

In equations 12–13 σ_{min} is the local minimum stress [MPa], σ_{max} is the maximum local stress [MPa] from equations 8–9, $\Delta\sigma_{local}$ local stress range [MPa], and R_{local} is the local stress ratio. (Nykänen & Björk 2016, p. 582)

Following equation is then used to calculate the fatigue life for each of the stress ranges (Nykänen & Björk 2016, p. 582):

$$N_f = \frac{C_{ref}}{\left(\frac{\Delta\sigma_k}{\sqrt{1 - R_{local}}}\right)^m} \tag{14}$$

In the equation 14, N_f is the fatigue life, C_{ref} is the fatigue capacity, m = 5.85 is the slope parameter, R_{local} is the local stress ratio and $\Delta\sigma_k$ is the linear-elastic ENS range [MPa]. As stated earlier mean curve is used to calculate the variable amplitude cases so in this case the C_{ref} is equal to $C_{ref,mean} = 10^{21.59}$. For design life calculations under constant amplitude cases the characteristic curve would be used in those cases the C_{ref} is replaced with $C_{ref,char} = 10^{20.83}$ otherwise the equation stays the same. (Nykänen, Mettänen, Björk, & Ahola 2017, pp. 178–190)

At last, the damage caused by various stress ranges can be combined using Palmgren-Miner's linear damage sum shown in equation 1 just like with the other methods as well.

2.6 FE-modelling

For modeling the notch stress models FEMAP (finite element modeling and postprocessing) software was used. Submodeling technique (also known as breakout modeling) was used to analyze the interesting weld details. Idea in the submodeling is to make it possible to model the global geometry with less fine mesh and with tetrahedral elements to make the meshing easier. After solving the global model its translations can be set as a nodal loads to the sub-models. All analyses were conducted using linear geometry and material models. In the FE-models the Youngs' modulus was set to 210000 MPa and Poisson's ratio as 0.3.

Based on the 3D-scanned welds worst case assumption for the weld geometry was used to model the weld geometries. The front and rear end castings welds were modeled slightly different due to the different material thickness of the casting at the joints. Weld toe radius of 1 mm was assumed for both ENS and 4R methods.

Global model of the beam was modelled using mainly 10-noded parabolic tetrahedral elements but also some 15-noded wedge elements were used at certain transitions and combination of linear beam elements and rigid RBE2 elements were used to model the joints of the beam. The global model of the beam is shown in figure 9. Multiple elements through thickness was set on the locations where the displacements are transferred to the submodels also the mesh density was increased at the location of the LUT-strain gauges.

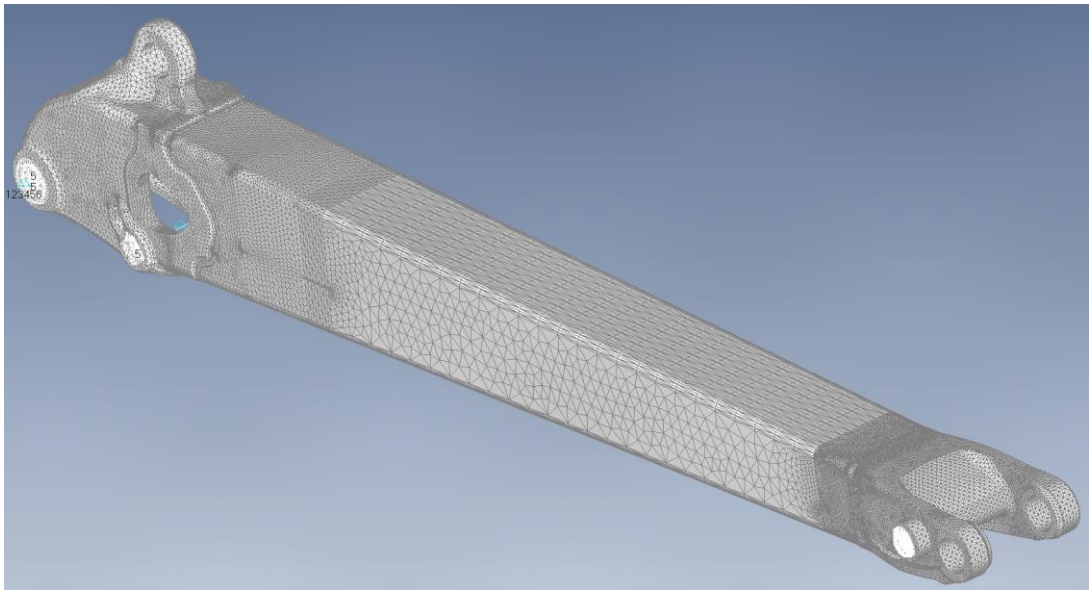

Figure 9. Global model of the beam.

Submodels were created for the welds that join the rear and front end castings to the beam made of plate material. Submodels were constructed using linear 8-noded hexahedral elements and the mesh size at the weld toes and roots was aimed to 0.1 mm in the radial and tangential directions. The element size is significantly smaller than the requirement of the IIW guidelines (Hobbacher 2016, p. 29) but still significantly larger than the 0.05 mm proposed by Baumgartner and Bruder (2012, p. 138). It was seen that due to the size of the component aiming to element size of 0.05 mm would have caused too large model size. The submodels are shown in figure 10.

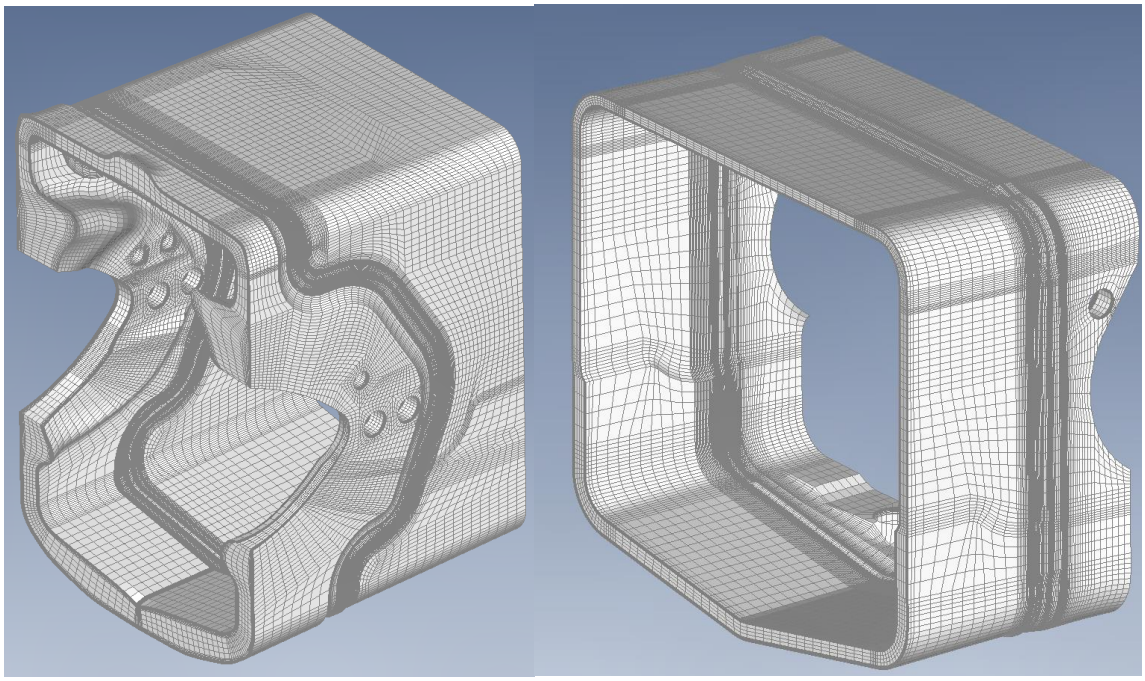

Figure 10. Submodels for the rear and front end castings.

Figure 11 shows the meshing through the thickness at the weld location. Based on arbitrarily measuring the distances between nodes at the weld toes and roots the element size in tangential direction is 0.06–0.12 mm and in radial direction 0.08–0.11 mm. In the submodels the small elements were aimed only at the weld toes and the element size was increased at the middle of the plate. Straight line of nodes was set through the thickness at the weld toes to make it possible to perform stress linearization and calculate the membrane, bending and hot spot stress.

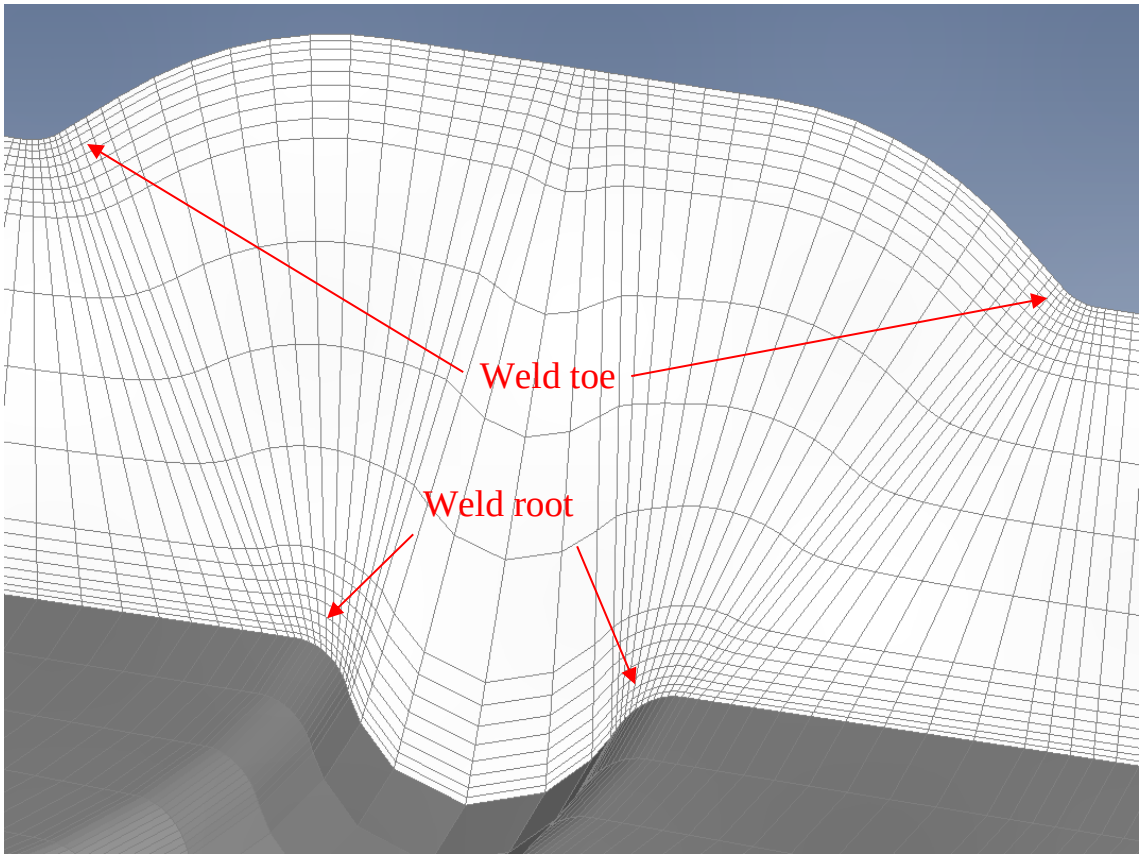

Figure 11. Weld meshing through the thickness.

The critical corners of the welds were modeled as ground since those are also ground in the real lifting boom. For some of the less critical corners the grinding was not modeled to reduce the effort required in the FE-modeling. The material removal was considered based on the maximum grinding depth found from the failure surface. Maximum grinding depth was assumed 1.9 mm in the root side based on measurements. Figure 12 shows how the effect of grinding on the material thickness was considered in the FE-models.

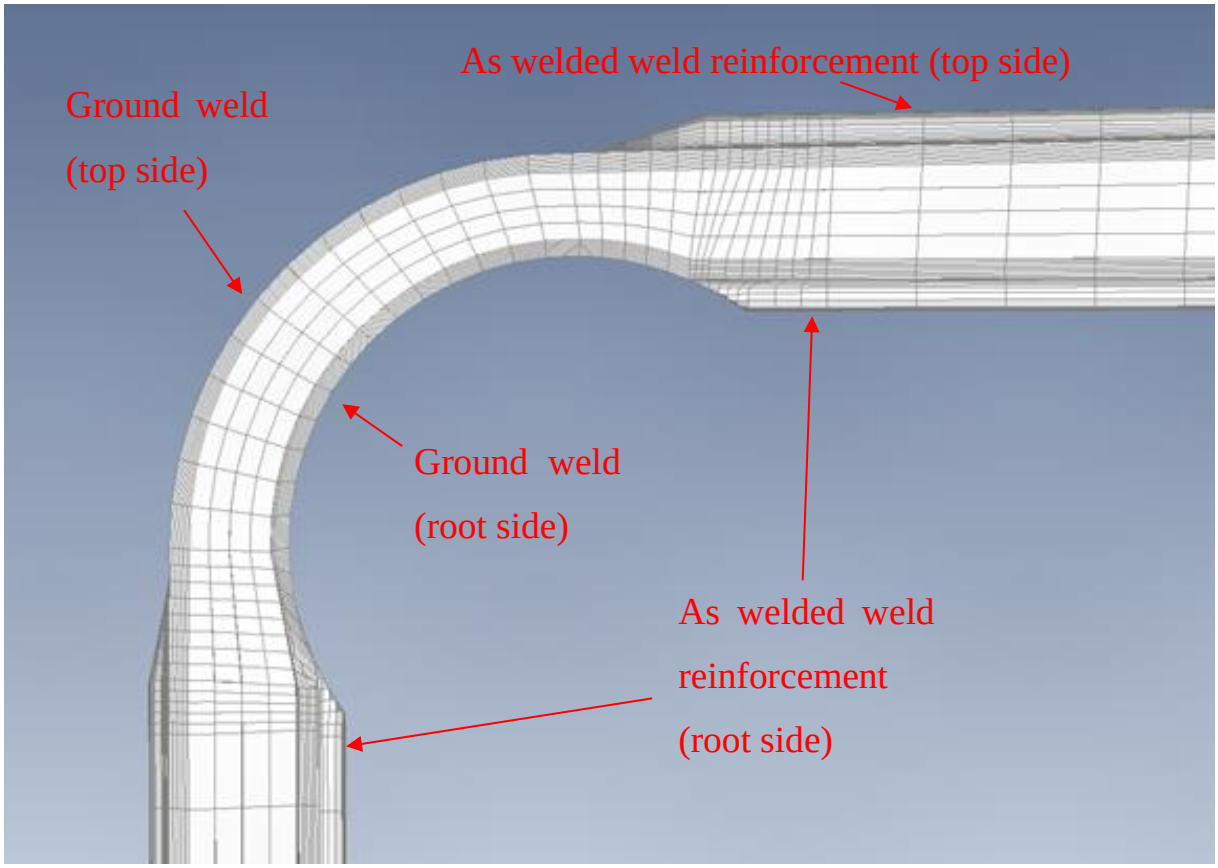

Figure 12. Ground corner of the FE-model.

The finite element models were used to find nodal stresses that can be used in further fatigue calculations. To make these calculations possible unit forces equal to 10 kN were set in the global model and the loads were analyzed one at the time and then superposition principle can be used to combine the results of single forces to find out the stress state of the lifting boom through the given loading history.

For the subsequent calculations nodal stresses are output from FEMAP in suitable coordinate system. Nodal stresses are calculated using average conversion approach with corner results included. This calculates the nodal stress as the average of the surrounding elements corner values.

2.7 Different methods for finding the forces of the beam

Two different methods for solving the forces acting on the beam were compared. These methods are used to find forces at the beam based on strain gauge data and based on that implement unit force method for fatigue assessment.

2.7.1 True-Load

True-Load is a commercial software that finds optimized locations for strain gauges based on a FE-model. Then after inputting the strain gauge data back to the software it calculates back load time histories that can be used in for example in fatigue analysis. In this case the True-Load is used to calculate load time histories for 9 different loads of the lifting boom. Figure 13 shows the location and direction of the forces generated by the True-Load. 10 kN was used as the unit force for each of the forces of the beam and True-Load gives multipliers for each of those forces in a table form.

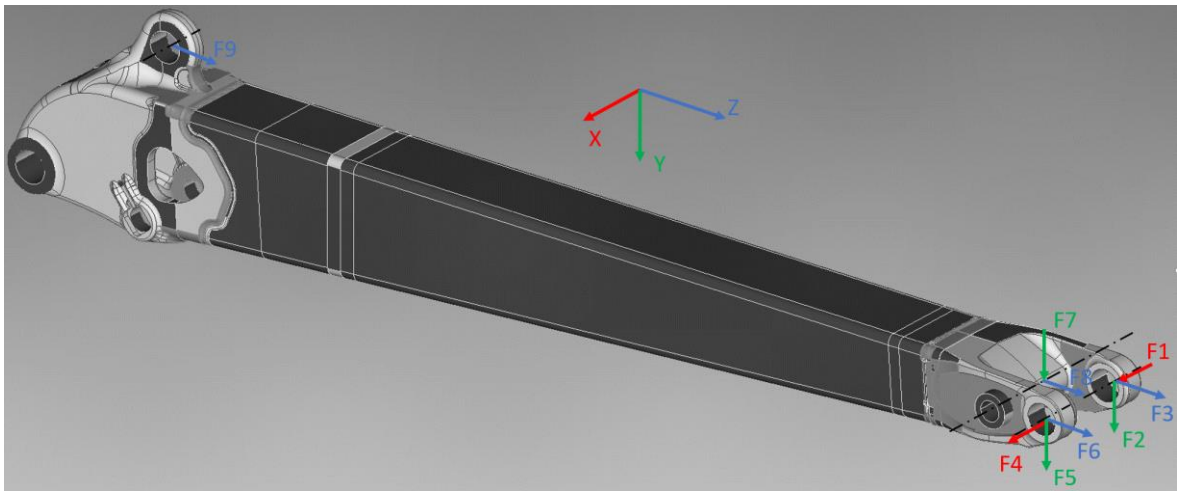

Figure 13. Forces from the True-Load.

The principal stresses for each time step were calculated based on the stress components from finite element model and multiplying those with force multipliers from the True-Load. Following equation shows how the stress components for one time step and node are calculated based on the FE-results and True-Load multipliers:

$$\begin{bmatrix}\sigma_x\\ \sigma_y\\ \sigma_z\\ \tau_{xy}\\ \tau_{yz}\\ \tau_{zx}\end{bmatrix} = F_1\begin{bmatrix}\sigma_{x,F1}\\ \sigma_{y,F1}\\ \sigma_{z,F1}\\ \tau_{xy,F1}\\ \tau_{yz,F1}\\ \tau_{zx,F1}\end{bmatrix} + F_2\begin{bmatrix}\sigma_{x,F2}\\ \sigma_{y,F2}\\ \sigma_{z,F2}\\ \tau_{xy,F2}\\ \tau_{yz,F2}\\ \tau_{zx,F2}\end{bmatrix} + F_3\begin{bmatrix}\sigma_{x,F3}\\ \sigma_{y,F3}\\ \sigma_{z,F3}\\ \tau_{xy,F3}\\ \tau_{yz,F3}\\ \tau_{zx,F3}\end{bmatrix} + F_4\begin{bmatrix}\sigma_{x,F4}\\ \sigma_{y,F4}\\ \sigma_{z,F4}\\ \tau_{xy,F4}\\ \tau_{yz,F4}\\ \tau_{zx,F4}\end{bmatrix} + F_5\begin{bmatrix}\sigma_{x,F5}\\ \sigma_{y,F5}\\ \sigma_{z,F5}\\ \tau_{xy,F5}\\ \tau_{yz,F5}\\ \tau_{zx,F5}\end{bmatrix} + F_6\begin{bmatrix}\sigma_{x,F6}\\ \sigma_{y,F6}\\ \sigma_{z,F6}\\ \tau_{xy,F6}\\ \tau_{yz,F6}\\ \tau_{zx,F6}\end{bmatrix} +$$

$$F_7\begin{bmatrix}\sigma_{x,F7}\\ \sigma_{y,F7}\\ \sigma_{z,F7}\\ \tau_{xy,F7}\\ \tau_{yz,F7}\\ \tau_{zx,F7}\end{bmatrix} + F_8\begin{bmatrix}\sigma_{x,F8}\\ \sigma_{y,F8}\\ \sigma_{z,F8}\\ \tau_{xy,F8}\\ \tau_{yz,F8}\\ \tau_{zx,F8}\end{bmatrix} + F_9\begin{bmatrix}\sigma_{x,F9}\\ \sigma_{y,F9}\\ \sigma_{z,F9}\\ \tau_{xy,F9}\\ \tau_{yz,F9}\\ \tau_{zx,F9}\end{bmatrix} = \sum_{i=1}^{9}\left(F_i\begin{bmatrix}\sigma_{x,Fi}\\ \sigma_{y,Fi}\\ \sigma_{z,Fi}\\ \tau_{xy,Fi}\\ \tau_{yz,Fi}\\ \tau_{zx,Fi}\end{bmatrix}\right) \quad (15)$$

In equation 15 F_i are the force multipliers from True-load, $\sigma_{x,i}$, $\sigma_{y,i}$, $\sigma_{z,i}$, $\tau_{xy,i}$, $\tau_{yz,i}$, $\tau_{zx,i}$ are the stress components corresponding to specific load from FE-model [MPa] and σ_x, σ_y, σ_z, τ_{xy}, τ_{yz}, τ_{zx} are the total stress components at specific time and node [MPa].

Principal stresses are the eigenvalues of the stress components matrix. Principal stresses can then be calculated using equation: (Young & Budynas 2002, pp. 24–25)

$$\begin{bmatrix}\sigma_1\\ \sigma_2\\ \sigma_3\end{bmatrix} = eig\begin{pmatrix}\sigma_x & \tau_{yx} & \tau_{zx}\\ \tau_{xy} & \sigma_y & \tau_{zy}\\ \tau_{xz} & \tau_{yz} & \sigma_z\end{pmatrix} \quad (16)$$

In equation 16, σ_1, σ_2 and σ_3 are the principal stresses [MPa] while σ_x, σ_y, σ_z, τ_{yx}, τ_{zx}, τ_{xy}, τ_{zy}, τ_{xz}, τ_{yz} are the corresponding stress components [MPa] solved from the equation 15. (Young & Budynas 2002, pp. 24–25)

For the further calculations principal stresses are used. Since the sign of the principal stress can change the principal stress with highest absolute value is used in calculations. Rainflow analysis is conducted for the vector of principal stresses with highest absolute values through time.

For the ENS, hot spot and nominal stress methods the knee point in the S-N curves is taken into account and the stress ranges are divided to values above knee point and below knee point and the fatigue lifes and Palmgren-Miner's damage sums are calculated separately using corresponding slopes. After calculating the damage sums those can be added together.

2.7.2 Simplified method with 8 strain gauges

Another idea for finding the forces for the unit force method was measuring strains with 8 strain gauges in a single cross-section of the beam. Four of the strain gauges are used to measure normal stresses and the remaining four shear stresses. Figure 14 shows schematic of the location of the strain gauges in the cross section. The cross-section plane where the 8 strain gauges are located is referred as LUT plane. Green markings describe normal stress gauges and red ones shear stress gauges. Based on the strains the force components of a beam cross-section can be calculated including axial force, two bending moments, torsional moment, two shear forces, and bimoment. Therefor the loading of a simple boom structure could be defined with relatively simple system of strain gauges. This method also gives good insight on the force components that the boom experiences during the loading. Drawback of this method is that it requires some work to formulate the equations into suitable form while using software like True-Load performs that phase itself. Also, for complex load cases this system is not suitable and for example in this case it does not take the cylinder force at the rear end casting into account. Although the local effects caused by the cylinder force can be measured using hot spot strain gauges if such locations are considered as interesting. The external forces determined by this method and used for the fatigue calculations are shown in figure 15. Those forces will be referred to in equations below.

Axial strains are measured using quarter-bride system. Shear strains are measured using half-bridge system that filters out other stress components and gives directly the shear strain values. To calculate the normal stresses based on strains Young’s modulus of 210 GPa was used. The shear modulus for calculating shear stresses was defined based on the Young’s modulus and Poisson’s ratio of 0.3 and is 81 GPa.

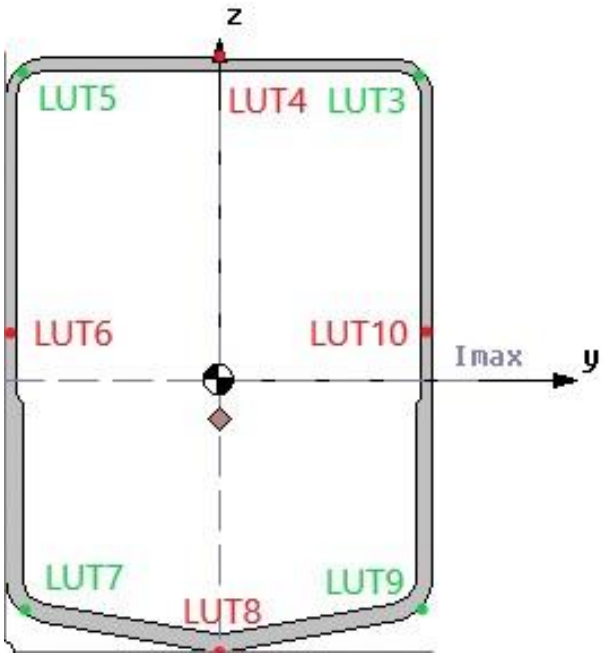

Figure 14. Location of the LUT strain gauges in the cross section looking from the front of the boom.

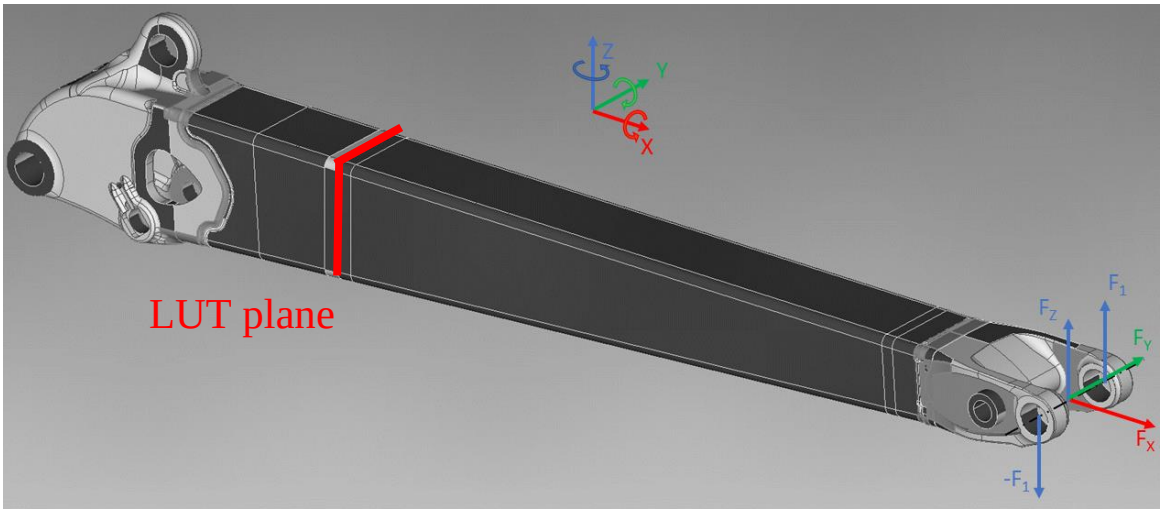

Figure 15. External forces and their positive directions used in this method.

To solve the normal force, bending moments and bimoment in the cross-section following system of equations was formulated. Cross-sectional properties required in the calculations were achieved from software including FEMAP and AGIFAP (Advanced Graphical Interactive Frame Analysis Package).

$$\begin{cases} \varepsilon_{LUT3} = \frac{N}{EA} + \frac{M_{yy} z_{LUT3}}{I_{yy} E} - \frac{M_{zz} y_{LUT3}}{I_{zz} E} + \frac{B_\omega \omega_{LUT3}}{E I_\omega} \\ \varepsilon_{LUT5} = \frac{N}{EA} + \frac{M_{yy} z_{LUT5}}{I_{yy} E} - \frac{M_{zz} y_{LUT5}}{I_{zz} E} + \frac{B_\omega \omega_{LUT5}}{E I_\omega} \\ \varepsilon_{LUT7} = \frac{N}{EA} + \frac{M_{yy} z_{LUT7}}{I_{yy} E} - \frac{M_{zz} y_{LUT7}}{I_{zz} E} + \frac{B_\omega \omega_{LUT7}}{E I_\omega} \\ \varepsilon_{LUT9} = \frac{N}{EA} + \frac{M_{yy} z_{LUT9}}{I_{yy} E} - \frac{M_{zz} y_{LUT9}}{I_{zz} E} + \frac{B_\omega \omega_{LUT9}}{E I_\omega} \end{cases} \quad (17)$$

In the equation 17, the ε_{LUT3}–ε_{LUT9} are the strain values from the measurements, N is normal force [N], E is Young's modulus [MPa], A is the cross-section area [mm], M_{yy} is bending moment around y-axis [Nmm], I_{yy} is the second moment of area around y-axis [mm^4], z_{LUT3}–z_{LUT9} are the z-coordinates corresponding to the gauges [mm], M_{zz} is the bending moment around z-axis [Nmm], y_{LUT3}– y_{LUT9} are the y-coordinates corresponding to the gauges [mm], I_{zz} is second moment of area around z-axis [mm^4], B_ω is the bimoment [Nmm^2], ω_{LUT3}–ω_{LUT9} are sectorial coordinates corresponding to strain gauge in question [mm^2] and I_ω is the warping constant [mm^6]. The positive and negative directions are considered in the coordinates of the strain gauges and therefor the signs of the equation 17 match but if calculations are performed in different coordinate system the signs would differ.

Next the external forces can be calculated based on normal force and bending moment equations.

$$F_x = N \quad (18)$$

$$F_z = \frac{M_{yy} - F_x Z_1}{-X} \quad (19)$$

$$F_y = \frac{M_{zz}}{X} \quad (20)$$

In equations 18–20 F_x is the external force in x-direction [N], N is the normal force [N], F_z is the external force in z-direction [N], M_{yy} is bending moment around y-axis [Nmm], Z_1 is z-distance between the bearing and the center of mass of the LUT-plane [mm], X is the x-

distance between the bearing and LUT-plane [mm], F_y is the force in y-direction [N] and M_{zz} is the bending moment around z-axis [Nmm].

In addition to these three forces a pair of equal and opposite forces is used to generate the torsion in the lifting boom. The torsion in the cross-section is defined based on the average torsional moment calculated for each of the shear strain gauges. This calculation procedure is shown in following equations:

$$\begin{bmatrix} T_{LUT4} \\ T_{LUT6} \\ T_{LUT8} \\ T_{LUT10} \end{bmatrix} = \begin{bmatrix} \left(\tau_{LUT4} + \frac{F_y S_{LUT4,LUT8}}{I_{zz} t_4}\right) 2A_m t_1 \\ \left(\tau_{LUT6} - \frac{F_z S_{LUT6,LUT10}}{I_{yy} t_3}\right) (-2A_m t_1) \\ \left(\tau_{LUT8} - \frac{F_y S_{LUT4,LUT8}}{I_{zz} t_4}\right) 2A_m t_2 \\ \left(\tau_{LUT10} + \frac{F_z S_{LUT6,LUT10}}{I_{yy} t_3}\right) (-2A_m t_1) \end{bmatrix} \tag{21}$$

$$T_{avg} = \frac{T_{LUT4} + T_{LUT6} + T_{LUT8} + T_{LUT10}}{4} \tag{22}$$

$$F_1 = \frac{T_{avg}}{2Y} \tag{23}$$

In the equations 21–23, T_{LUT4}–T_{LUT10} are the torsional moments corresponding to the strain gauges [Nmm], τ_{LUT4}–τ_{LUT10} are the shear stresses corresponding to the measured strain gauge values [MPa], F_y is the force in y-direction [N], F_z is the external force in z-direction [N], $S_{LUT4,LUT8}$ is the first moment of area at LUT4 and LUT8 locations [mm^3], A_m is the area enclosed by the cross-sectional center line [mm^2], t_1 is the wall thickness at LUT4, LUT6 and LUT10 [mm], $S_{LUT6,LUT10}$ is the first moment of area at LUT6 and LUT10 location [mm^3], t_2 is the plate thickness at LUT8 [mm], t_3 is combined wall thickness of LUT6 and LUT10 locations [mm], t_4 is combined wall thickness of LUT4 and LUT8 locations [mm], I_{yy} is the second moment of area around y-axis [mm^4], I_{zz} is second moment of area around z-axis [mm^4], T_{avg} is the average torsional moment in the cross-section [Nmm], Y is half of the bearing distance in y-direction [mm] and F_1 is the force causing the torsion [N].

After calculating the external forces similar calculation procedure can be followed as in the case of True-Load. Difference was that the True-Load gives external forces automatically and, in this case, you need to solve those by yourself.

3 RESULTS

In the subsections below results from various measurements, analyses and calculations are discussed in detail. Calculation results are presented as Palmgren-Miner's sum distributions at the toes and as stress range distributions at the node that has highest damage sum. Various graphs are used to compare measured values and calculation results. The most important results are shown in the text and less important ones are included in appendices.

3.1 Experimental testing

Experimental testing included weld geometry measurements, residual stress measurements and fracture surface analysis. Geometry measurements were required for FE-modeling the weld joints. Residual stress measurements were used to find residual stress value used in 4R calculations and to compare two different lifting boom designs. Fracture surface analysis was conducted to get information of the fatigue failure. Results of the experimental testing are described below.

3.1.1 Weld geometry

Based on the weld geometry measurements worst case assumption for the weld geometry was formed and that was used in the FE-modeling. The dimensions for the FE-modeling was set as follows r_{true} = 0 mm, flank angle of the weld top surface 43 degrees, flank angle of the root 76 degrees, top side weld reinforcement width 18.2 mm and root side weld reinforcement width 4.8 mm. The dimensions are illustrated in figure 16. For both front end and rear end castings the root geometry was considered similar, but the surface geometry had to be modified slightly due to different thickness of the casting. All the welded corners of the boom were ground from both sides and from the fracture surface and scanned data it was obvious that the grinding had formed a dimple in the root sides. Grinding depth at the weld roots was examined based on the scanned data but eventually the maximum grinding depth was found from the fracture surface and could be measured using calipers. Grinding depth measured at the fracture surface was 1.9 mm.

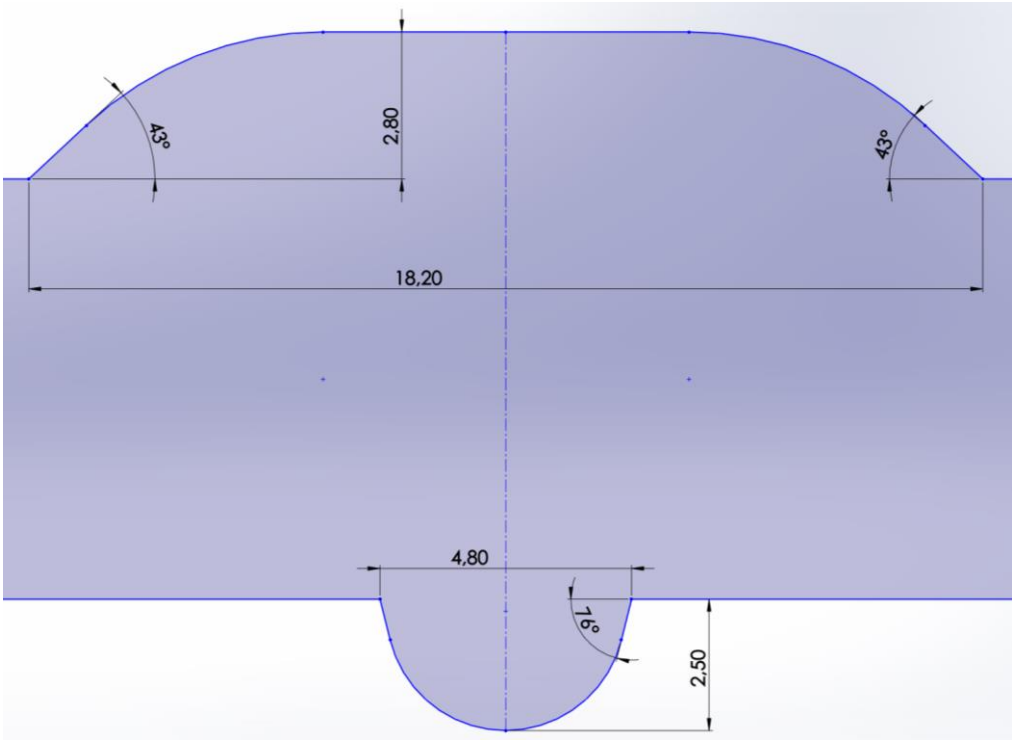

Figure 16. Assumed weld geometry at rear end casting.

3.1.2 Residual stresses

Measured residual stressed at weld toes can be seen in appendix I. Based on the residual stress measurements the residual stresses are low and mainly compressive although it can be seen that the grinding caused tensile residual stresses. From the appendix I it can be seen that tensile residual stresses can be seen at the rear end castings in the middle of the web, front end castings web and the front end castings ground corner. The older design had also tensile residual stresses in the middle of the flange at rear end casting in front of the cylinder bracket. Refer to figures 3–5 (pages 15–16) for the naming of the measurement locations.

As said earlier few residual stress distributions perpendicular to the weld toe was measured. Figure 17 shows the residual stress distributions. It can be seen from the figure that the highest tensile residual stresses are at the ground area. Also, tensile residual stresses are at the middle of the web in the rear end castings tip.

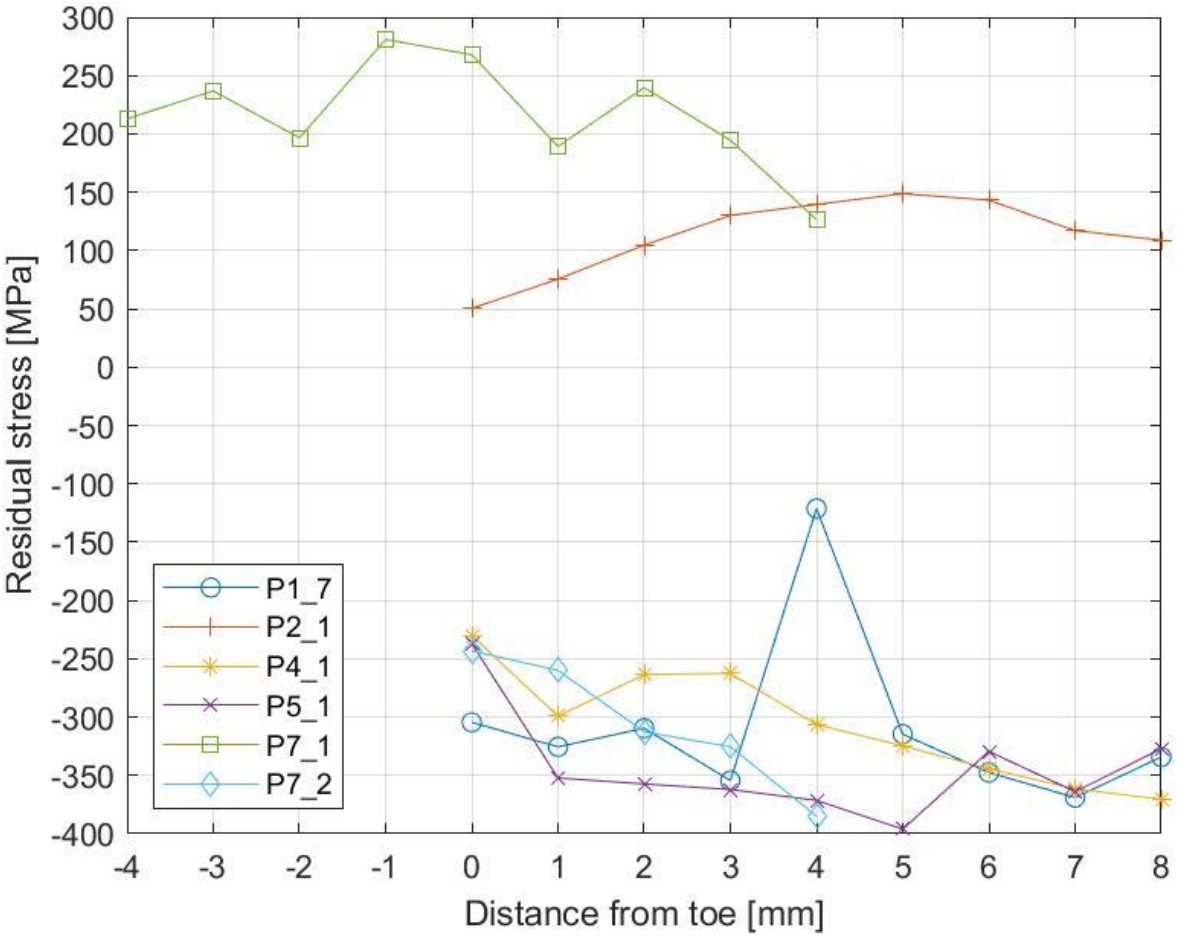

Figure 17. Residual stress distributions.

In figure 18 residual stress values measured before and after fatigue testing are drawn into a single graph. It can be seen that the fatigue testing has not had significant effect on the residual stress values and the values follow similar pattern in both cases.

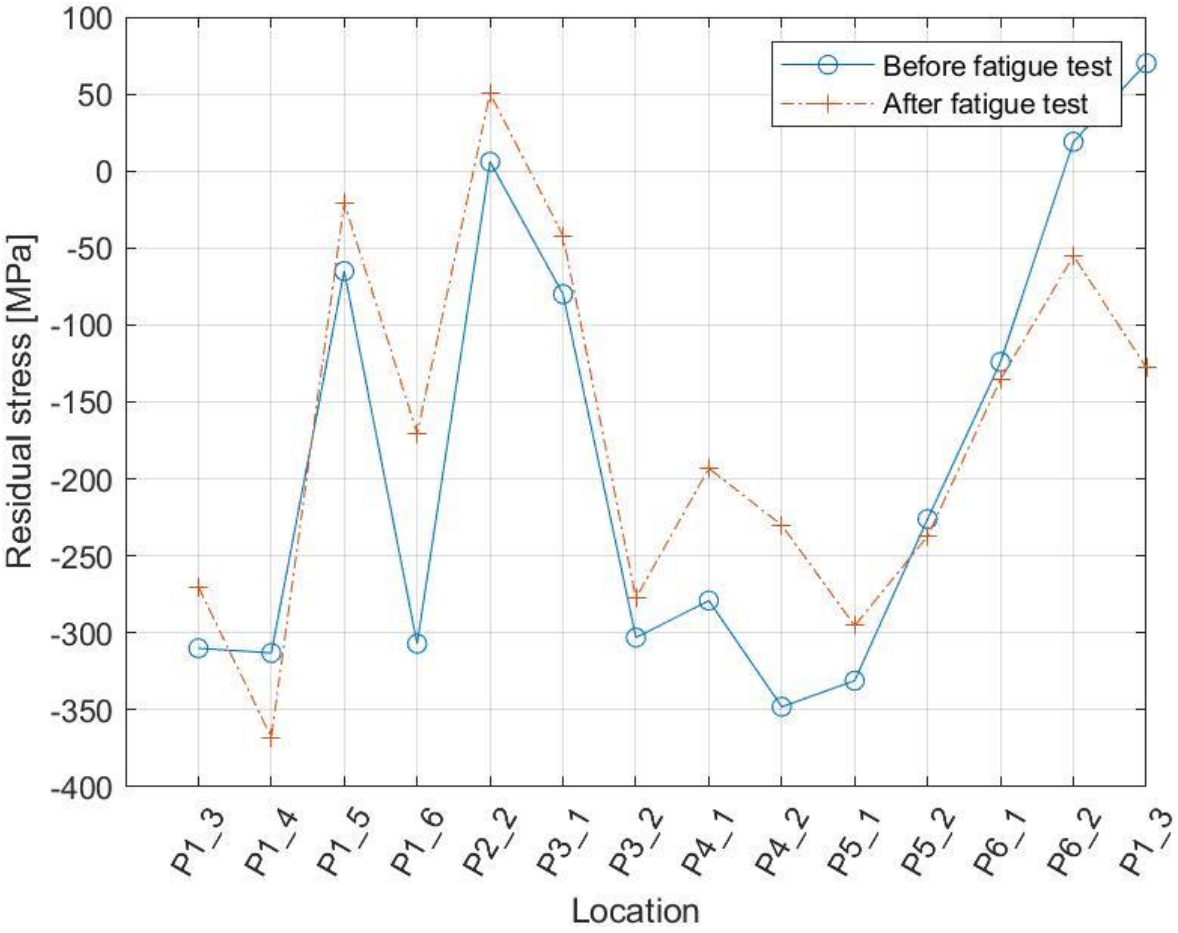

Figure 18. Residual stress relaxation.

3.1.3 Comparison of the two beam designs

To assist in comparing the residual stress states after welding in the two different design versions of the boom figure 19 was drawn. From that figure it can be seen that the residual stresses follow similar pattern. The biggest differences at locations P1_5, P2_1 and P2_2 are the ones that the largest design changes occurred. Since the residual stresses in the newer design are more compressive based on this graph it could be said that the design chance seems to have had a positive impact on the residual stress state although the amount of measurements is not high enough to make conclusive statements.

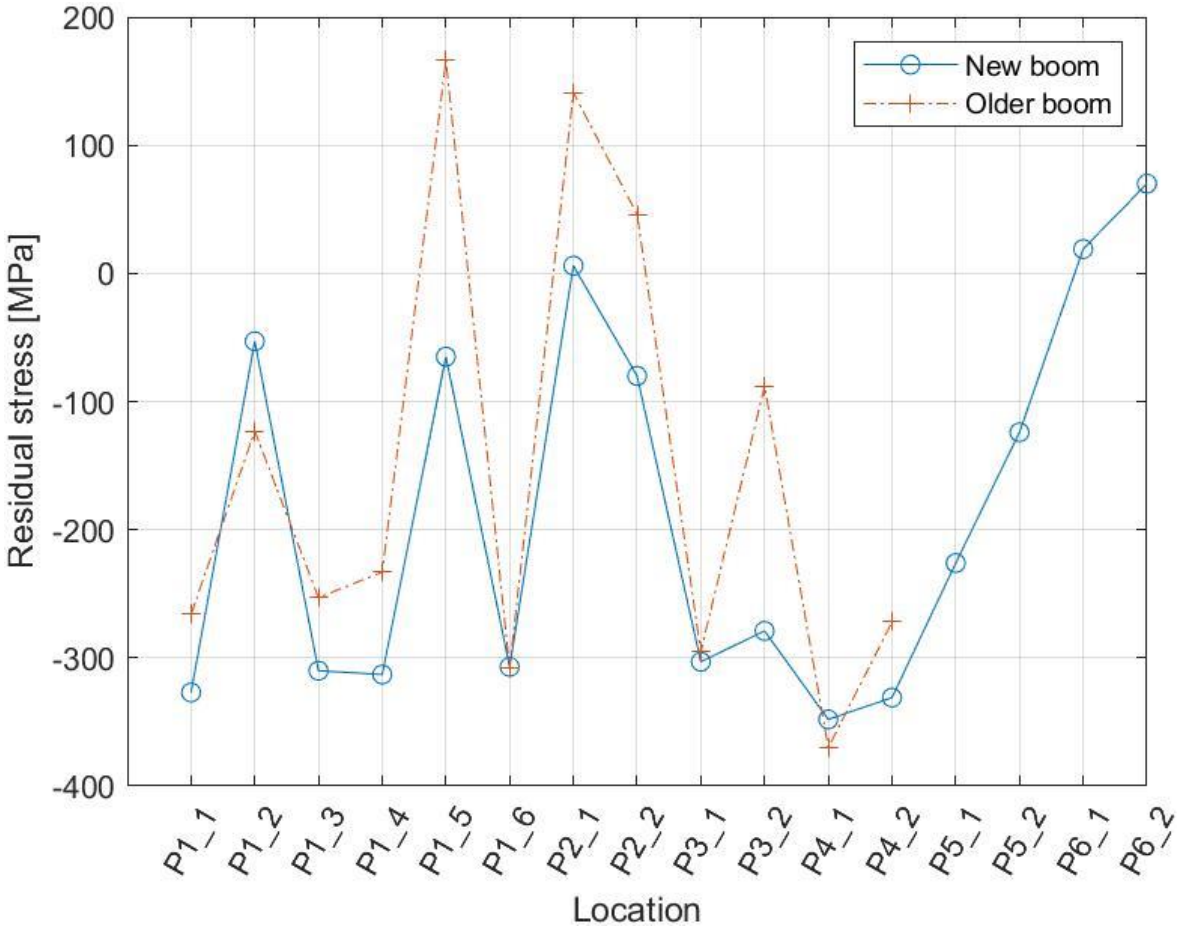

Figure 19. Residual stress state after welding in both boom versions.

3.1.4 Fracture surface analysis

The fracture surface was examined with optical microscope as well as scanning electron microscope (SEM). Figure 20 taken with profilometer shows clearly how fatigue cracks have grown in two different planes and then merged forming a highly visible ridge in the surface (pointed with arrow). Figure 21 is taken from the location pointed by the same arrow. Already from figure 20 it is clearly visible that the crack initiation and growth has started from the root side. The root side has smoother slow crack growth area and the surface side is coarser due to faster crack growth. In the figure 20 the web of the beam is to the right and the upper flange of the beam would be on the left.

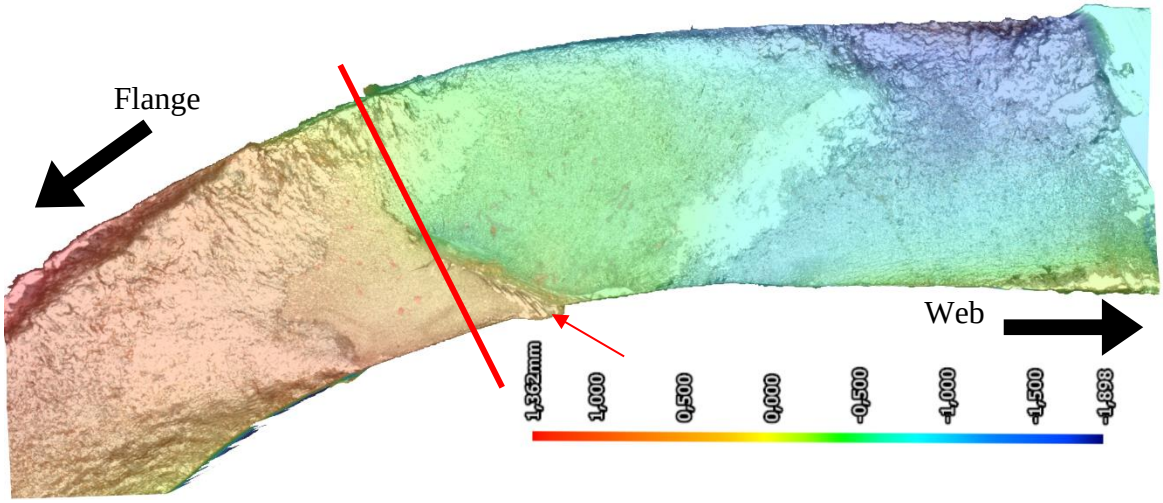

Figure 20. Profilometer picture of the fracture surface.

Some of the crack growth can be seen from figure 21. Crack propagation marks can be seen starting from the root surface and the side of the ridge. Crack growth along the side of the ridge is quite odd and at this point it is impossible to say for sure in which order the crack initiation and growth has happened. It is also clear that there exists more than one crack growth and initiation location since otherwise such ridge in the fracture surface would not form but clear crack propagation marks cannot be seen elsewhere in the fracture surface.

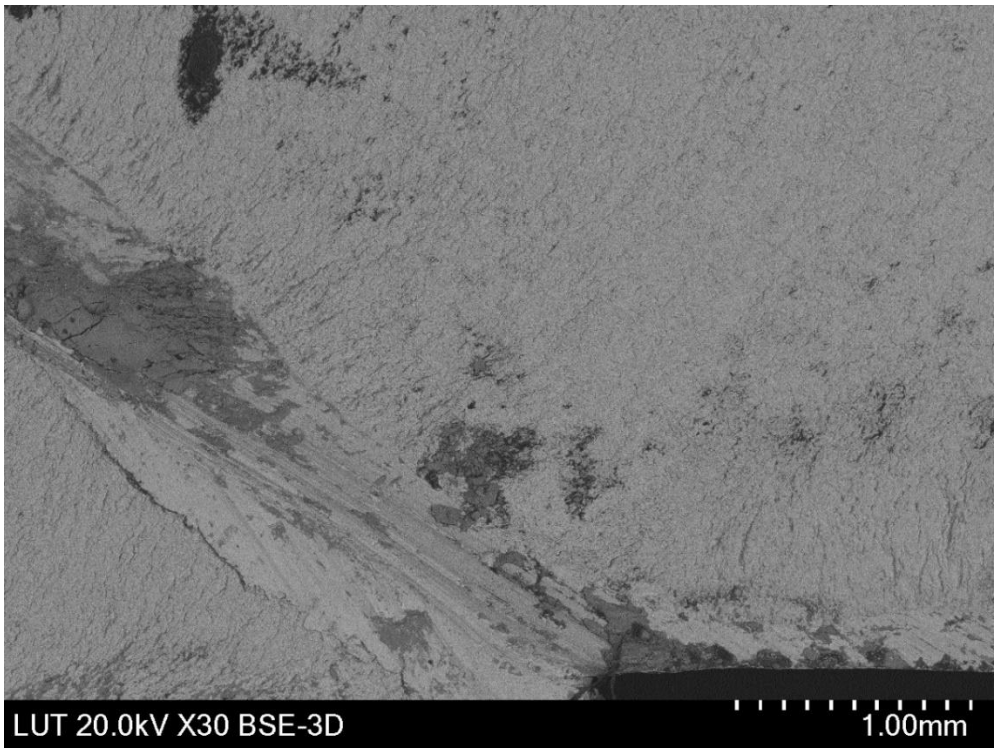

Figure 21. SEM picture of the crack growth at the ridge.

To get more information of the crack growth a macro section was manufactured from the location shown in figure 20 with red line. The ridge can be seen in the middle of the plate thickness on the right side. Reason for why the ridge is not visible in the left side of the figure 22 is probably in the alignment of the pieces during the manufacturing of the macro section since similar pattern occurred at both sides of the fracture surface. Macro section can be seen in figure 22. In the figure 22, some lack of fusion between the weld beads is shown in the detailed microscope image in the corner, but this has clearly nothing to do with the fatigue failure since it is in different plane.

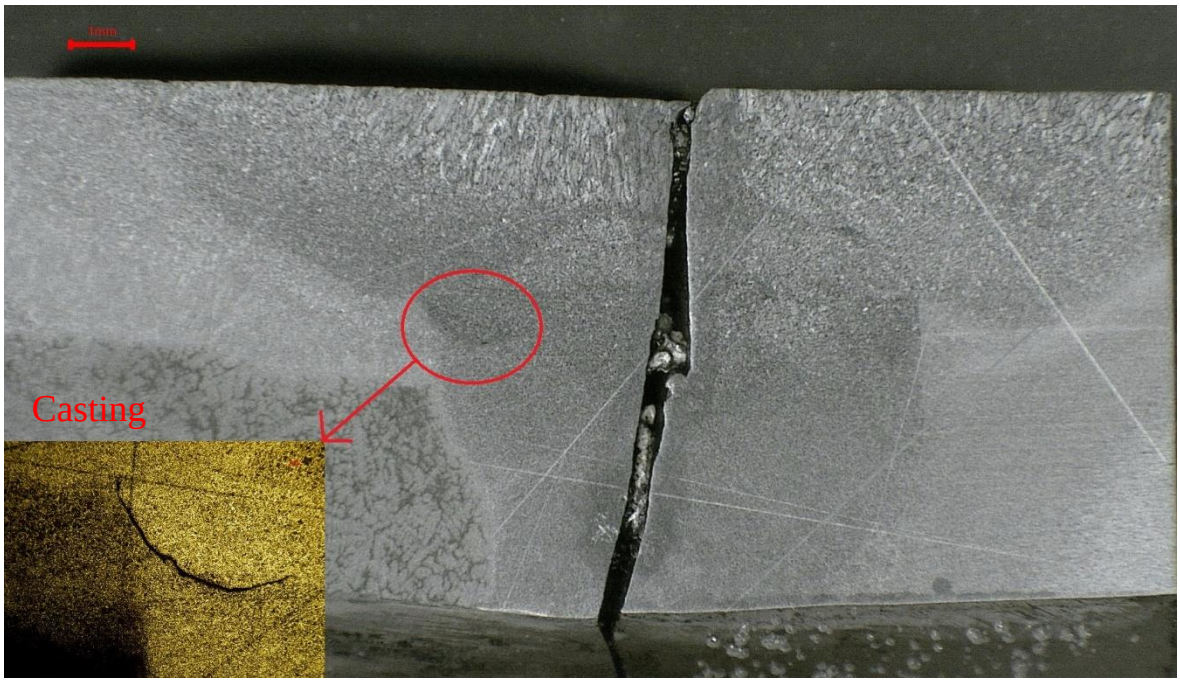

Figure 22. Macro section of the fracture.

Fatigue cracks have initiated and grown from the root side of the ground weld joint located at the corner of the boom. In addition to that it is difficult to say much more than fatigue cracks have initiated in more than one location and then merged together forming the visible ridge.

3.2 Comparison of strain gauge measurements and calculation results

To validate the True-Load and 8-strain gauge calculations simple comparison was performed with the LUT strain gauges measuring normal and shear stresses and the corresponding stress components calculated using the forces from the True-Load and 8-strain gauge methods.

Results of this comparison are included in figure 23. Similar comparison was also done with shear stresses but since the normal stresses are significantly higher only those are shown here and graphs for shear stresses are shown only in appendix II. The figure 23 and the shear stress graphs can be seen in larges size in appendix II. From figure 23 it was noted that the strain gauges LUT7 and LUT9 at the bottom corners corresponded very well to the values calculated based on both methods. In the results based on True-Load the strain gauges LUT3 and LUT5 at the top flange both had similar offset of bit over 20 MPa compared to the measured strain gauge values. This kind of offset is not visible in the results of the 8-strain gauge method and the calculation results correspond almost identically to the measured values. Also, from the figure 23 it can be clearly seen that the True-Load overestimates some of the stress spikes quite significantly. Despite the previous observations the results based on the strain gauges and True-Load seem to follow similar trend.

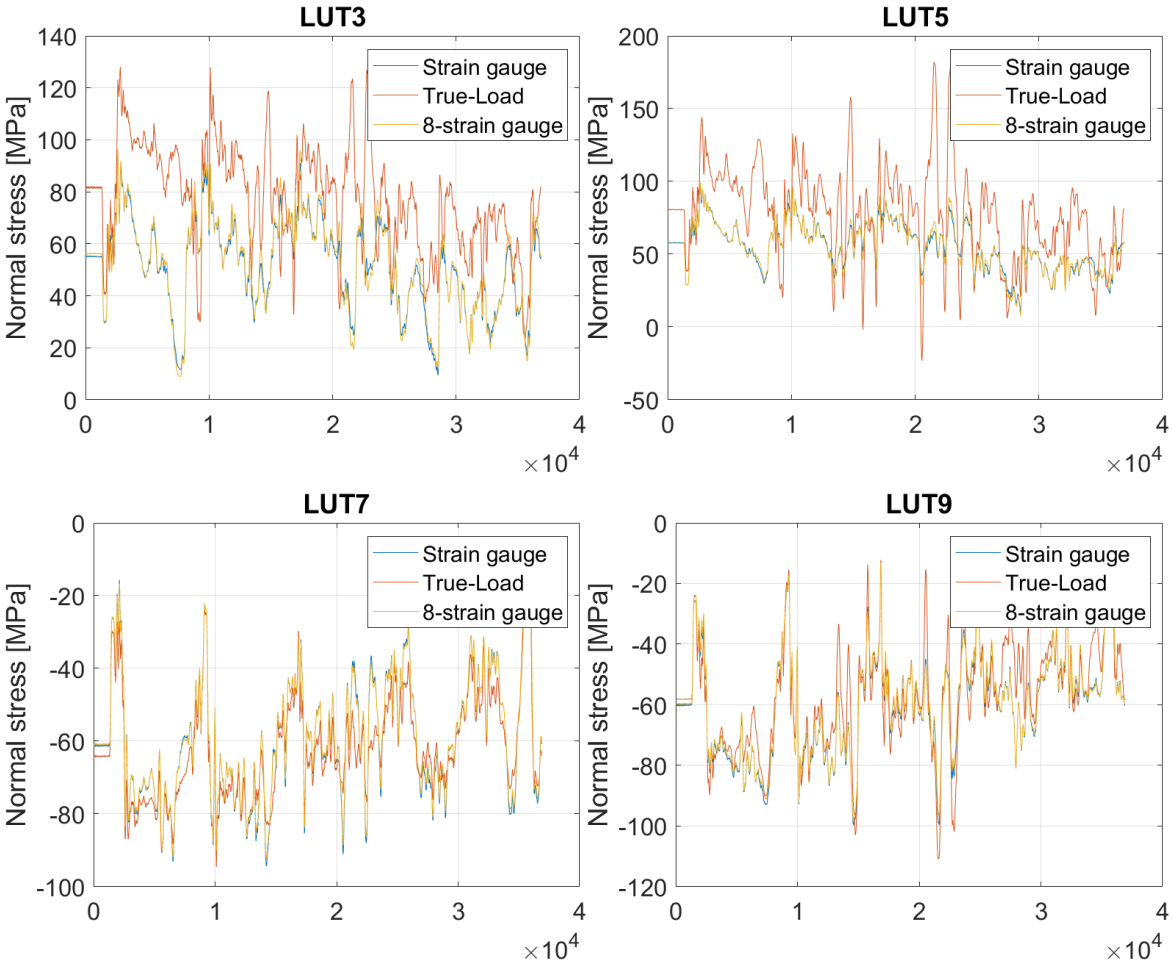

Figure 23. Calculated and measured nominal stress compared.

By looking at appendix II it can be seen that the 8-strain gauge method corresponds very well with both normal and shear strain gauge measurements at the LUT plane. Similarly, it can be seen that the result match very well also at the LUT2 hot spot strain gauge as shown in figure 29 (page 51). As seen from the graphs of appendix II and figure 29 the shear, normal and hot spot stresses are almost identical with the measured strain data.

3.3 Fatigue strength assessment

Results of the different fatigue assessment methods are gone through in the chapters below. Results are compared with strain gauge data when possible. Results for more critical toes of both two welds are shown and the results for other toes are shown in appendices.

3.3.1 Results of nominal stress method

Nominal stress method was used to calculate only the ground corners since the notch stress methods are not suitable for those. Figure 24 shows the Palmgren-Miner's damage sum distribution for the most critical weld toe based on True-Load. Similar damage sum distributions for other toes are shown in appendix VI and appendix VII based on design and mean S-N curves correspondingly. It can be seen that the calculation results would point the right corner as the most critical, but the fatigue failure occurred at the left corner. Based on the mean S-N curve the maximum damage sum at the left corner was 0.28. Design rules recommend damage sum 0.5 for variable amplitude loading or even 0.2 in case of fluctuating mean stress (Hobbacher 2016, p. 93). Based on that it seems that the result is relatively well in line with the IIW recommendation while the opposite corner seems to have had very good fatigue life.

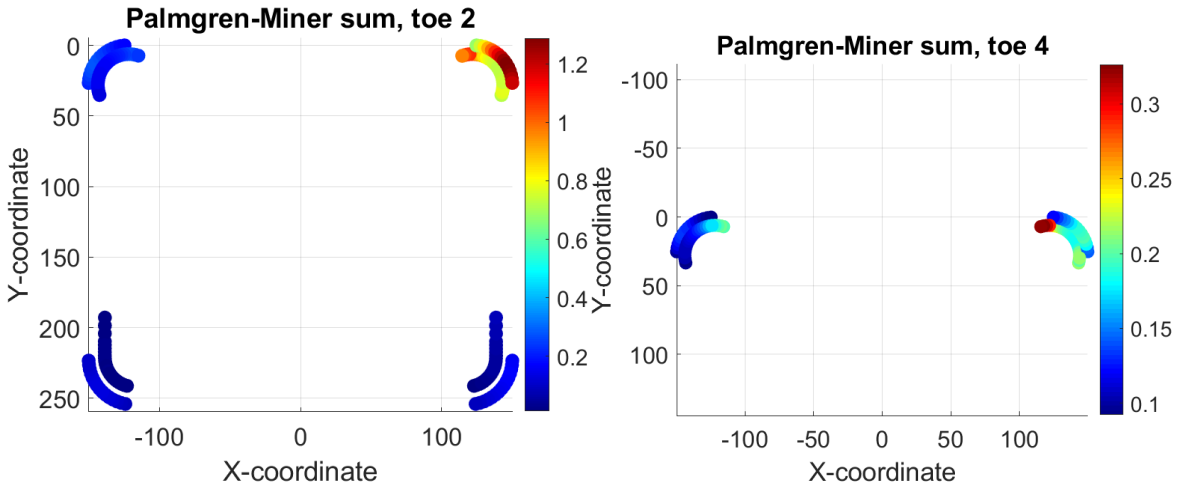

Figure 24. Critical weld toes damage sum distributions based on True-Load and mean S-N curve.

The stress range distributions based on True-Load for the most loaded node of the toes can be seen in appendix VIII.

Appendix III and IV include the Palmgren-Miner's sum distributions calculated for each of the ground corners using the 8-strain gauge method and nominal stress method with both design and mean S-N curves. The most critical toes of both welds are also shown in figure 25. As it can be seen comparing these results to the results based on True-Load (figure 24) the damage sums based on 8-strain gauge method are significantly lower especially at the front end casting. As it has been already discussed the True-Load tends to overestimate some of the stress peak causing larger damage sums but the differences at the front end casting are too high to be explained just by that. The stress range distribution for one test load at the most loaded node of the weld toes can be seen in appendix V.

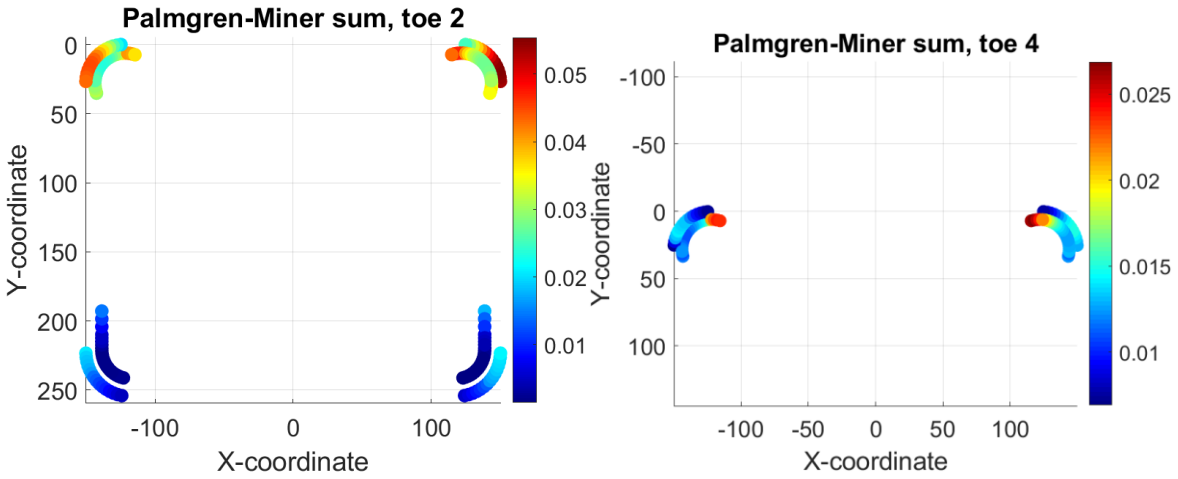

Figure 25. Critical weld toes damage sum distributions based on 8-strain gauge method and mean S-N curve.

It seems that the 8-strain gauge method is not valid at the front end casting even though it seems to give good correspondence with the strain gauge results at the rear end casting. This might be due to the fact that the method is based on measurements close to the rear end casting.

At the rear end casting the result of True-Load and 8-strain gauge method seem to be closer as it can be seen by comparing appendices III–VII but the differences are still significant.

3.3.2 Results of hot spot method

As it was known that the asymmetry of the loading changes during the fatigue testing the effect of that was taken into account by taking the strain gauge data from different days of the fatigue testing. First data set was taken from the beginning of the test, second from the middle of the test and last from the end of the test. It was assumed that all these cycles are ran one third of the whole test. These three cycles are shown in figure 26 and were used to calculate the values of table 2. This procedure was not possible for the other fatigue assessment methods due to the lack of strain gauge data.

Table 2 shows the Palmgren-Miner's sums for the three different cycles based on hot spot strain gauges, calculations based on True-Load and 8-strain gauge method. From the table 2 it can be seen that the cumulated damage differs slightly between the selected sections of the fatigue test. From the results the effect of the excessively large stress peaks caused by True-

Load can be clearly seen since the True-Load results are significantly higher even though the general trend of the stress history is similar as can be seen in figure 27.

Table 2. Palmgren-Miner's sums based on hot spot method and design S-N curve.

	Beginning	Middle	End	Total [Sum]
LUT1 SG	0.013	0.013	0.018	0.043
LUT2 SG	0.071	0.065	0.067	0.203
LUT1 TL	-	-	-	0.927
LUT2 TL	-	-	-	1.204
LUT1 8-gauge	-	-	-	0.07
LUT2 8-gauge	-	-	-	0.139

Even though based on the results of the table 2 one could assume that the loading is similar in each of the compared cases figure 26 shows different view. It can be seen that the mean stress level changes considerably between the cases while the shape of the distribution remains quite constant and since the hot spot method does not consider mean stress or stress ratio the difference seen in figure 26 is not seen on the damage sum estimations. While conducting the analysis it was noticed that the mean stress level of LUT1 strain gauge changed considerably between various days with no apparent reason which can be seen also in figure 26 therefore the LUT1 strain gauge is ignored in further analysis.

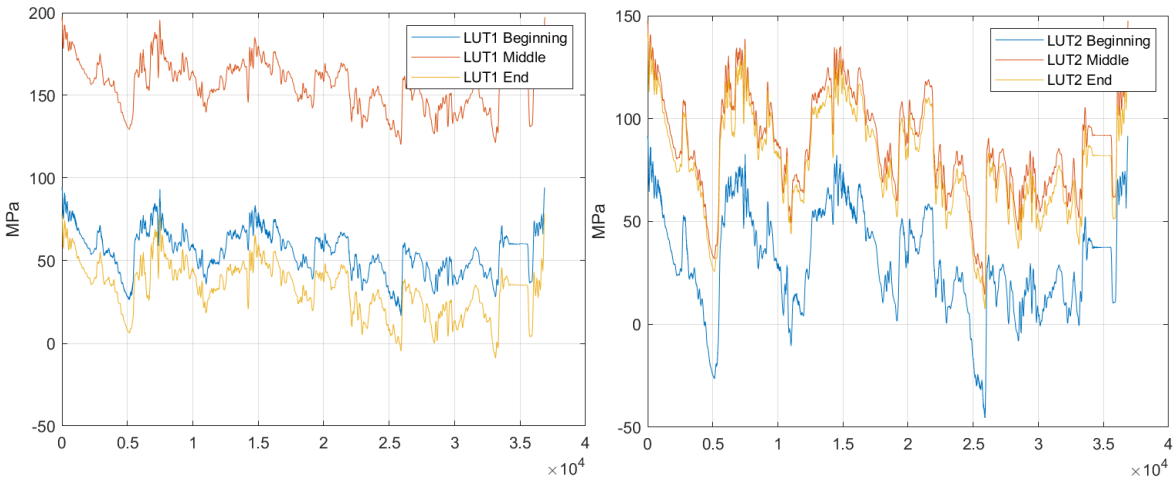

Figure 26. Hot spot strain gauge data.

Looking at the figure 27 similar spikes caused by the True-Load can be seen with hot spot method as in the case of nominal stress area (figure 23 at page 45). It can also be seen that the hot spot stress calculated based on True-Load seems to follow similar general trend as the measured values.

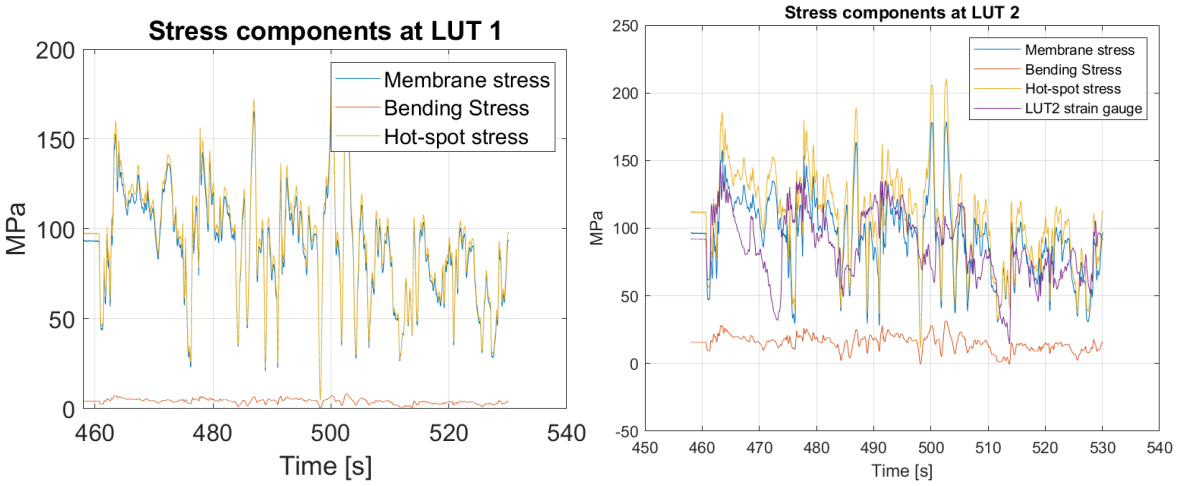

Figure 27. Stress components at the hot spot gauge locations in the middle of the test based on True-Load.

In figure 28 hot spot stress ranges are shown based on the hot spot strain gauge measurements and True-Load. It is clearly visible that the True-Load system causes significantly higher stress ranges than the hot spot strain gauge measurements would indicate. The True-Load system seems to overestimate or even generate some of the stress peaks which can clearly affect the fatigue life estimates as shown in table 2. From appendix IX it can be seen that the measured hot spot stress range distributions per test cycle are similar for each of the three data sets. Also, the LUT2 strain gauge location at the middle of the flange is clearly more severely loaded than LUT1. Appendix XI includes similar stress range distributions for both hot spot strain gauge locations but those are calculated based on the True-Load data. For both of those appendices the stress ranges are cut at 100 cycles to make the graphs more readable since the amount of very low stress ranges is high. By comparing the results in the appendix IX and appendix XI it can be seen that the True-Load results include significantly higher stress ranges as could be also seen in figures 27–28 and appendix II.

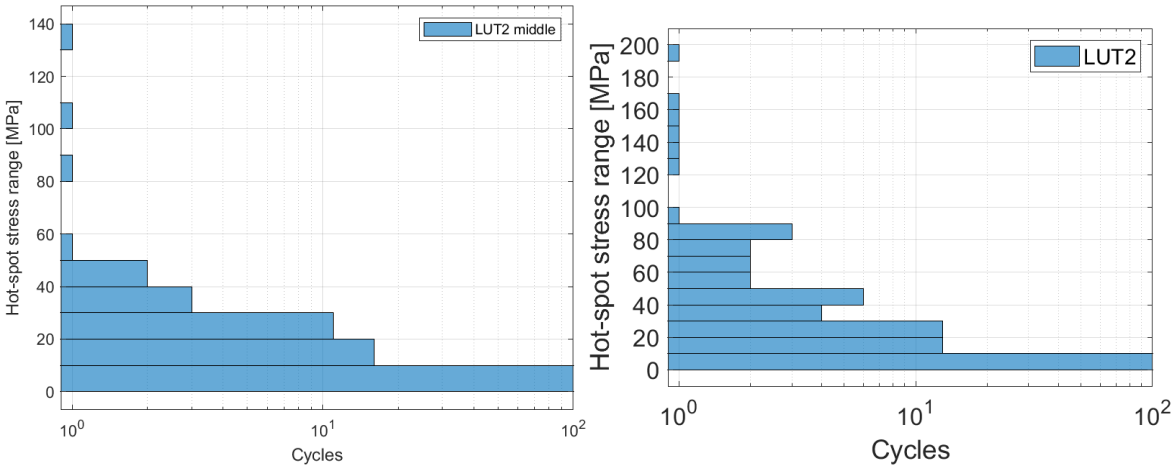

Figure 28. Hot spot stress range distributions based on strain gauge on left and based on True-Load on right.

Figure 29 shows the stress components calculated at the LUT2 strain gauge location based on the 8-strain gauge method. It can be seen that the calculated stresses correspond very well with the measured strain gauge data. Similarly, the stress range distribution between the measured data (appendix IX) and 8-strain gauge method (appendix X) seem to correspond much better than the in the case of True-Load.

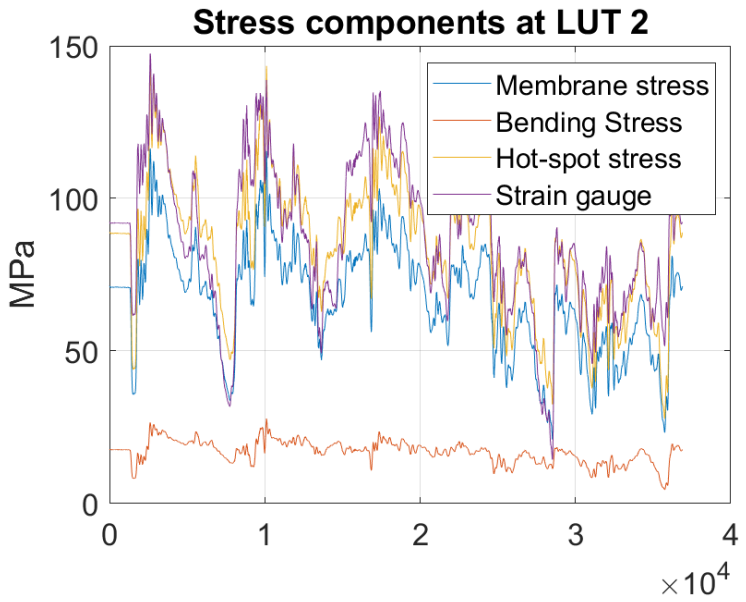

Figure 29. Stress components at the LUT2 location based on the 8-strain gauge method.

3.3.3 Results of effective notch stress method

The damage sum distributions based on True-Load for more critical weld toes of both welds are shown in figure 30. Again, it can be seen that the right side of the boom seems to have significantly larger damage sums. Also, now the effect of the cylinder force can be seen in the middle of the weld toe 4. Damage sum distributions for all toes based on design S-N curve are shown in appendix XV and for mean S-N curve in appendix XVI. The stress range distributions for the most loaded node of each weld toe can be seen in appendix XVII.

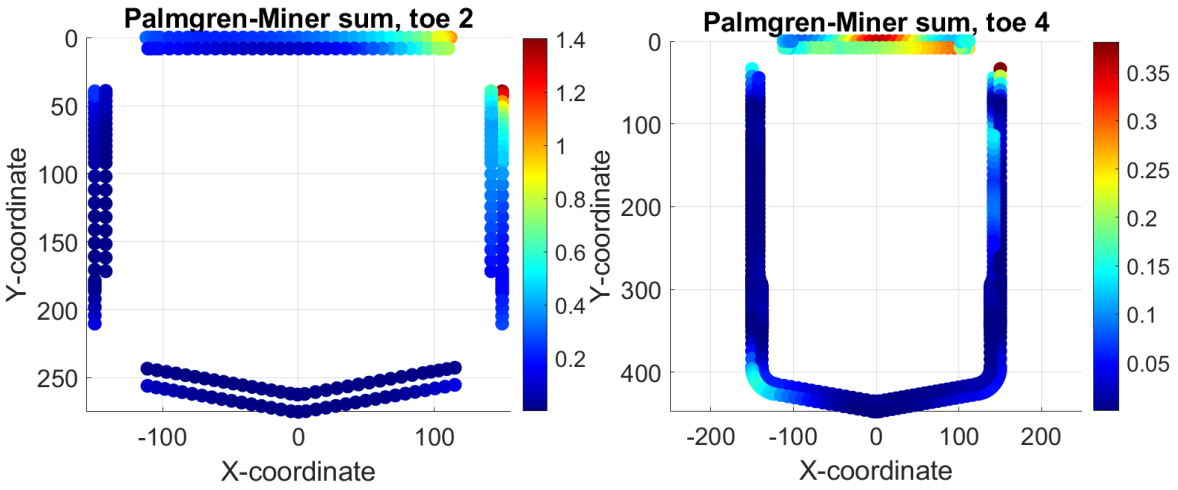

Figure 30. Damage sum distributions based on True-Load and mean S-N curve.

At the rear end casting the 8-strain gauge method lacks the effect of the hydraulic cylinder which the True-Load takes into account, and this is clearly visible in the calculation results included in figure 31. Therefor True-Load gives more information of the local phenomena whereas additional hot spot strain gauges would be required to see those local effects in combination with the 8-strain gauge method. Also looking at the results of the front end casting it can be seen that that damage sum values are very low. The damage sum distribution is quite different to the results based on True-Load. The stress range distributions can be seen in appendix XIV. Figure 31 shows the most critical weld toes for both welds while appendix XII and appendix XIII shows also the less critical toes. It seems that the measurements close to the rear end casting are not suitable to be used for the front end casting calculations. It might be possible to fix this issue by having another measurement plane close to the front end casting.

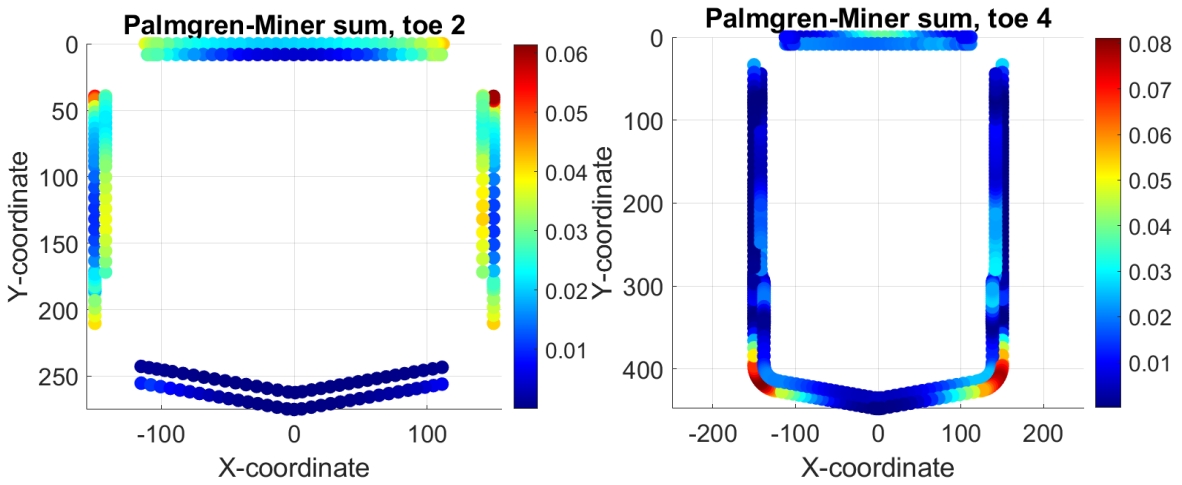

Figure 31. Damage sum distributions based on 8-strain gauge method and mean S-N curve.

3.3.4 Result of 4R method

4R calculations were performed only using the True-load method since as shown in the earlier chapters it was shown that the 8-strain gauge method does not give reliable results especially in the front end casting. Since the 4R method is significantly more time consuming to calculate than ENS method this also supported the decision not to calculate everything with 4R method. Figure 32 shows the damage sum distribution at the most critical weld toes based on ENS results. The damage sum for all the weld toes are shown in appendix XVIII.

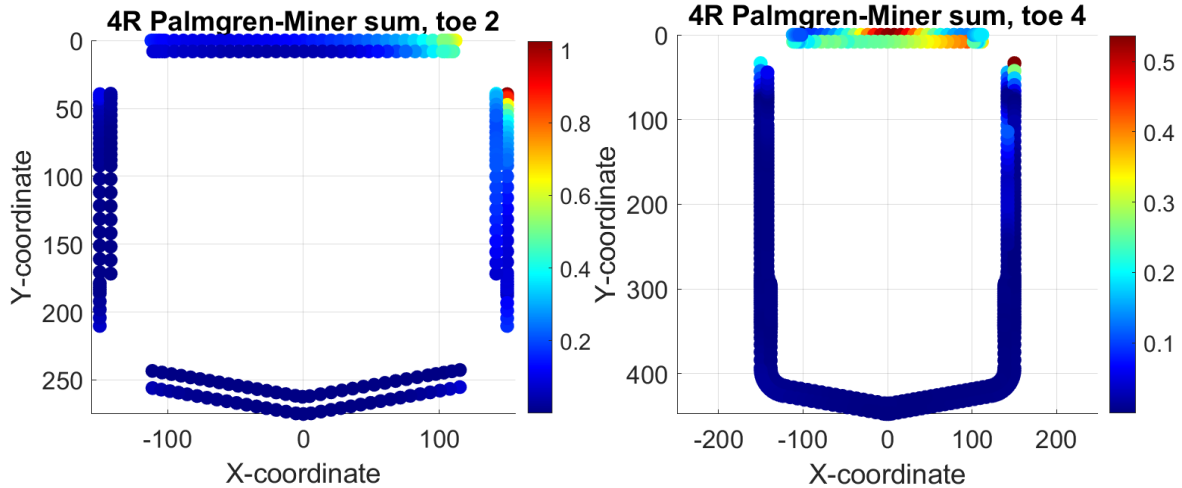

Figure 32. Damage sum distributions at the critical weld toes based on 4R method.

4 DISCUSSION

Various calculation methods used in this thesis are discussed in the chapters below. Simple sensitivity analysis for 4R method is also presented. For the 4R methods it was examined how different material, residual stresses or mean ENS stress levels would affect the result even if the ENS method would give same exact answer for each of the cases.

4.1 Comparison between the True-Load and 8-strain gauge methods

It has been mentioned multiple times before that the True-Load method seems to overestimate some of the stress peaks and therefor cause higher stress ranges in the fatigue analysis. Since this leads into errors in the highest stress ranges it can have significant effect on the fatigue analysis results. Also, the advantage of using True-Load is that it can take into account the forces due to the hydraulic cylinder above the lifting boom.

Based on the strain gauge data the 8-strain gauge method gave similar results as the hot spot strain gauges and the normal and shear stresses at the LUT strain gauges corresponded very well with the calculated values. But it is clearly visible from the results that the 8-strain gauge method does not give acceptable results at the front end casting. This is probably due to the fact that that calculation method is calibrated based on strain gauges close to the rear end casting and therefore the method's accuracy is not good enough to describe the stress state in the opposite end of the beam. Close to the rear end casting the results of 8-strain gauge method seemed significantly better than the results of True-Load based on the hot spot and nominal LUT strain gauges. It would be interesting to see how the results would change if the strain gauges would have been attached close to the front end casting instead of the rear end casting.

Based on the results it could be concluded that it seems that the 8-strain gauge method is not able the describe the stress state of whole lifting boom with good accuracy. Close to the LUT-plane the 8-strain gauge method seems to be able to describe the stress state of the beam well but at the further end of the beam the accuracy seems to suffer. This could be solved by having another measurement plane close to the front end casting or with additional

hot spot strain gauges. True-Load on the other hand seems to work relatively well. Both of the systems have their own flaws and limitations.

4.2 Comparison between the fatigue assessment methods

To compare both the fatigue assessment methods and the strain gauging methods figure 33 was combined. In the figure 33, the damage sums based on hot spot gauges, True-Load and 8-strain gauge method are compared at the hot spot strain gauge locations. Notch stress methods include damage sum for both of the weld toes. From the figure it is clearly visible that the True-Load causes much higher damage sums than would be assumed based on strain gauges or the 8-strain gauge method. The 8-strain gauge method seems to correspond relatively well with the hot spot strain gauge results. It seems that 4R method gives similar damage sums as ENS method. Hot spot method seems to give higher damages sums than 4R and ENS methods at the same weld toe. However, no other striking trends between the fatigue assessment methods are visible.

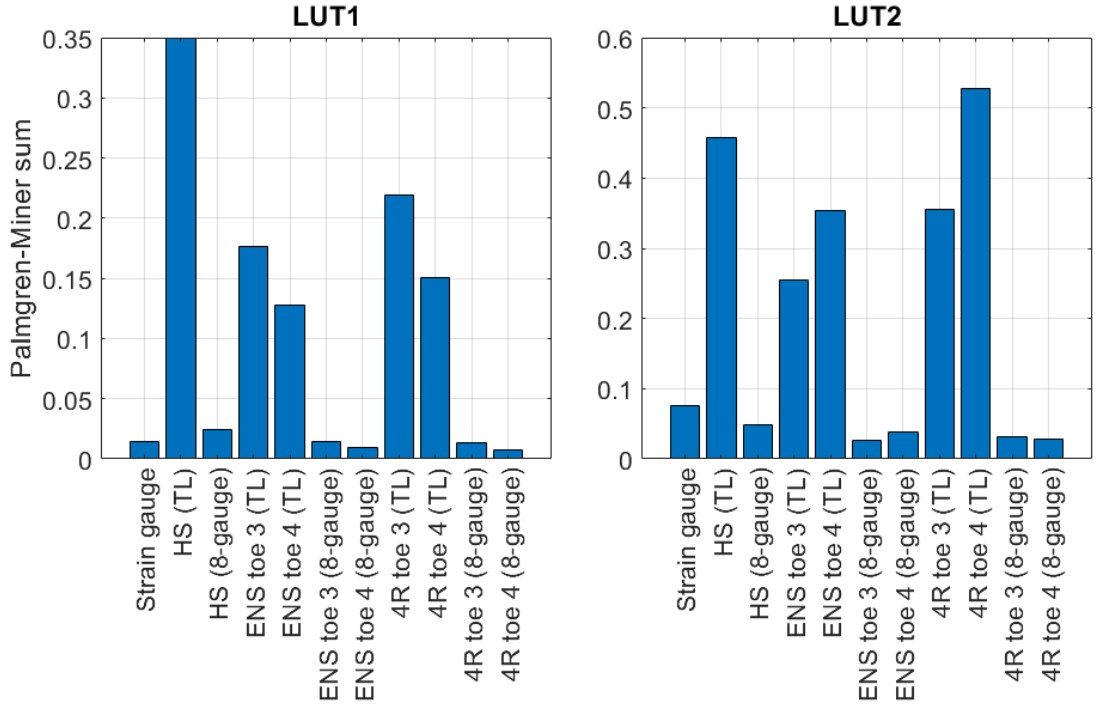

Figure 33. Damage sums based on various methods and mean S-N curve.

Large advantage of the ENS method is that the calculations can be made in closed form which makes the calculation procedure effective while this is not possible for the 4R method and the calculation takes much longer.

Figure 34 shows clearly how the stress history based on True-Load differs from the other methods and the effect of that can be seen on the results of figure 33. Similar behavior can also be seen for example in appendix II.

Clear difference in the 4R and ENS results can be seen in the bottom flange of the rear end castings weld since ENS method does not differentiate between compressive and tensile stress cycles but 4R method takes that into account.

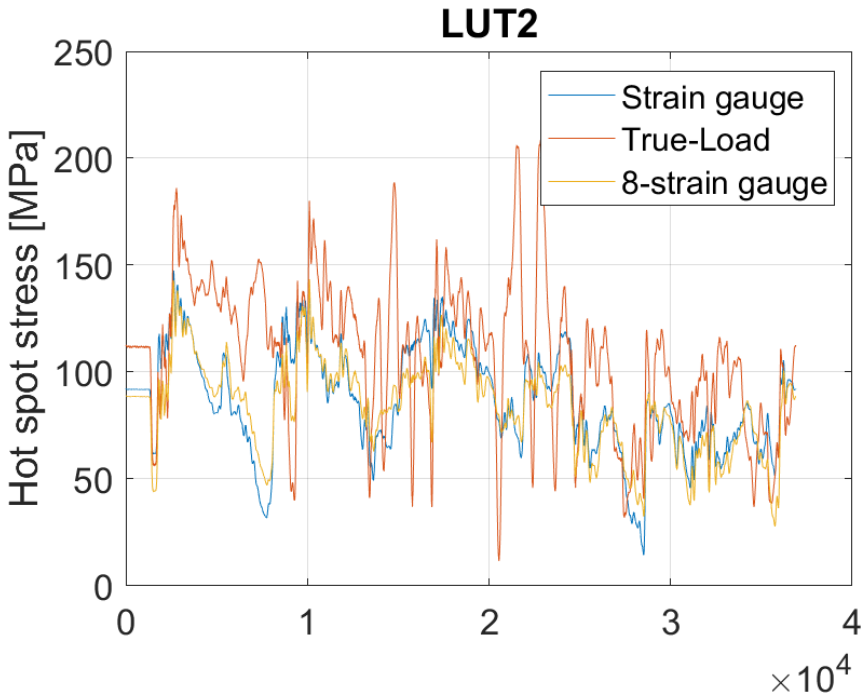

Figure 34. Comparison of the hot spot stress history based on different evaluation methods.

4.3 Sensitivity analysis for 4R

Effect of the 4R parameters were studied by using 3 variable amplitude loadings with different mean stress levels. As the basis for the comparison loading for a single node was selected. This loading has low absolute mean stress value. To see the effect of the mean stress two comparison curves were made by either adding or subtracting 300 MPa for each of the stress values of the stress history. That way all these curves would give same exact results with ENS method. These loading histories can be seen in the bottom of figure 35. For the material comparison worst measured residual stress equal to 281 MPa was assumed. It can be seen that residual stresses can have huge effect on the damage sum and fatigue life.

Also, it is clearly seen that materials with higher yield or ultimate strength led to worse fatigue life and tensile mean stress has more significant effect on the high strength steels.

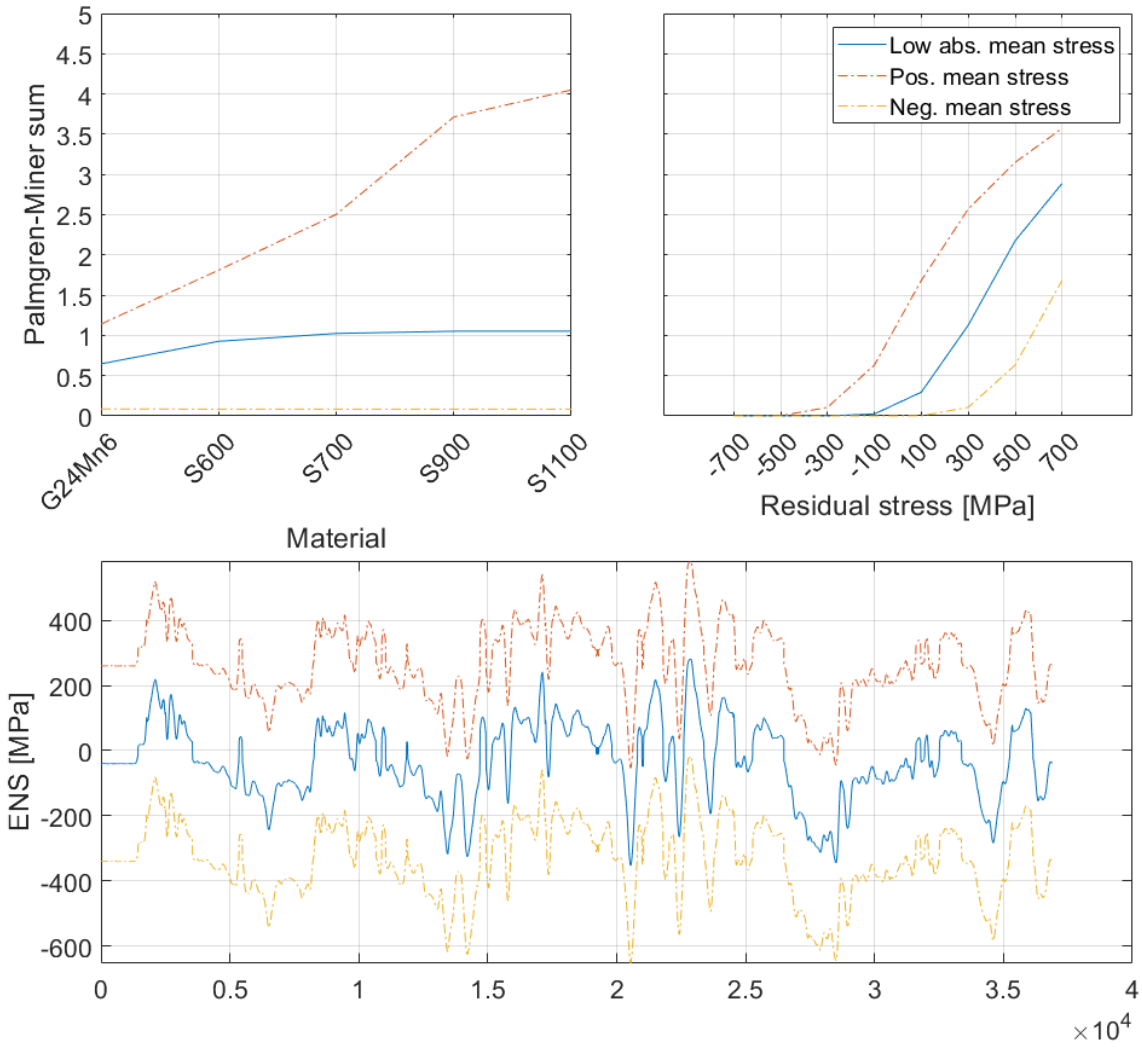

Figure 35. Effect of different parameters on 4R results.

For both figure 35 and 36 same three load cases are used. From figure 36 it can be clearly seen that the effect of tensile residual stress is more severe for higher strength steels. Based on this using high strength steels in as welded state gives no advantage in the fatigue life and to even achieve similar fatigue life than lower strength grades low or compressive residual stresses are needed. For all of the cases of the figures 35–36 ENS method would give same exact Palmgren-Miner's sum since it does not consider mean stress, material or residual stresses but the results of 4R method highly differ between the load and material cases.

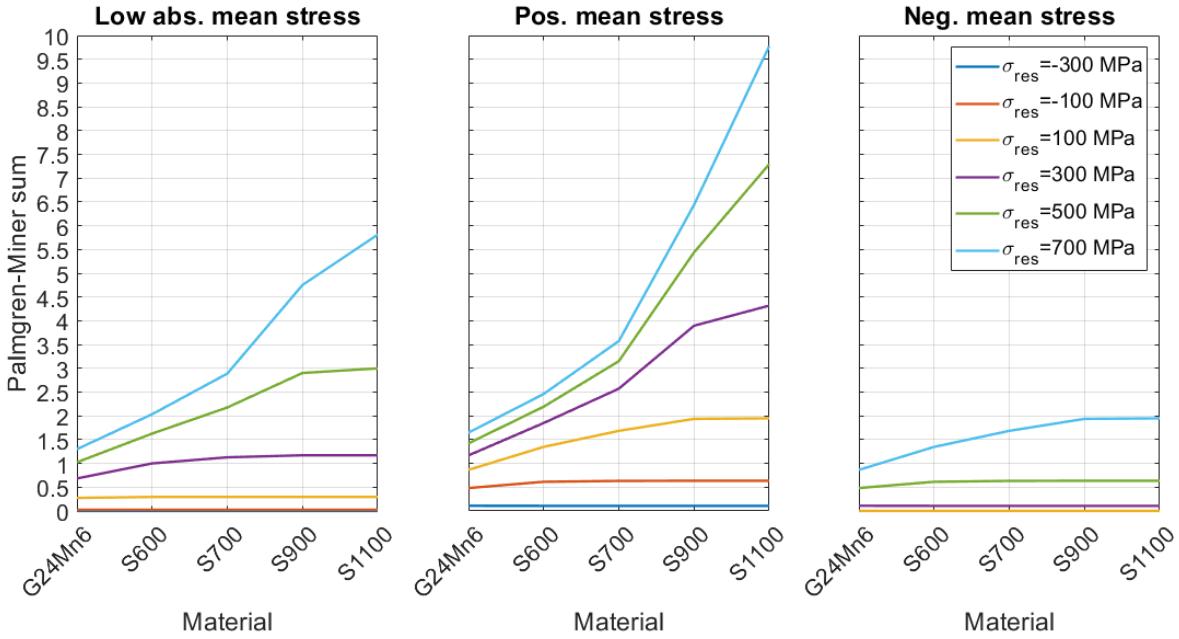

Figure 36. Effect of residual stress.

Based on Nykänen et al. (2017, p. 183) lowest residual stress values after high frequency mechanical impact (HFMI) treatment can be assumed as -0.255Rm. For the materials considered in figure 36 that would mean that the residual stresses after HFMI treatment could be assumed to be -150 to -280 MPa in compression depending on the material. By looking at the graphs of figure 36 there is not significant differences in the damage sums caused by the material change at such residual stress levels. Also, the damage sums are very low for each of the load and material cases considered. Consequently, peening processes like HFMI treatment can be very effective way for achieving good fatigue strength for welded high strength steels.

5 CONCLUSION

Fatigue analysis of the lifting boom was successfully conducted. In the process finite element model for notch stress analysis was constructed. Also fatigue calculations were conducted in such way that the same calculation sheets could be used for various weld joints just by changing the input data from True-Load and FE-model.

It was shown that the True-Load software gives reasonable results for the fatigue damage although it clearly overestimated the effect of some of stress peaks which led into larger stress ranges than measured data would suggest. Reason why the True-Load overestimates some stress peaks would be an interesting topic for further research. There was some offset between measured stresses and ones calculated using True-Load but that might have been caused by zeroing of the strain gauges.

The 8-strain gauge method showed great correspondence with measured results close to the LUT plane but when moved away from that the accuracy of the results dropped and especially at the front end of the beam results were not acceptable. Also, this method could not take into account the effect of the hydraulic cylinder on top of the beam although this did not seem to cause much error based on comparison of hot spot strain gauge and calculation results shown in figure 29 at page 51. And these local effects can be taken into account with separate hot spot strain gauges.

Results of the 8-strain gauge method showed that it gives accurate results close to the LUT-plane but not further away from it. Addition of another measurement plane close to the front end casting might give accurate results for the front end of the boom. Also, the fatigue assessment can be done based on hot spot strain gauges attached to critical locations and using the 8-strain gauge method just for determining the forces affecting the boom. Stress ranges for the fatigue calculations using 4R, ENS and nominal stress methods were based on the principal stress with highest absolute value and this assumption gave reasonable results with all of those methods.

The fatigue failure occurred at the at the opposite corner of the estimation of calculation results. This might be partly due to the fact that the data used for calculations was so short and might have not described the whole fatigue test well. It was unfortunate that more comprehensive strain gauge data was not available. Maximum damage sum at the failed corner was 0.28 based on True-Load and mean S-N curve that is between the values given in design codes 0.2 or 0.5. So, it could be seen that even the failed corner seemed to have similar fatigue resistance as design codes would assume. The opposite corner however seemed to have much better fatigue resistance than assumed by design codes. This difference might have become more moderate if more input data would have been available. It was known that the asymmetry of the loading changes during the fatigue testing, but it was not possible to account for that due to the lack of strain gauge data.

Based on the calculation results it seemed that the 4R method gives similar damage sum values as ENS. The hot spot method seems to give larger damage sums than 4R and ENS methods. Also, as it was shown in figure 36 (page 58) the effect of assumed residual stress can have significant effect on the 4R results. The results of 4R method and ENS method can be highly different depending on the mean stress level, residuals stresses and material.

It was also noted that the residual stresses can be very local. Residual stresses at P1_5 and P1_10 were -21 MPa and -296 MPa (appendix I) respectively so the difference is about 275 MPa even though the distance of the measuring locations is only about 13 mm (figure 3 at page 15).

The distribution and magnitude of the bimoment and its effect on the fatigue of the welds was not investigated in detail during this work and remains as a topic for further research.

LIST OF REFERENCES

Ahola, A., Muikku, A., Braun, M. & Björk, T. 2021. Fatigue strength assessment of ground fillet-welded joints using 4R method. International Journal of Fatigue, 142. Pp. 1–12.

Amraei, M., Zhao, X., Björk, T. & Heidarpour, A. 2020. Bond characteristics between high/ultra-high strength steel and ultra-high modulus CFRP laminates. Engineering structures, 205. Pp. 1–12.

Baumgartner, J. & Bruder T. 2012. An efficient meshing approach for the calculation of notch stresses. Welding in the World, 57. Pp. 137–145.

Hobbacher, A., F. 2016. Recommendations for Fatigue Design of Welded Joints and Components. Second edition. Springer International Publishing. 143 p.

Mettänen, H., Nykänen, T., Skriko, T., Ahola, A. & Björk, T. 2020. Fatigue strength assessment of TIG-dressed ultra-high-strength steel fillet weld joints using the 4R method. International Journal of Fatigue, 139. Pp. 1–14.

Niemi, E., Fricke, W. & Maddox, S. 2018. Structural Hot-Spot Stress Approach to Fatigue Analysis of Welded Components. Designer's guide. Second edition. Springer Singapore. 76 p.

Nykänen, T. & Björk, T. 2015. Assessment of fatigue strength of steel butt welded joints in as-welded condition - Alternative approaches for curve fitting and mean stress effect analysis. Marine Structures, 44. Pp. 288–310.

Nykänen, T., & Björk, T. 2016. A new proposal for assessment of the fatigue strength of steel butt welded joints improved by peening (HFMI) under constant amplitude tensile loading. Fatigue and Fracture of Engineering Materials and Structures, 39. Pp. 566–582.

Nykänen, T., Mettänen, H., Björk, T. & Ahola, A. 2017. Fatigue assessment of welded joints under variable amplitude loading using novel notch stress approach. International Journal of Fatigue, 101. Pp. 177–191.

Radaj, D., Sonsino, C., M. & Fricke, W. 2006. Fatigue assessment of welded joints by local approaches. Second edition. Cambridge: Woodhead Publishing Limited. 660 p.

SFS-EN 10293. 2015. STEEL CASTINGS. STEEL CASTINGS FOR GENERAL ENGINEERING USES. Helsinki: Suomen Standardisoimisliitto SFS ry. 21 p.

SFS-EN 1993-1-9. 2005. Eurocode 3: Design of steel structures. Part 1-9: Fatigue. Helsinki: Suomen Standardisoimisliitto SFS ry. 38 p.

SSAB. 2017. Strenx 700MC Plus. [www- data sheet]. [Referred 21.5.2021]. Available: https://www.ssab.com/products/brands/strenx/products/strenx-700-mc-plus

Young, W. & Budynas, R. 2002. Roark’s Formulas for Stress and Strain. Seventh edition. McGraw-Hill. 854 p.

APPENDIX I

Residual stresses at weld toes.

Location	New boom	New boom after fatigue	Old boom
P1_1	-327	-	-266
P1_2	-53	-	-123
P1_3	-310	-270	-253
P1_4	-313	-367.8	-233
P1_5	-65	-20.7	166
P1_6	-307	-170.4	-308
P1_7	-	-304.5	-
P1_8	-	-383.8	-
P1_9	-	-165.6	-
P1_10	-	-295.5	-
P2_1	6	50.4	141
P2_2	-80	-42	46
P3_1	-303	-277.4	-295
P3_2	-279	-193.1	-88
P4_1	-348	-230	-370
P4_2	-331	-295.3	-272
P5_1	-226	-237.1	-
P5_2	-124	-135.4	-
P6_1	19	-55.1	-
P6_2	70	-127.7	-
P7_1	-	267.9	-
P7_2	-	-243.3	-

Comparison of strain gauge values with stresses calculated based on 8 strain gauges and True-Load.

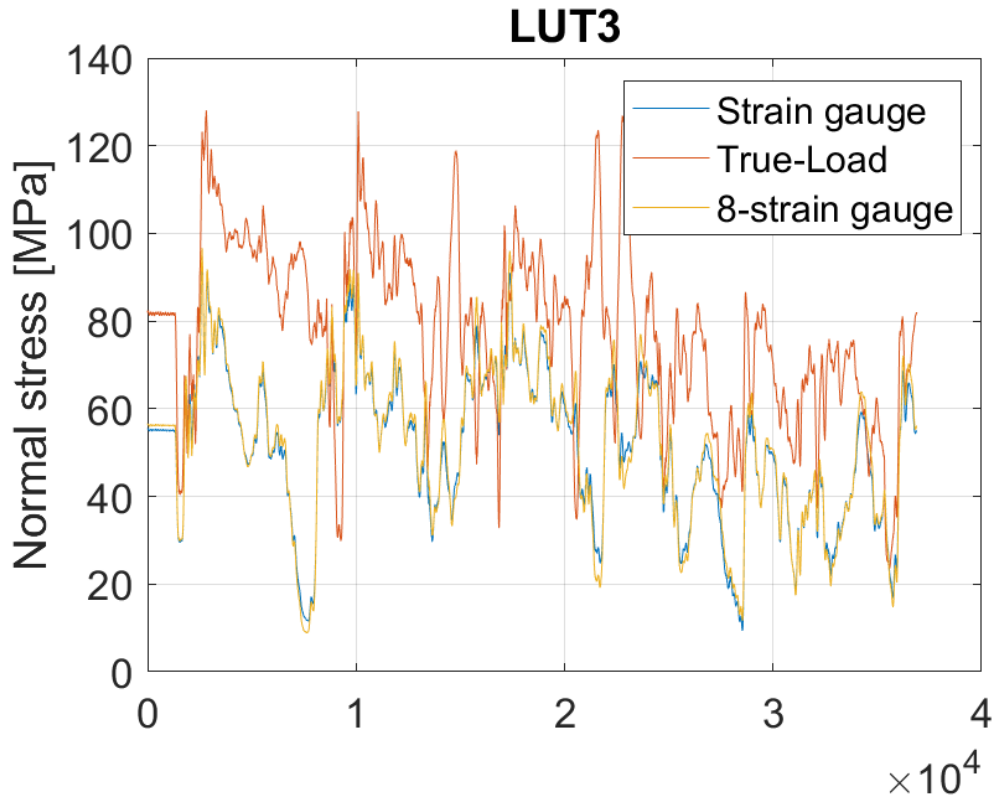

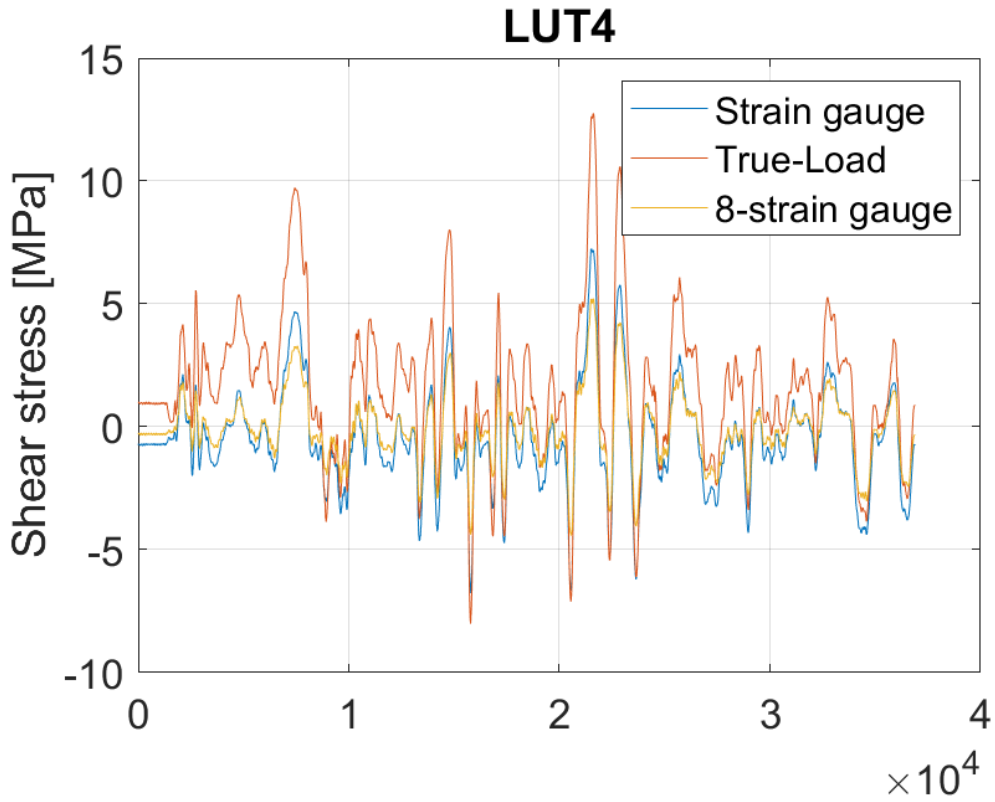

Comparison of strain gauge values with stresses calculated based on 8 strain gauges and True-Load.

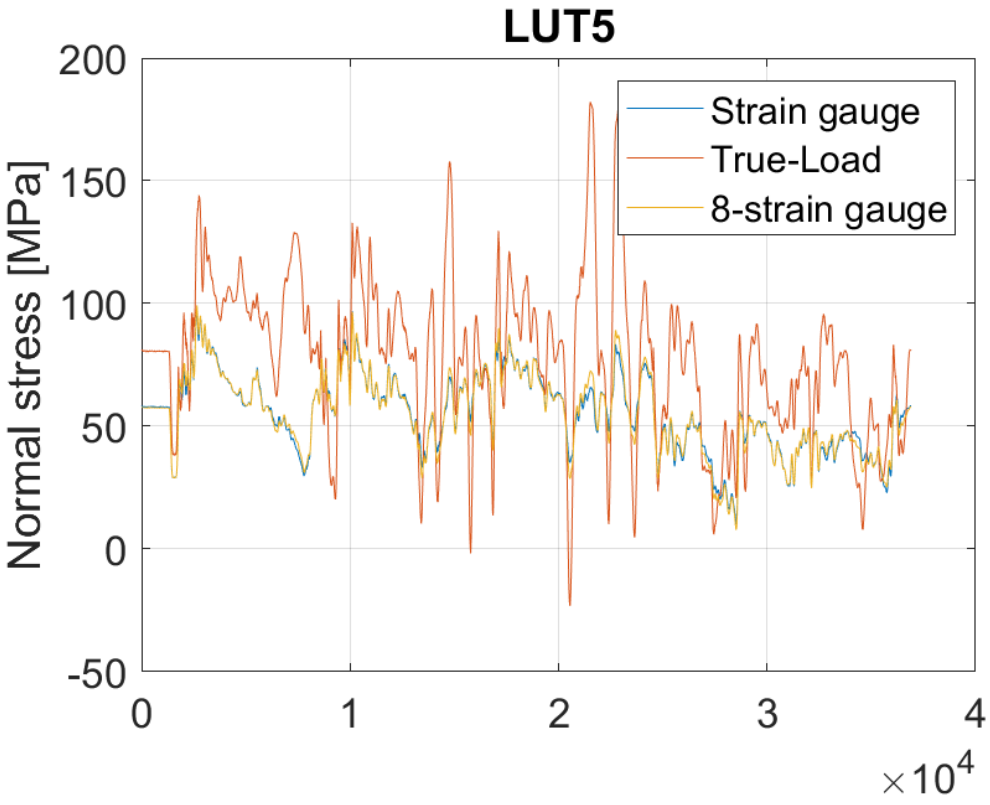

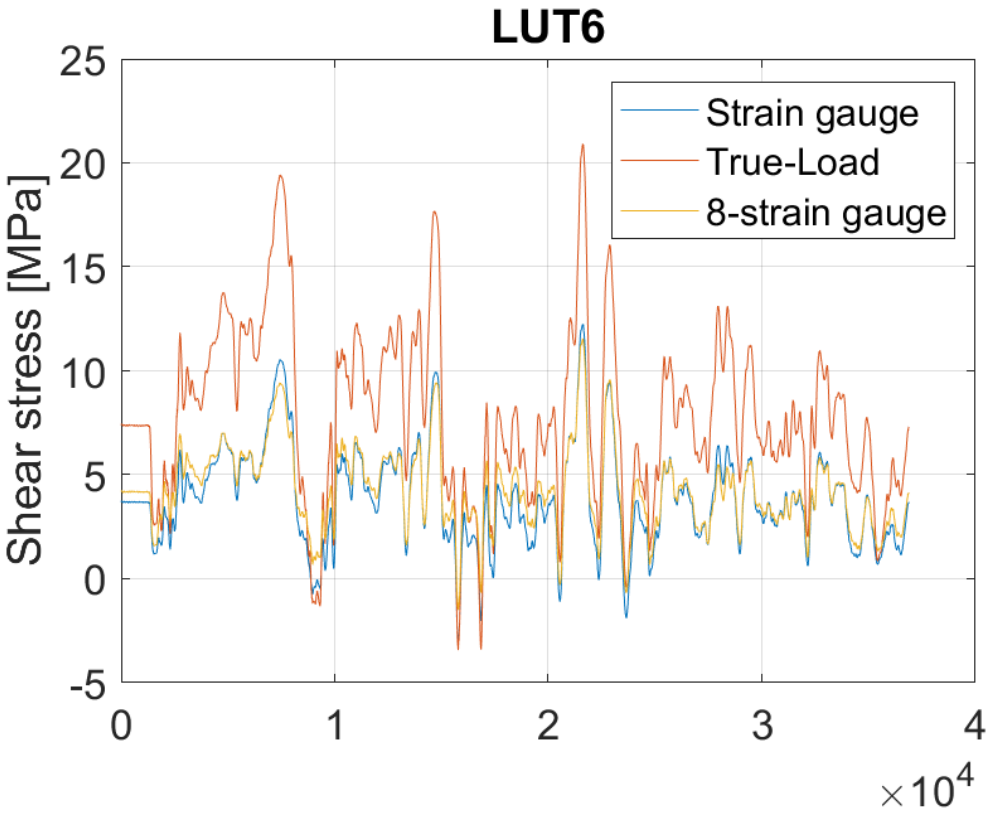

Comparison of strain gauge values with stresses calculated based on 8 strain gauges and True-Load.

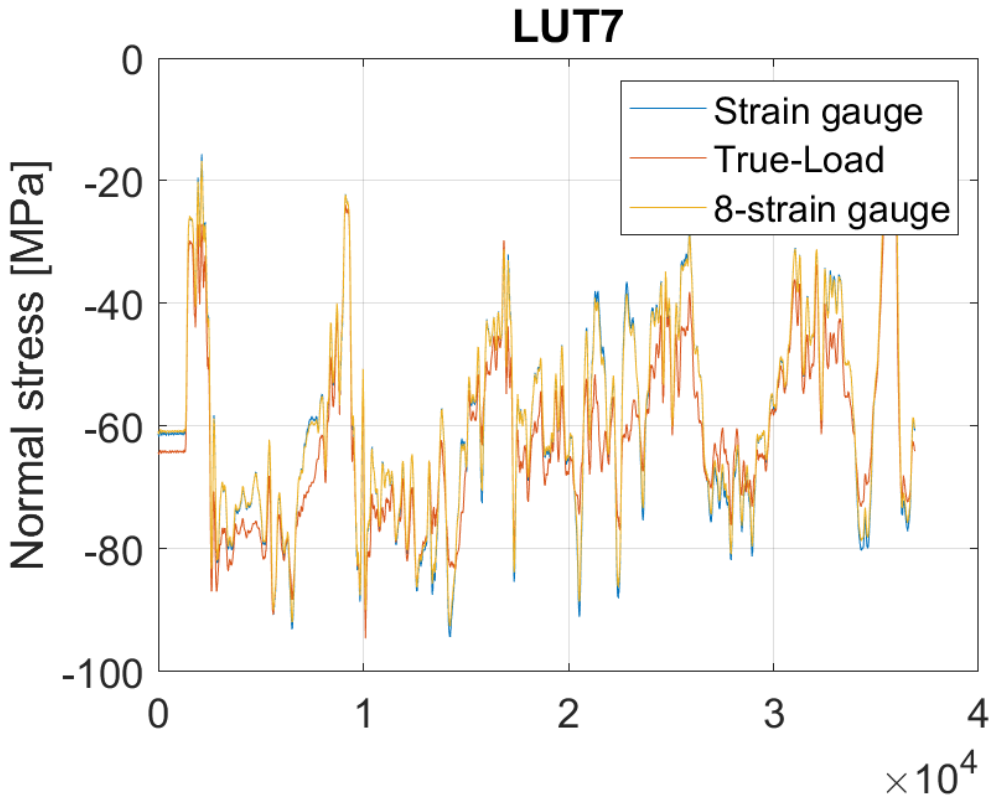

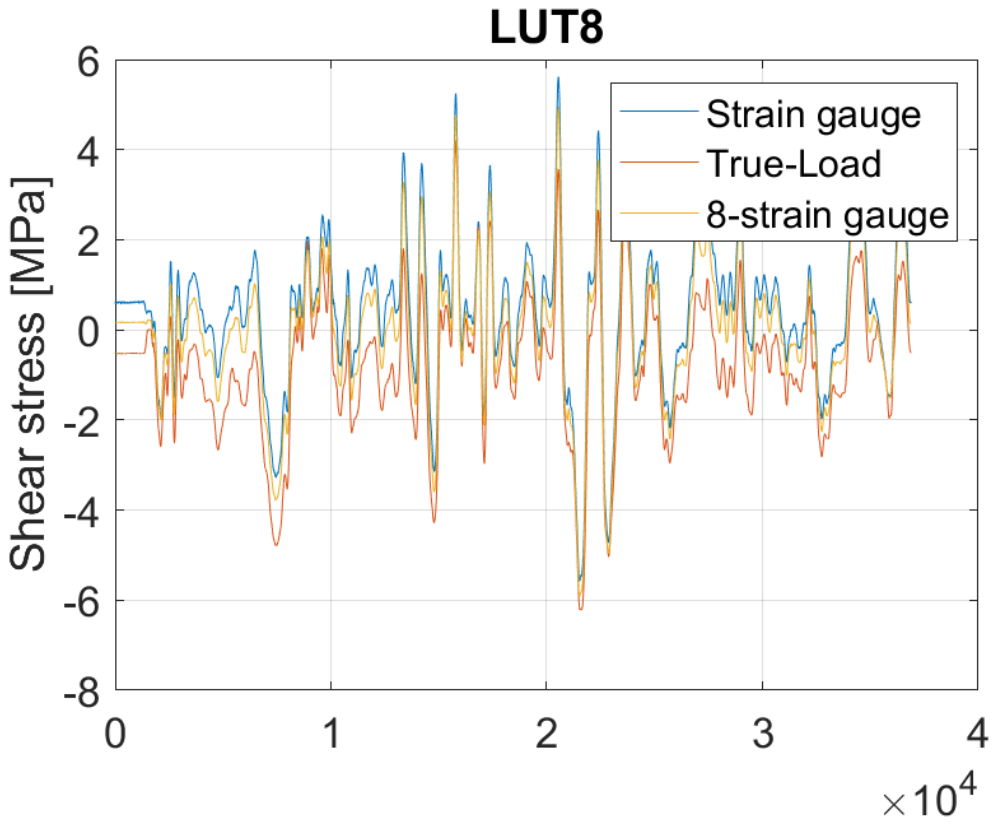

Comparison of strain gauge values with stresses calculated based on 8 strain gauges and True-Load.

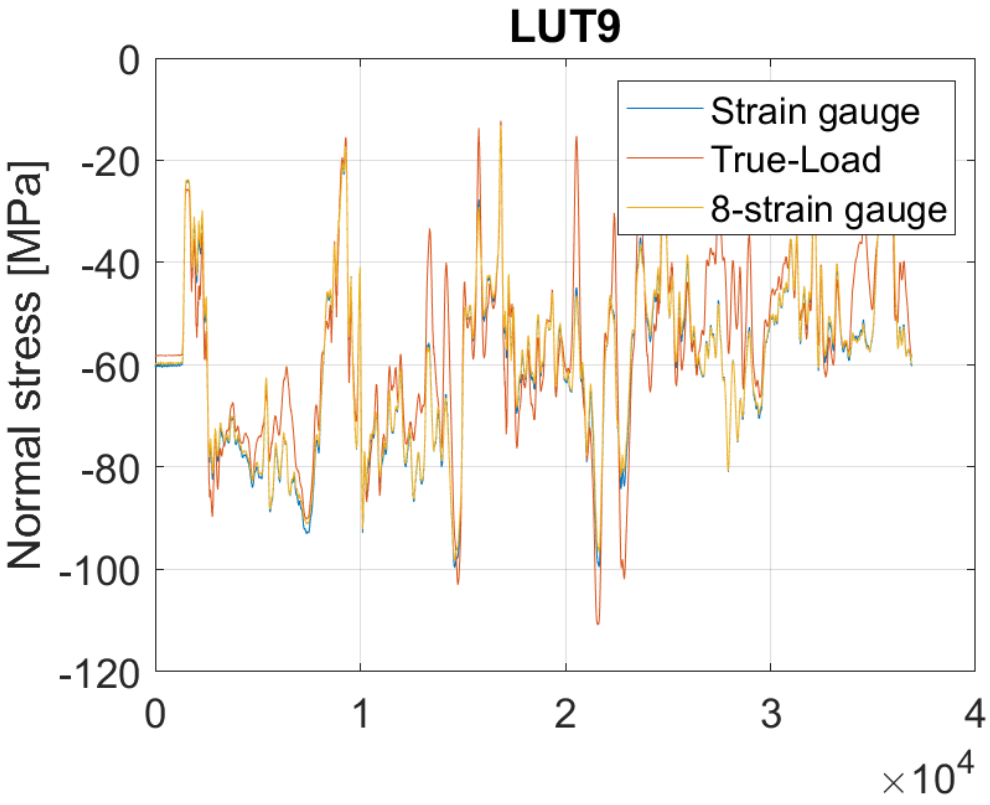

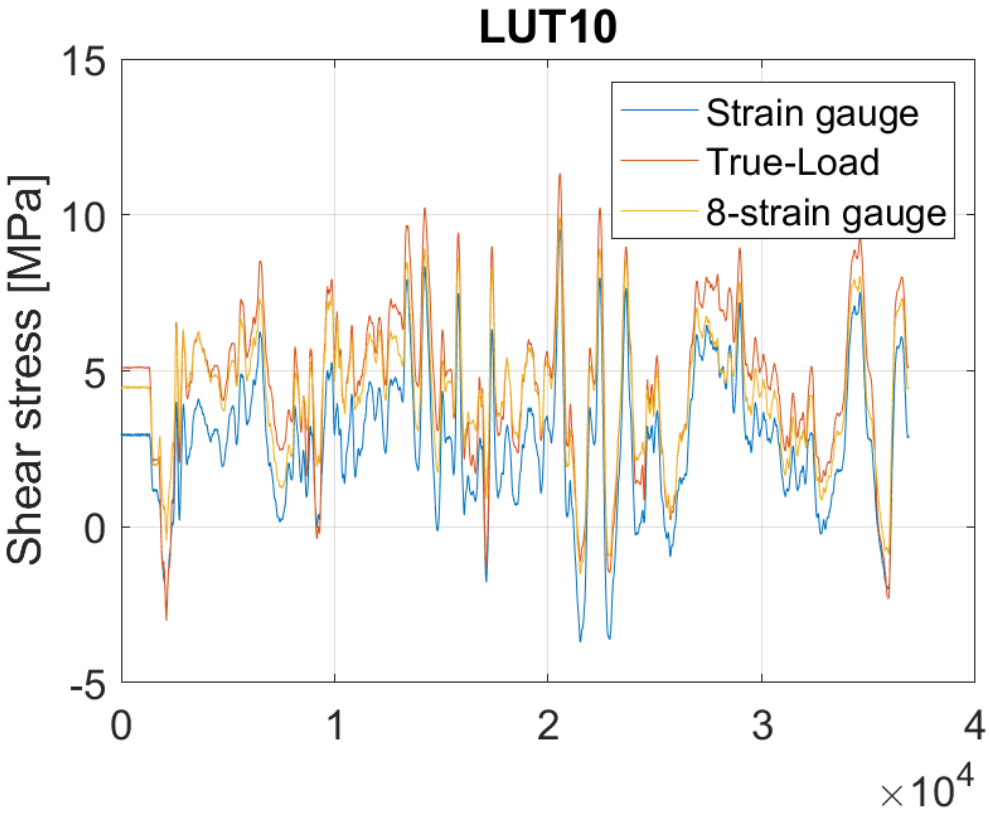

APPENDIX III

Palmgren-Miner's sum based on 8 strain gauges, nominal stress method and design S-N curve.

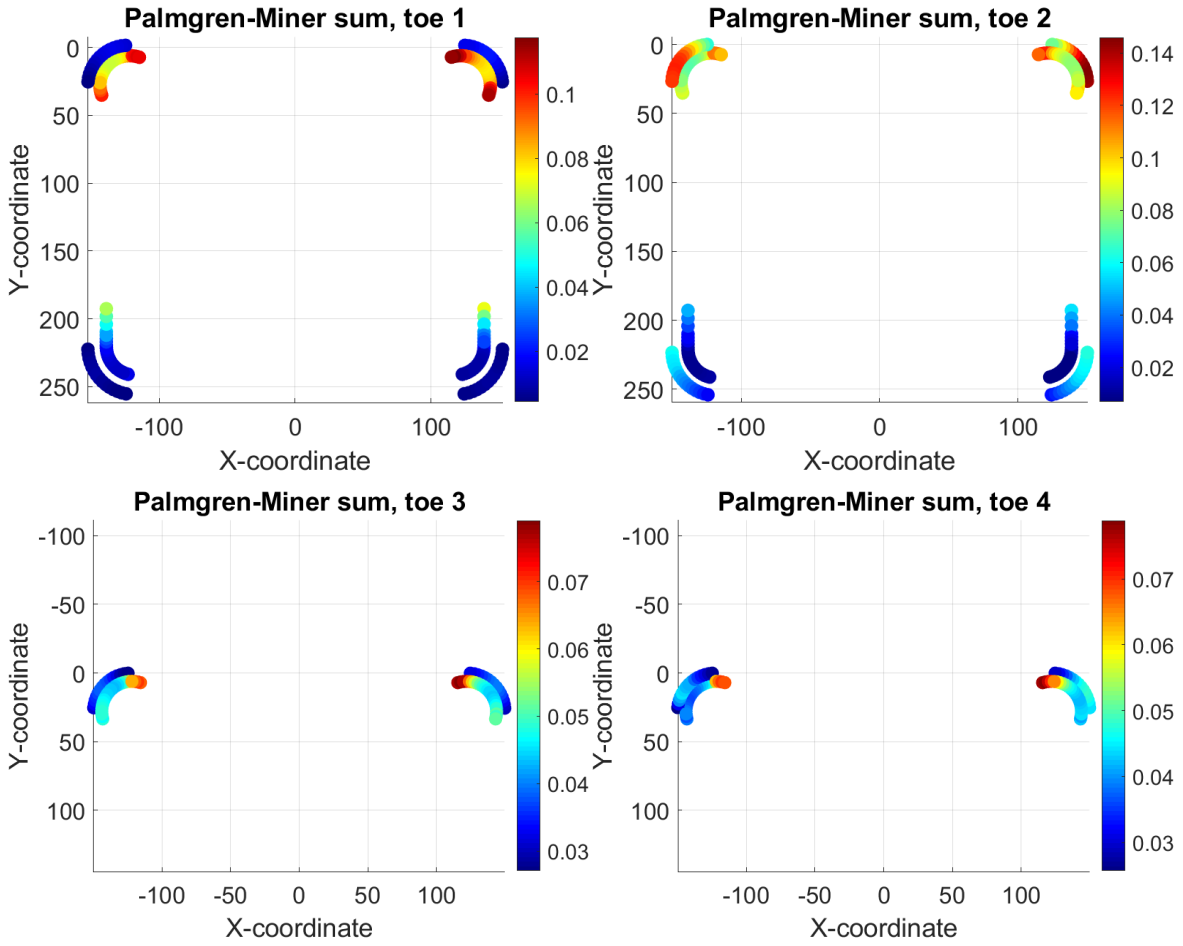

Palmgren-Miner's sum based on 8 strain gauges, nominal stress method and mean S-N curve.

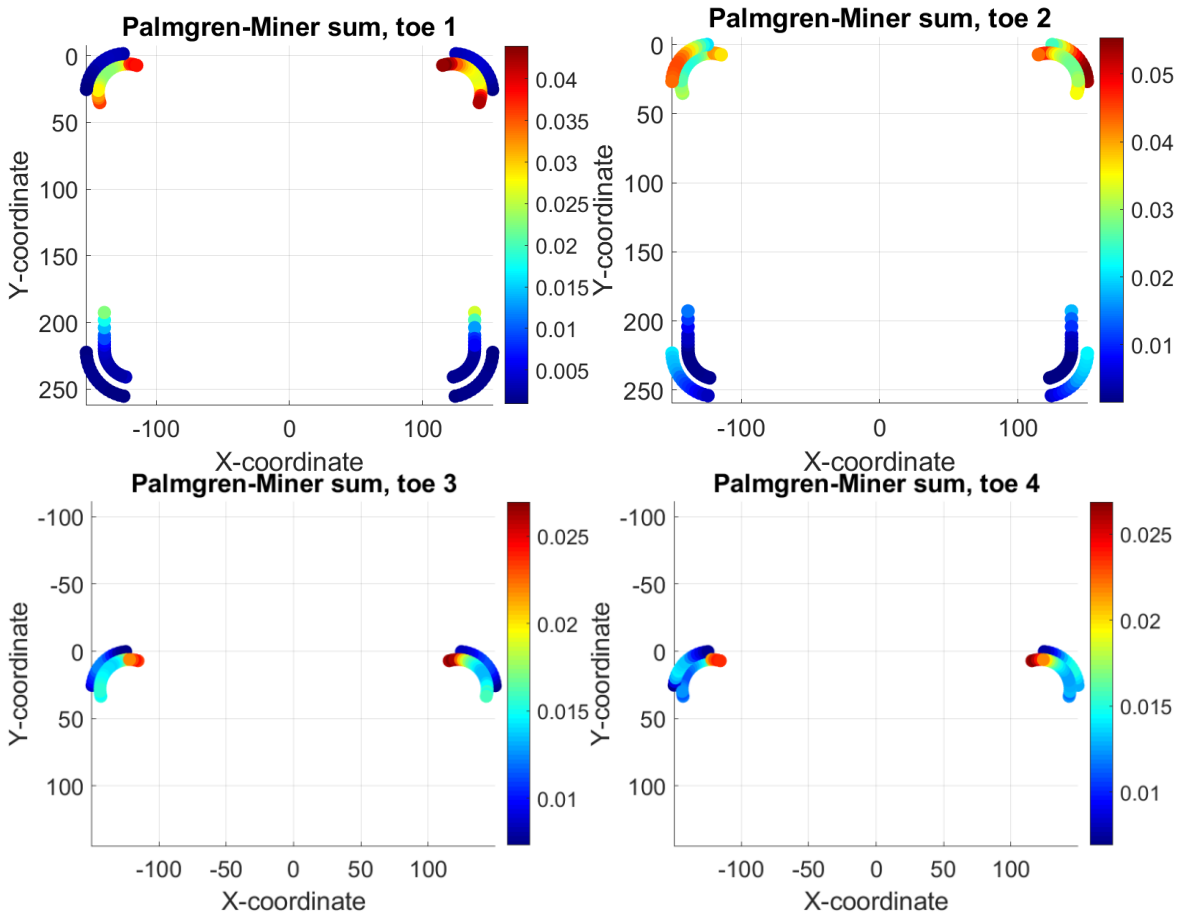

APPENDIX V

Nominal stress range distributions of the most loaded node of each toe based on 8 strain gauge method.

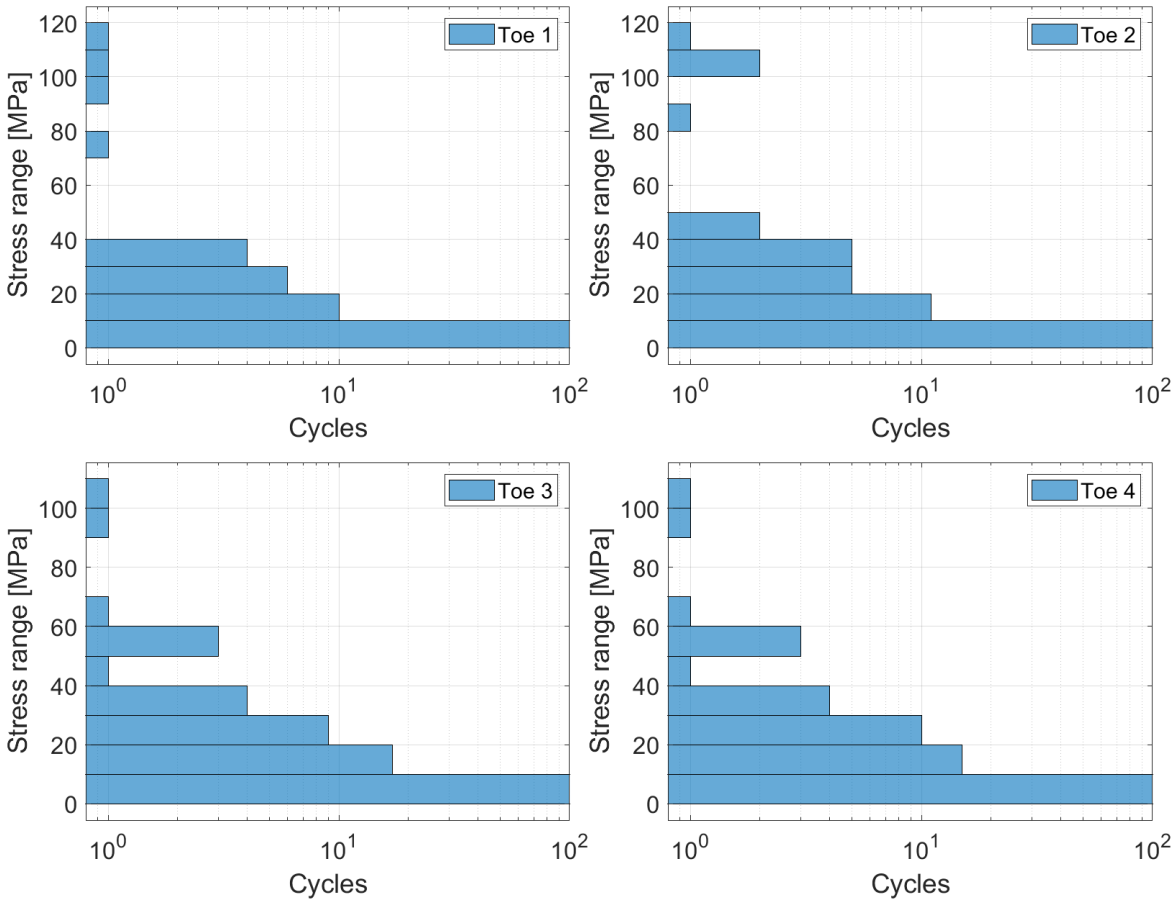

APPENDIX VI

Palmgren-Miner's damage sum distributions based on nominal stress method, design S-N curve and True-Load.

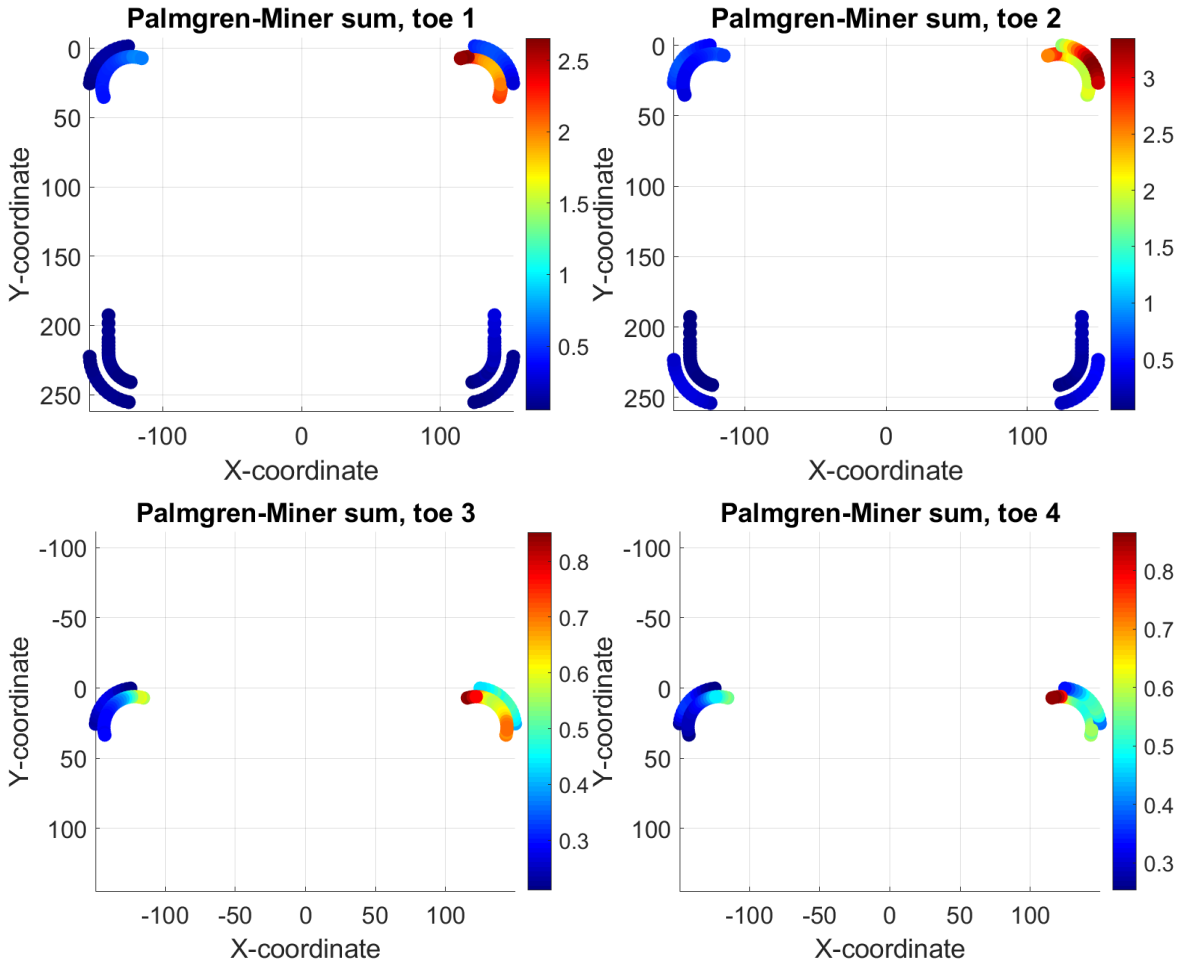

APPENDIX VII

Palmgren-Miner's damage sum distributions based on nominal stress method, mean S-N curve and True-Load.

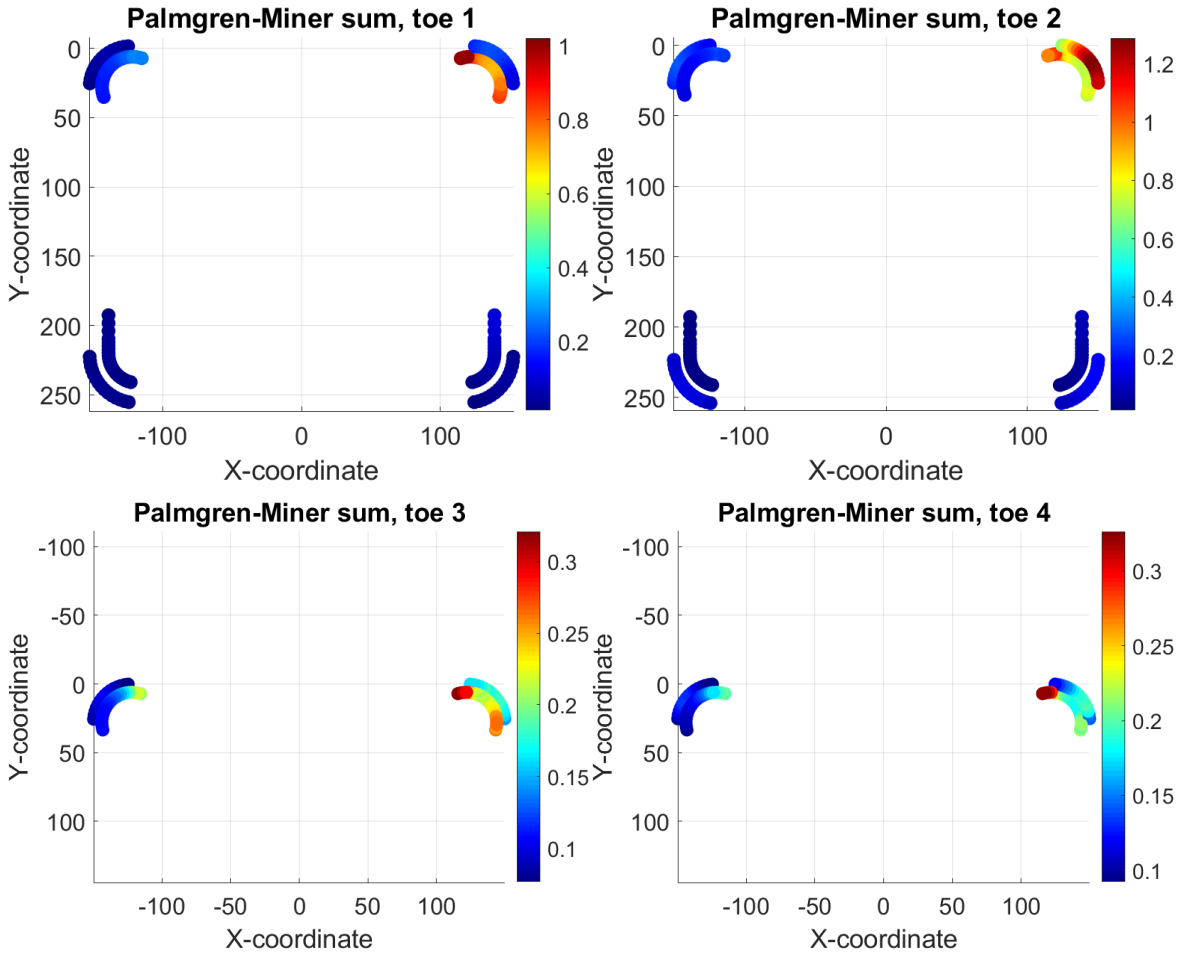

APPENDIX VIII

Nominal stress range distributions of the most loaded node of each toe based on True-Load.

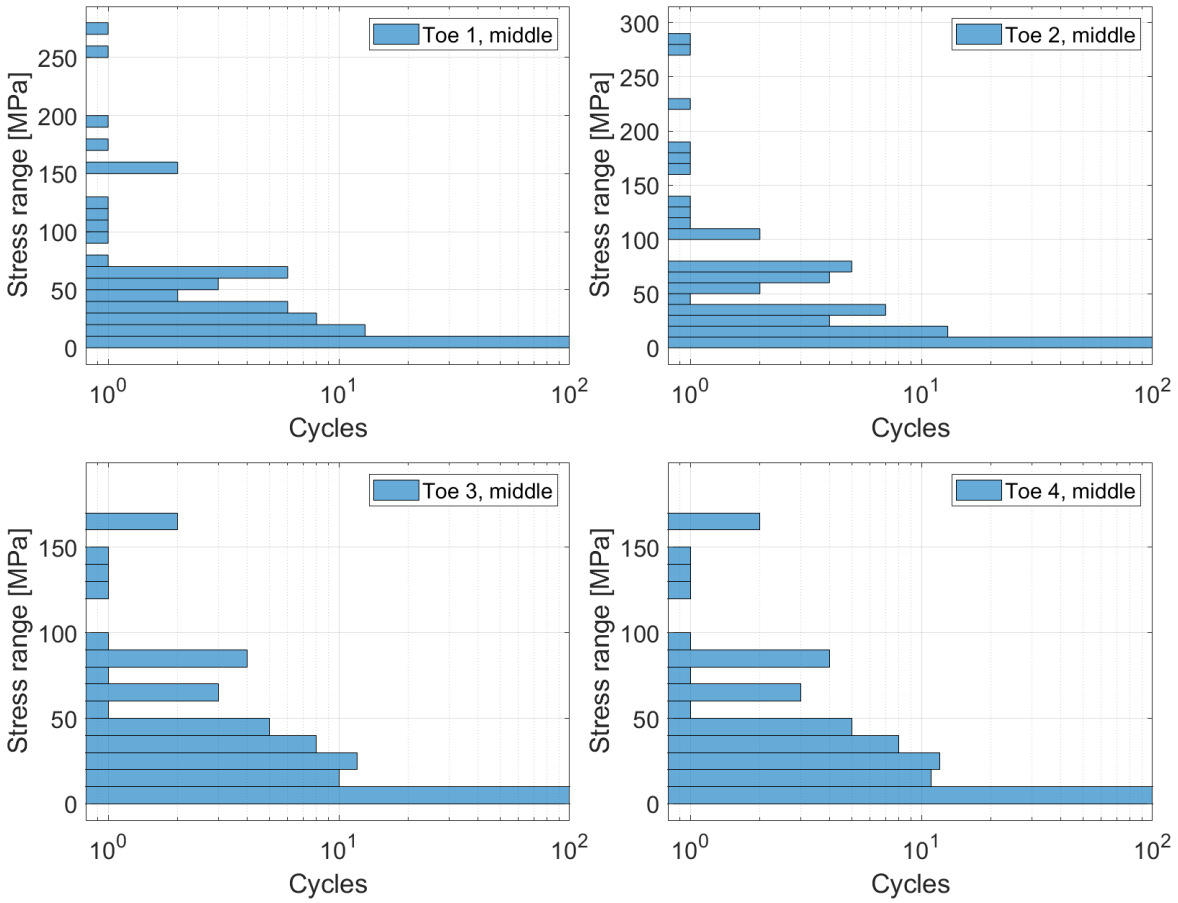

APPENDIX IX

Hot spot stress range distributions based on strain gauges.

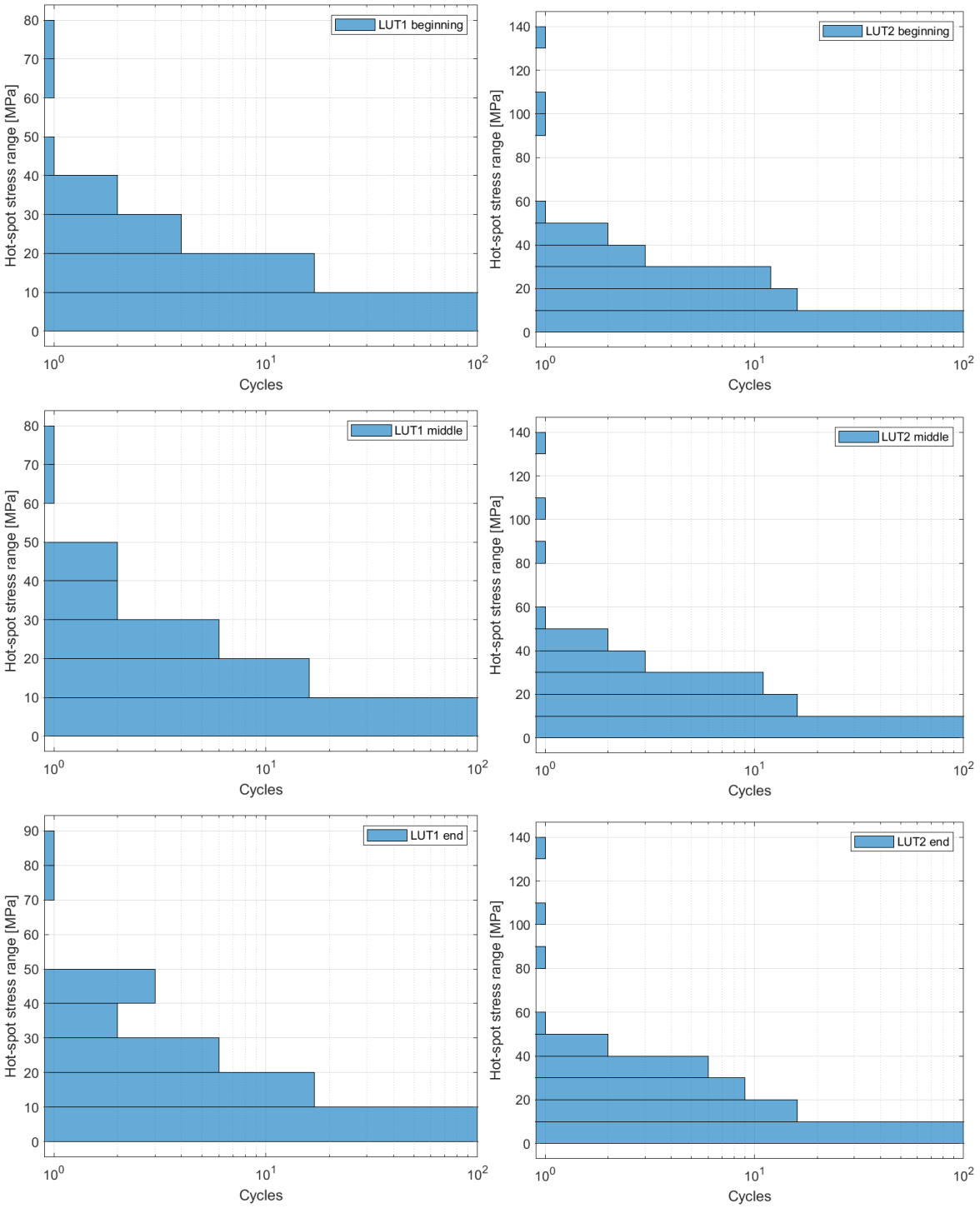

APPENDIX X

Hot spot stress range distributions based on 8-strain gauge method.

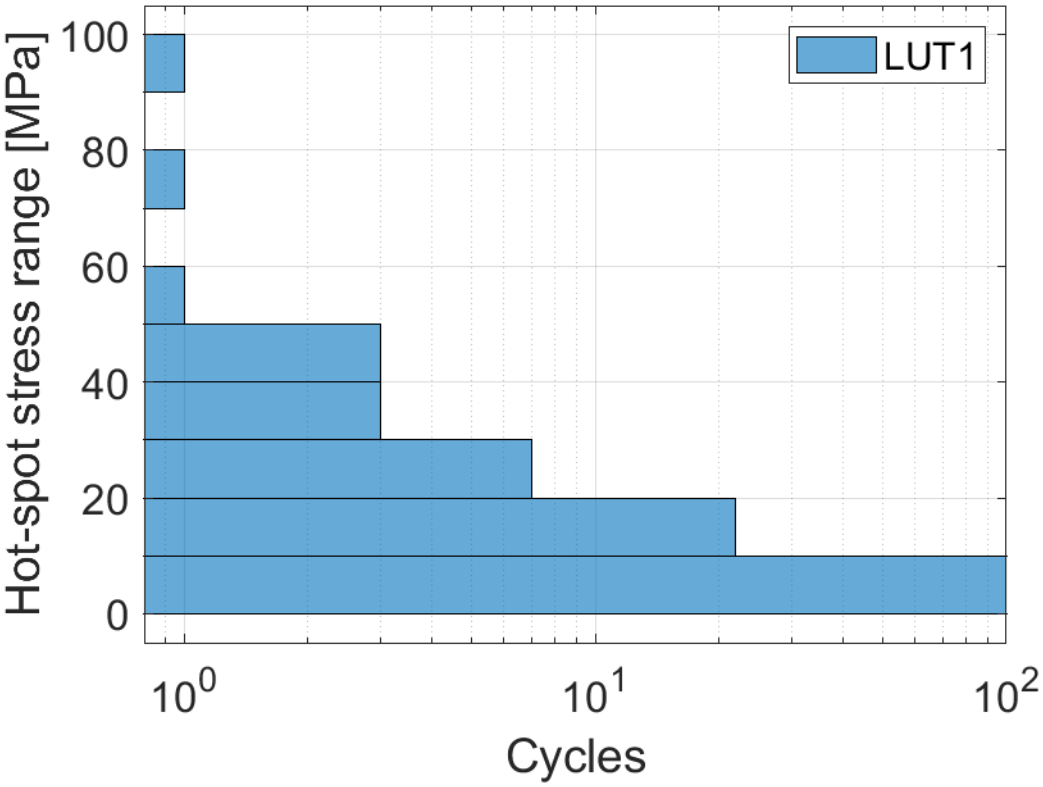

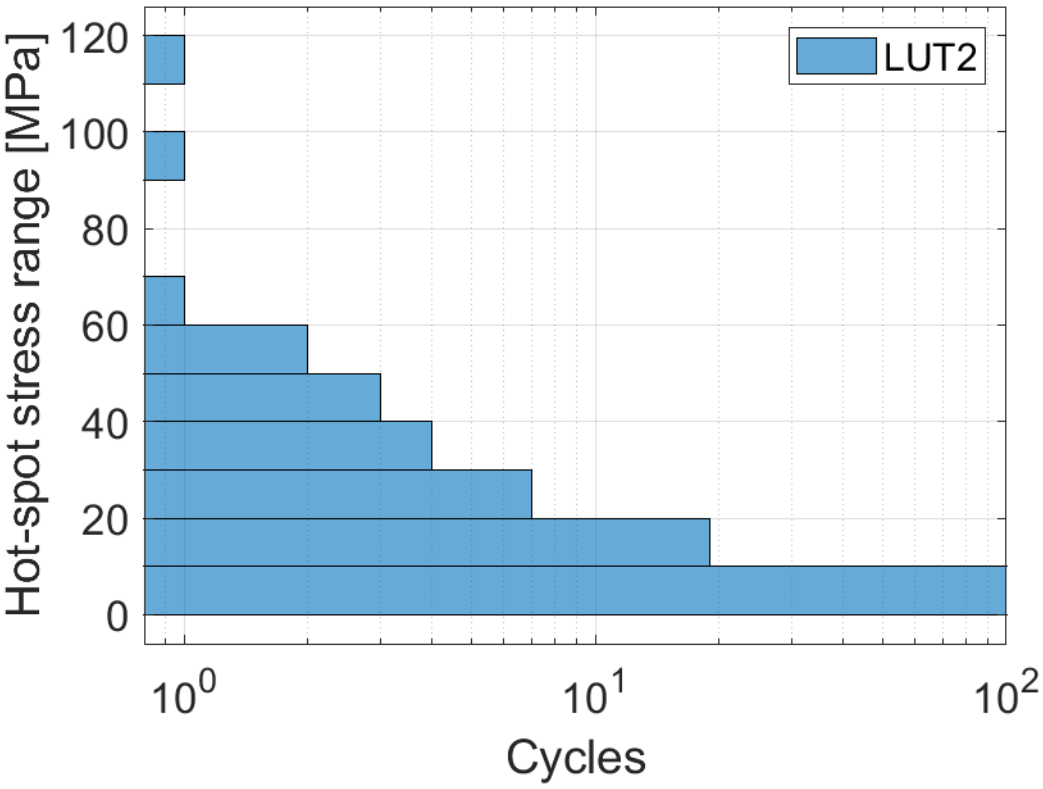

Hot spot stress range distributions based on True-Load.

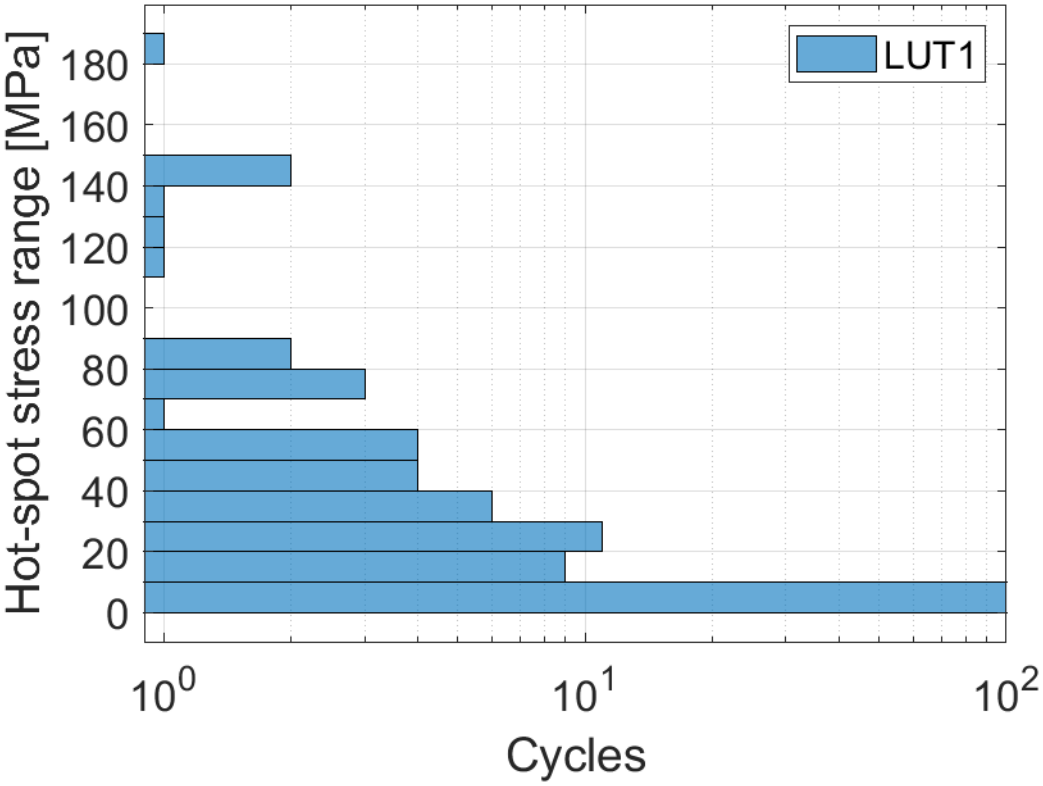

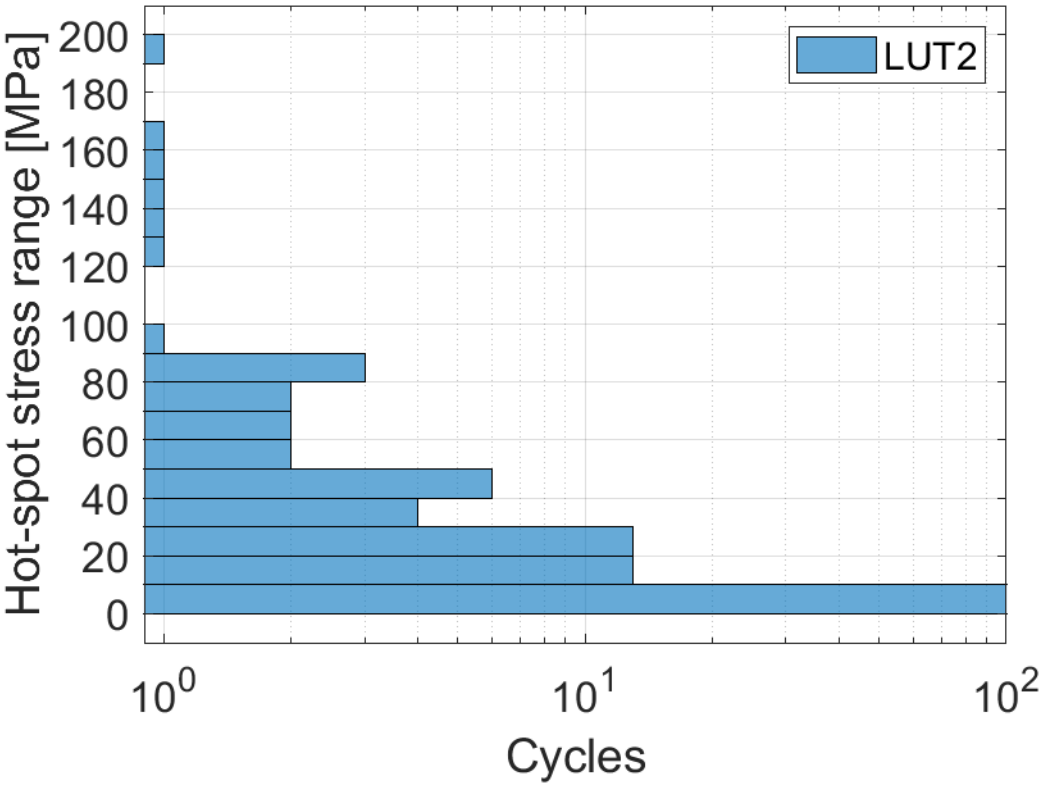

Palmgren-Miner's sum based on 8 strain gauges, ENS method and design S-N curve.

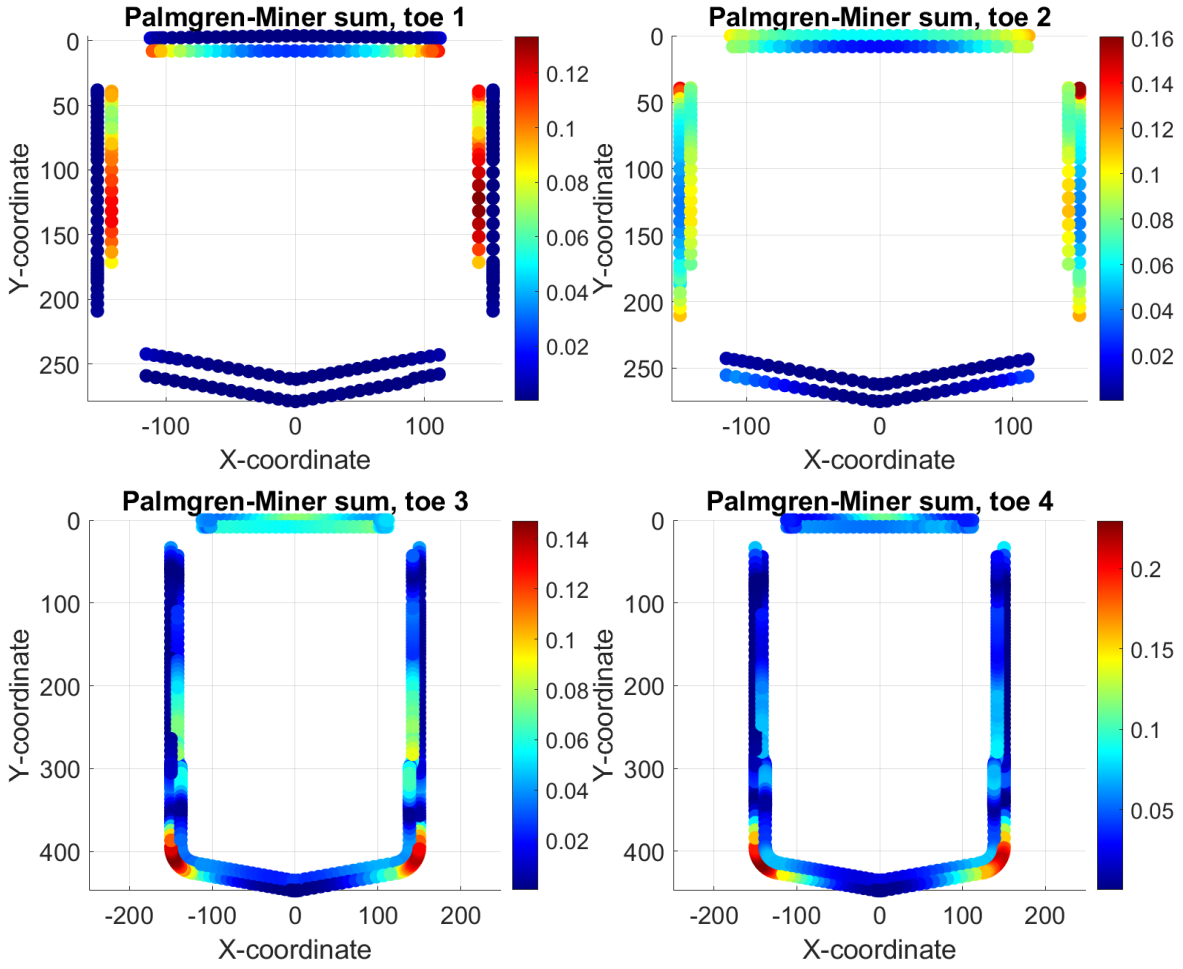

Palmgren-Miner's sum based on 8 strain gauges, ENS method and mean S-N curve.

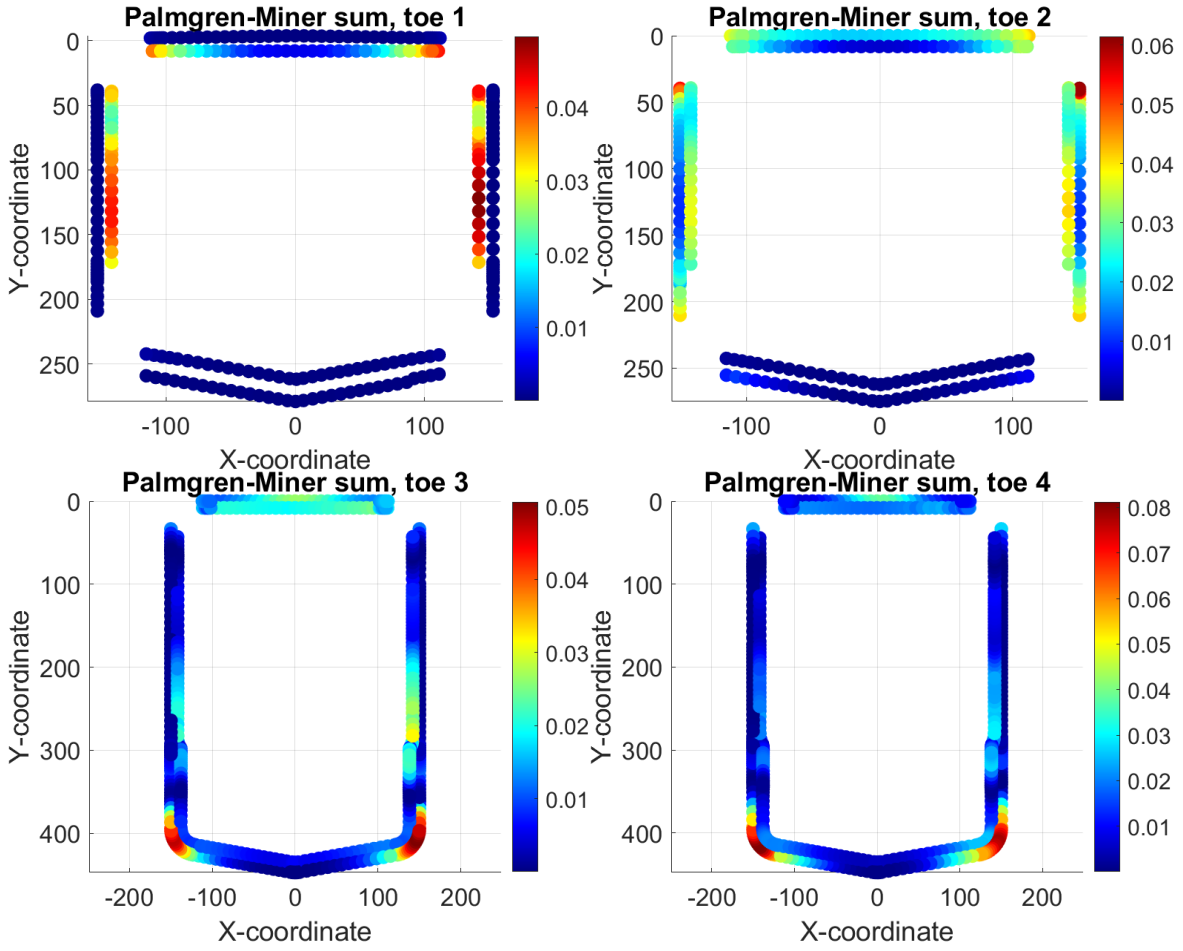

ENS range distributions of the most loaded node of each toe based on 8 strain gauge method.

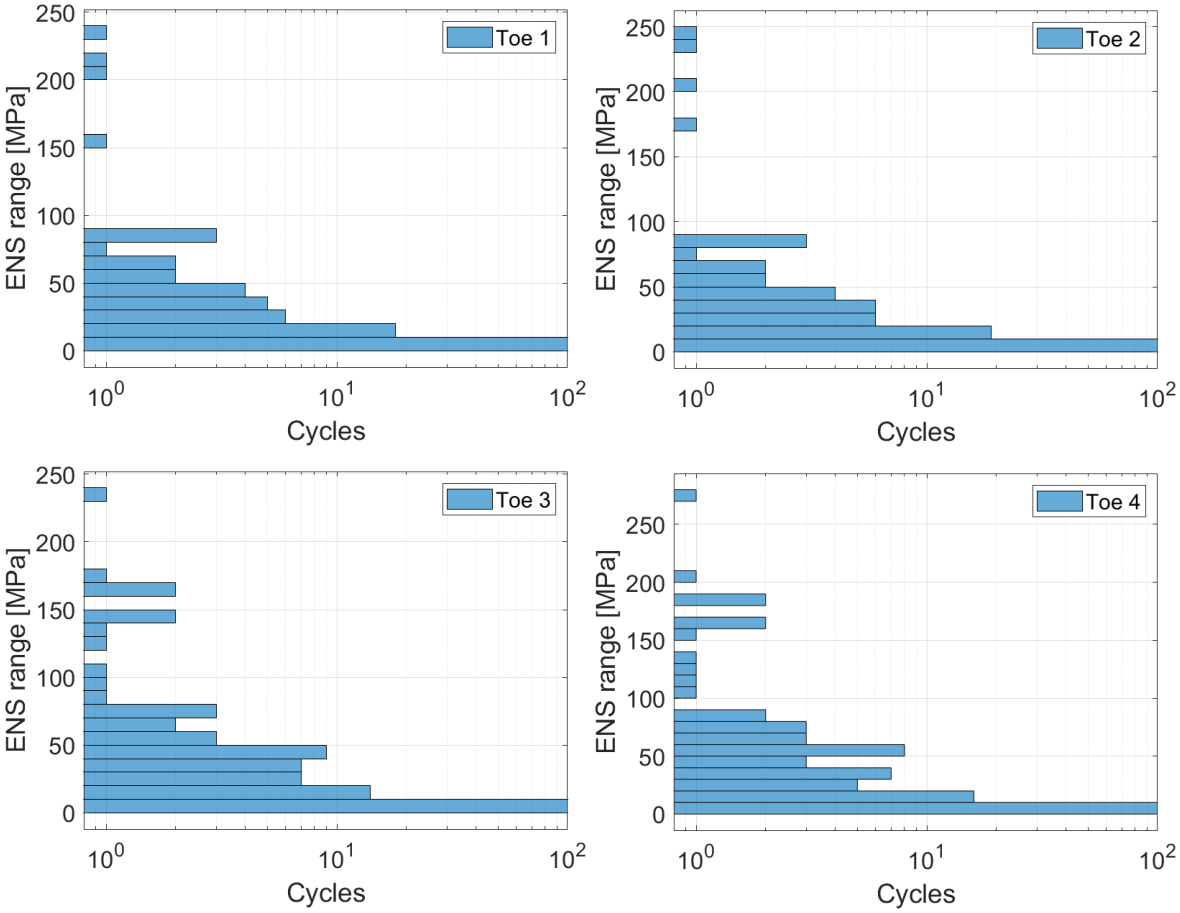

Palmgren-Miner's damage sum distributions based on effective notch stress, design S-N curve and True-Load.

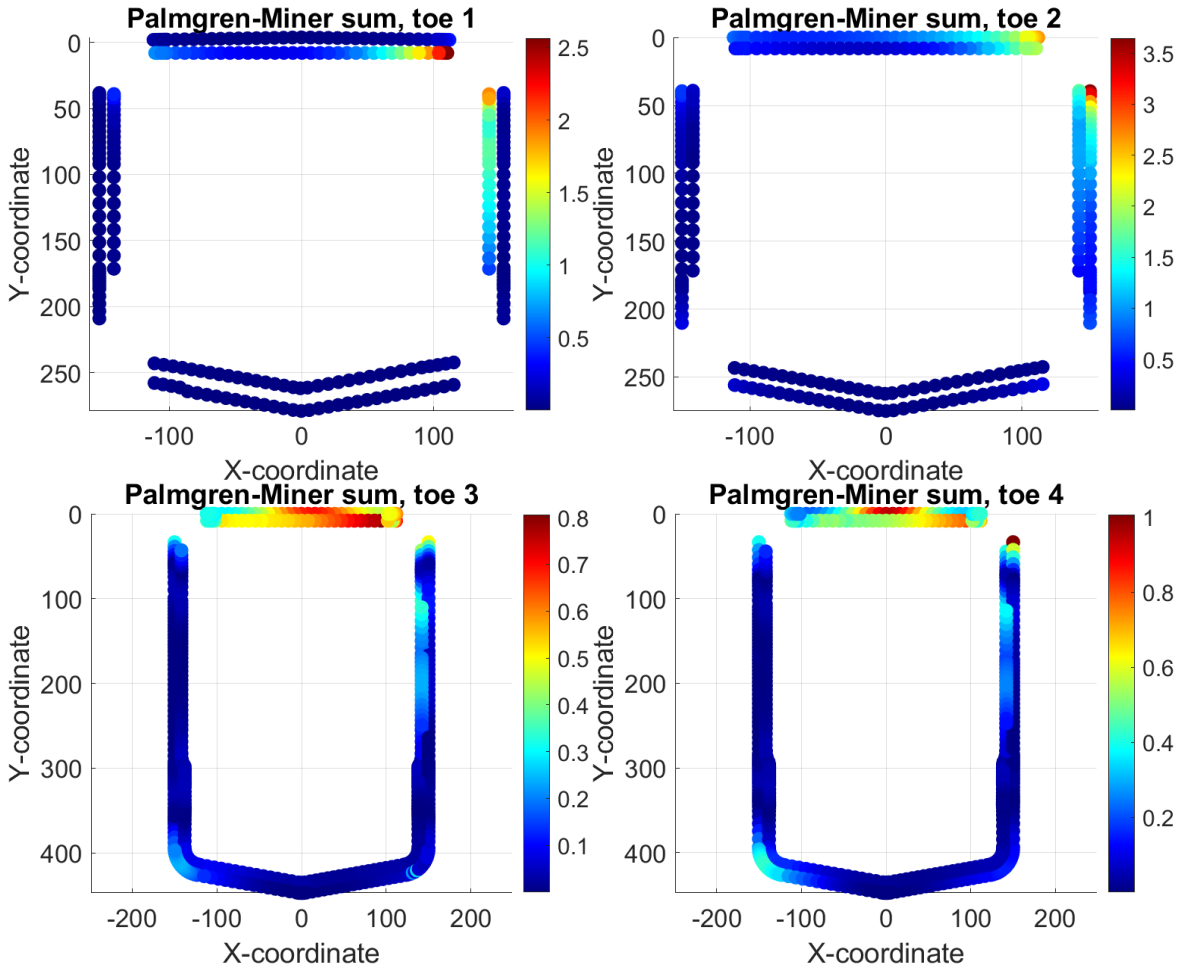

Palmgren-Miner's damage sum distributions based on effective notch stress, mean S-N curve and True-Load.

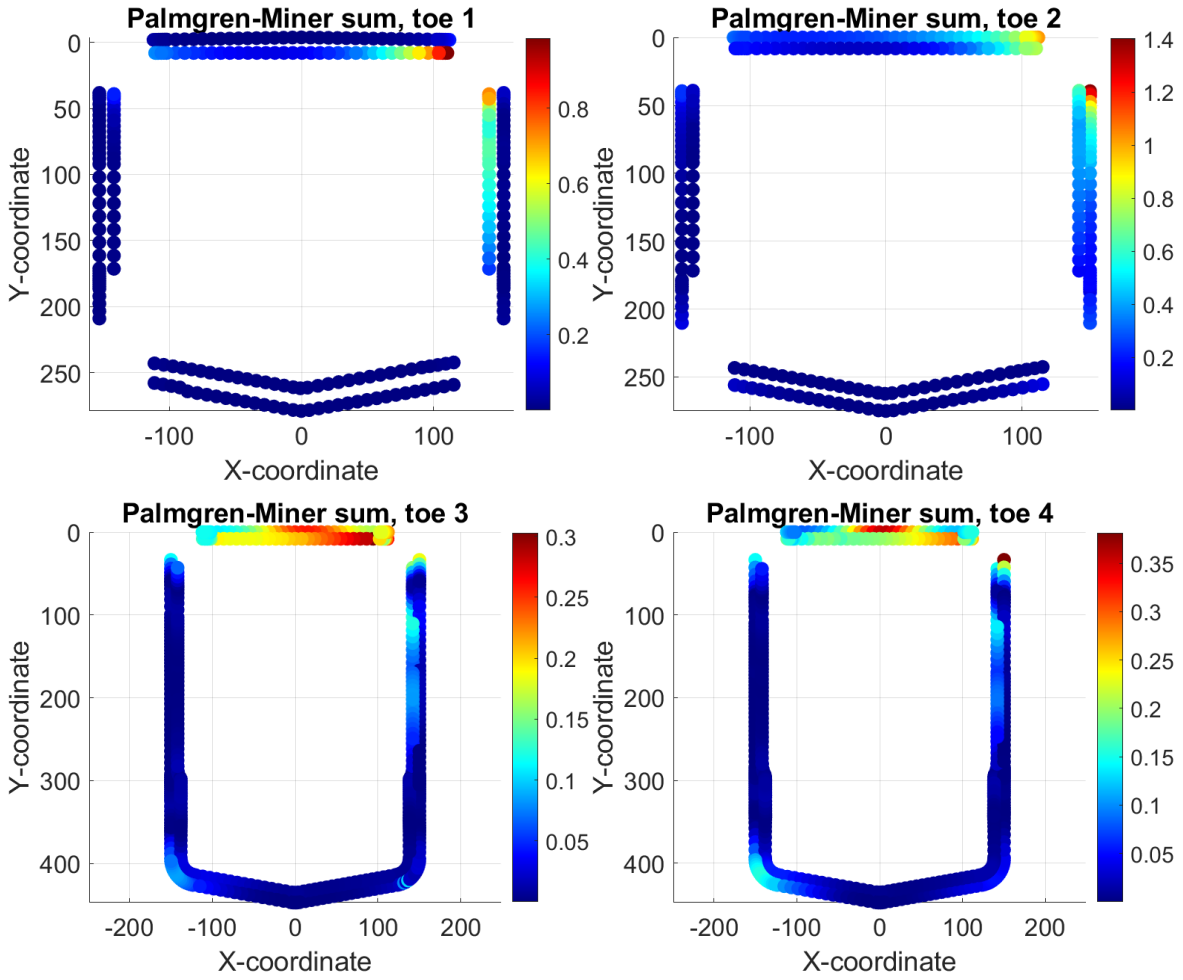

ENS range distributions of the most loaded node of each toe based on True-Load.

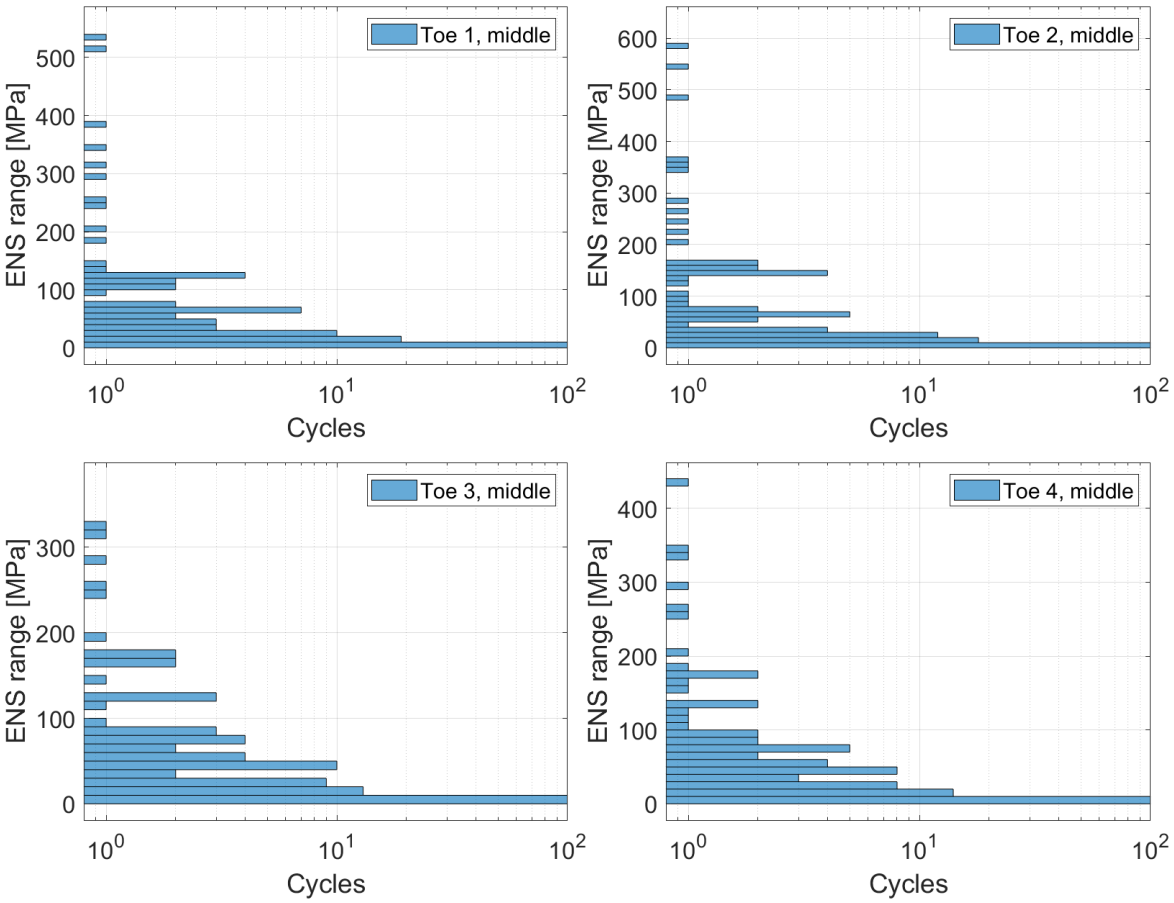

Palmgren-Miner's sums based on True-Load and 4R method.